Light-induced release of nitric oxide and carbon monoxide from metal complexes

Dissertation

zur Erlangung des akademischen Grades doctor rerum naturalium

(Dr. rer. Nat.)

vorgelegt dem Rat der Chemisch-Geowissenschaftlichen Fakultät der Friedrich-Schiller-Universität Jena

von M. Sc. Chem. Jingjing Liu

geboren am 29. 09. 1989 in Heilongjiang, China

Gutachter:

1. Prof. Dr. Wolfgang Weigand, Institut für Anorganische und Analytische Chemie, Friedrich-Schiller-Universität Jena

2. Prof. Dr. Benjamin Dietzek, Institut für Physikalische Chemie, Friedrich-Schiller-Universität Jena

3. PD. Dr. Alexander Schiller, ehemals Institut für Anorganische und Analytische Chemie, Friedrich-Schiller-Universität Jena

Tag der Verteidigung: 27. 02. 2019

Contents

Acknowledgements

First and foremost, I would like to thank my supervisor Priv.-Doz. Alexander Schiller for his guidance and support throughout the completion of my program as a doctoral student. I wish to thank him for giving me the opportunity to join his group and work on this interesting field. I am highly indebted for his time and patience to help me adapt to a foreign environment and guide me into PhD projects step by step. Dr. Schiller taught me not only how to perform scientific research, but also positive attitude towards life. I also deeply appreciate his encouragement and advice in busy schedule during my period of thesis-writing. It is really difficult to overstate my gratitude to Prof. Schiller, thank you so much!

Also I wish to thank Dr. Gandra Upendar Reddy for his help and patience with my many questions. I learnt a lot from him. I am grateful with Steve Gläser for help to familiarize with doctoral procedure, laboratory and Zusammenfassung. I want to thank the whole Schiller group: Dr. Vadde Ramu, Jörg Axthelm and Dr. Carmen Bohlender. I wish to also sincerely thank Dr. Peter Bellstedt and Dr. Friederike Pielenz for their technic analysis of samples with ^{19}F NMR spectroscopy, Dr. Johannes Steinmetzer for his computer studies and assistance of DFT calculations, Dr. Patrick Hoffmann for his cell studies and Dr. Helmar Görls for the determination of single crystal X-Ray analysis. Special thanks go to the technical staff of the organic and macromolecular institute and the inorganic and analytical institute for analytical investigation.

I offer my regards and blessings to my parents and my friends for their support in any respect during my PhD study in Germany.

Finally, I wish to thank the Chinese scholarship Council (CSC) for financially support during the PhD program which allowed me to study and work with such excellent scientists in Germany and also the German Research Foundation (DFG) for scientific research.

List of Abbreviations

NO	Nitric oxide
CO	Carbon monoxide
NORM	Nitric oxide releasing molecules
CORM	Carbon monoxide releasing molecules
NORMAs	Nitric oxide releasing materials
CORMAs	Carbon monoxide releasing materials
HOMO	The highest occupied molecular orbital
LUMO	The lowest unoccupied molecular orbital
DMF	N,N-dimethylformamide
DMSO	Dimethyl sulfoxide
ACN	Acetonitrile
NMR	Nuclear magnetic resonance
IR	Infrared spectroscopy
a.u	Arbitrary units
MLCT	Metal to ligand charge transition
ppm	Parts per million
ESI	Electrospray ionization
EPR	Enhanced permeability and retention
MS	Mass spectrometry
UV	Ultraviolet light
Vis	Visible light
Å	Ångström
δ	Chemical shift
CH	Cyclohexane

1. Introduction

Nitric oxide (NO) and carbon monoxide (CO), over the past several decades, have been considered as toxic gases, which are environmentally damaging or deadly to humans and animals at high concentrations.[1-4] However, since 1990s they have been well established as the famous gaseous signaling molecules (gasotransmitters), displaying notable chemical reactivity, including hydrogen sulfide (H_2S). [1] They are considered as messenger molecules that have diverse functions on and are involved in numerous bioregulatory pathways. Various animal models have demonstrated that these labile biological mediators diffuse into adjacent cells to interact with their targets, to reduce leukocyte adherence in the blood vessels, to be anti-inflammatory and to reduce blood vessel restenosis. [1-6] Thus, an appropriate amount of gasotransmitters delivery can lead to positive effects on inflammation and wound healing, which attracts considerable therapeutic interest. [2–4] This chapter will separately introduce the biological identities and activities of molecule species in organism systems. A brief description of the mechanism of species (NO or CO) and species donors during the process of releasing signal molecules on targeted sites will be given. The term “donor” implies that the compound releases the active mediator. Accordingly, these donors that release desired quantity of NO or CO to cells and tissues are called nitric oxide releasing molecules (NORMs) or carbon monoxide releasing molecules (CORMs) can be developed as potential therapeutic agents. In addition, their development in recent progress will be presented and the discussion of relevant drugs (NORMs and CORMs) that release NO or CO under light triggered conditions will be clearly illustrated. Meanwhile, this section will also introduce the application of these chemical compounds that can be used for controlled drug delivery, which generally recognized as NO releasing materials (NORMAs) or CO releasing materials (CORMAs).

1.1. Nitric oxide and its generation from NO releasing molecules

1.1.1. The biological activities of nitric oxide

Nitric oxide (NO) was long thought of as a simple, common air pollutant, which is formed from the oxidation of nitrogen and incomplete combustion of gasoline, for instance in automobile exhaust fumes. However, in 1867, Thomas Lauder Brunton first reported the therapeutic use of exogenous NO prescribed to rapid relief of angina pectoris in ischemic patients, which surrounded considerable controversy and was not recognized at the time due to his incorrect interpretation of the background of angina pectoris. [5–8] Maseri et al. in 1977, concluded the explanations of the effects of nitrates presented by Lewis and Gorlin, and established that the drugs could release coronary spasm and dilate the peripheral venous capacitance vessels due to their capability of dilating the coronary vessels within an ischemic myocardial domain. [7] In the same year, Ferid Murad discovered that several nitro vasodilators improved guanylate cyclase activity in particulate and/or soluble preparations from various tissues. Furthermore, he speculated that the generation of free NO from the decomposition of these agents also increased guanylate cyclase activity and cyclic guanosine monophosphate levels in intact tissues. [9] Robert Francis Furchgott believed that blood vessels were dilated because a new concept endothelium-derived relaxing factor (EDRF), which was probably produced by endothelial to relax vascular smooth muscle cells. Louis José Ignarro, together with and independently of Furchgott, concluded that EDRF was identical to NO. [10–14] This was the first discovery that a gas can act as a signal molecule in the organism. Interest in NO grew rapidly, consequently, research in various fields has implicated that this substance is involved in multiple physiological processes, including in the blood pressure regulation, mediation of specific cytotoxicity apoptosis, the inhibition of platelet aggregation, neurotransmission, and immune stimulation. [2,15–19] Hence, the Nobel Prize in Physiology or Medicine was awarded to Furchgott, Ignarro and Murad for their discoveries concerning “nitric oxide as a signaling molecule in the cardiovascular system”.

The whole biochemistry process of NO *in vivo* can be divided into three stages: generation, translocation and action. [20] During the first stage, NO is synthesized almost exclusively from L-

arginine catabolism to L-citrulline in a reaction catalyzed by a family of nitric oxide synthases (NOSs). Conceptually, these enzymes participate in a wide range of physiological functions by catalyzing the O_2^- and reduced NADP-dependent oxidation of L-arginine. [21] Three NOS isoforms which have around 50 % sequence homology produced by mammals can be identified according to the cell type or conditions in which they were first described: neuronal (nNOS), endothelial (eNOS), and inducible or inflammatory(iNOS). [16,22–27] NOSs utilize L-arginine as the substrate, molecular oxygen and reduced nicotinamide-adenine-dinucleotide phosphate (NADPH) as co-substrates. [28] Flavin adenine dinucleotide (FAD), flavin mononucleotide (FMN), and (6R-)5,6,7,8-tetrahydro-l-biopterin (H_4B) are cofactors of all isozymes. Each NOS isozyme contains a catalytic N-terminal oxygenase domain (NOS_{ox}) that binds heme (iron protoporphyrin IX), the substrate, H_4B and a C-terminal reductase domain (NOS_{red}) which binds FMN, flavin adenine dinucleotide (FAD) and NADPH. [29,30] In this process, the NOSs initially hydroxylate a terminal guanidino nitrogen of arginine to generate an enzyme-bound intermediate N^{ω}-hydroxy-L-arginine (NHA). [1,31–35] Subsequently, NHA is further oxidized to generate L-citrulline and NO (Scheme 1.1). [35] In both steps, NADPH derived electrons are transferred via the flavins FAD and FMN to the enzyme-bound heme, which enables the oxygen activation.

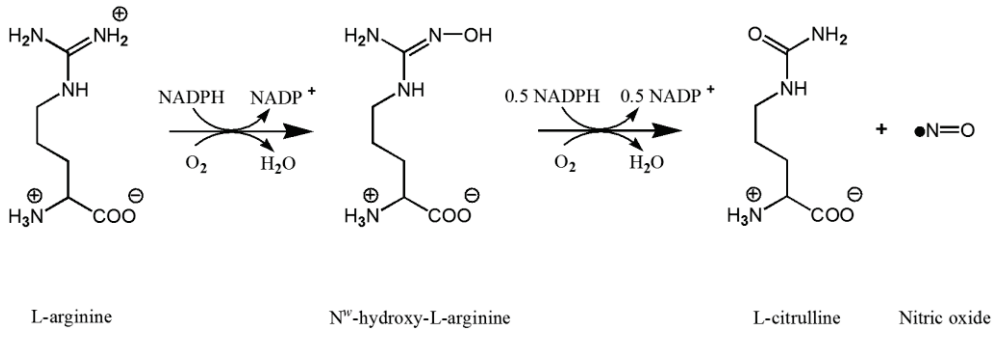

Scheme 1.1 Endogenous synthesis of nitric oxide. [35]

After the synthesis, newly generated NO need diffuse or be transported away from NOS to act as signal molecules. [20,36] During this stage, the chemical biology reactions of NO can be divided into two major categories, direct and indirect. [37–39] Direct effects of NO are defined as chemical reactions occur rapidly enough to interact with specific target biological molecules. Instead, the indirect effects are those biological targets react with reactive nitrogen oxide species (RNOS)

react which formed from the reaction of oxygen or superoxide with NO exerted medium effects. The former, generally, happen at low NO concentrations (< 0.2 μM), as well as the indirect effects involve in at higher concentrations of NO (> 0.4 μM). [37,40,41]

The first described physiological target for NO was soluble guanylyl cyclase (sGC), an enzyme that converts guanosine triphosphate (GTP) into the cyclic guanosine monophosphate (cGMP). [22,42,43] NO binds to the iron site within the heme moiety of guanylyl cyclase to facilitate a conformational change that results in enzyme activation. Another major direct effect of NO is interaction with cytochrome P450 (CYP), a family of enzymes that are involved in the synthesis and catabolism of numerous biomolecules in species ranging from bacteria through to plants and mammals. [44–46] Binding of NO to the heme can prevent oxygen binding leading to a reversible inhibiting catalysis or irreversible inhibition (indirect effect). Furthermore, the direct effects also conclude reactions of NO with some metal complexes, free radicals and lipid peroxidation at near diffusion rates.

In another pathway, NO may undergo various oxidative processing steps and can be converted to nitrogen oxide (NO_x) species with formal N atom oxidation states ranging from +1 to +5 before encountering a cellular target (equation 1−6).[47,48] Due to its unpaired electron, NO free radical (•NO) can react with molecular oxygen (O_2), superoxide anion ($O_2^{-\bullet}$) or transition metals to generate reactive nitrogen species (RNS): nitroxyl ions (NO^-), nitrosonium cations (NO^+), nitrite ions (NO_2^-), nitrate ions (NO_3^-), peroxynitrite ($OONO^-$) or metal nitrosyl derivatives. [43,47,49–52] $OONO^-$ is a powerful oxidizing and nitrating species that causes many pathological events including cardiovascular and neurodegenerative diseases, inflammation and cancer. [33,38,53] Meanwhile, NO^+ can react with nucleophilic centers such as ROH, RSH and RR'NH to produce RO-NO, RS-NO or RR'N-NO, consequently undergo other reactions to exert biological effects. In addition, •NO can also be converted to metal nitrosyl complex, some of which are better suited for delivery of NO or longer-term storage. [54,55]

$$2 \bullet NO + O_2 \rightarrow 2 \bullet NO_2 \quad (1)$$

$$\bullet NO_2 + \bullet NO \rightleftharpoons 2 \bullet N_2O_3 \quad (2)$$

$$N_2O_3 + H_2O \rightarrow 2NO_2^- + 2H^+ \quad (3)$$

$$N_2O_3 + RSH \rightarrow RSNO + NO_2^- + H^+ \quad (4)$$

$$\bullet NO_2 + RSH \rightarrow RS\bullet + NO_2^- + H^+ \quad (5)$$

$$\bullet NO_2 + RS\bullet \rightarrow RSNO \quad (6)$$

Finally, NO and NO derivatives play their roles through reactions with biomolecules in the action stage. Due to its radical character, NO interacts with large numbers of redox-active species, including targets composed of redox-active metals, redox-active metals that bound to or near redox-active ligands, redox-inactive metals which supported by redox-active ligands, or metal-free organic species.

1.1.2. Bonding of Nitric oxide in metal complexes

Nitric oxide free radical, an uncharged molecule and an exceedingly weak Lewis base when act as a nucleophilic agent, presents molecular orbitals with different nitrogen and oxygen contributions because of the difference in the electronegativities of nitrogen and oxygen atoms. The highest occupied molecular orbital (HOMO) of nitric oxide radicals is half-filled therefore the singly occupied molecular orbital (SOMO) is used in the radical recombination reactions and represents the orbital in which an electron is removed or added in redox reactions which represented by the molecular orbital diagram of •NO (Figure 1.1). [40] The bonding molecular orbitals belong predominantly to oxygen, while all antibonding molecular orbitals belong predominantly to nitrogen. [36] Rooted in the combination of the 2s atomic orbitals, the two sigma molecular orbitals (σ_1 and σ_2*), generally do not participate in bonding orbitals. The σ_2* orbital, having the more energetic antibonding, shows that the nitrogen nonbonding electron pair, nature of sigma bond, symmetrical characteristic and essential energy aspects of •NO. There also exists an unpaired electron in a π* molecular orbital polarized toward nitrogen in this molecule resides opposing the polarization of the lower energy π_b orbitals. Due to the five electrons in the outermost shell, nitrogen atom can consequently supply up to all five electrons to the more electronegative oxygen

atom, yielding diverse oxyanions. Or, conversely, the nitrogen atom can fill its outermost shell with full eight electrons by obtaining up to three electrons from less electronegative atoms (such as hydrogen and carbon atom). This electronic configuration, accordingly, results in a high reactivity and selectivity of the •NO, facilitating the oxidation to the nitroxyl cations (NO^+), reduction to the nitroxyl ions (NO^-), the possibilities of facile attack by oxygen affording NO_2, and the reaction with halogens (X_2) which leading to the formation of XNO. [56–58]

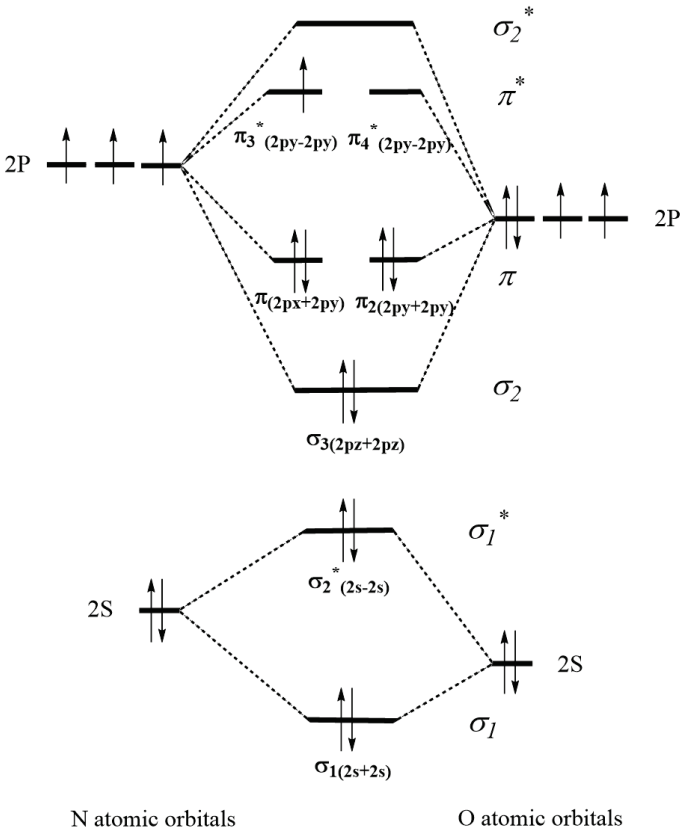

Figure 1.1 Energy level and molecular orbital diagram for •NO. [36,40,56]

In conclusion, almost all recombination reactions with radicals and transition metal ions are achieved by the nitrogen atom. Theoretically, NO is isoelectronic with the dioxygen monocation (O_2^+), as NO^+ (linear, sp hybridized) is isoelectronic with CO and CN^-, while NO^- (bent, sp^2 hybridized) is isoelectronic with O_2. In addition, NO^- like O_2 owns a triplet ground state, which increases ease of combination of certain types of metal nitrosyl complexes which have similar structure and electronic characters with biological oxygen activators.

The association reaction of •NO with transition metal ions is described as nitrosylation (equation 7), accompanying a shift of electron density to the metal center or the nitrosyl ligand. [36,48]

$$M + \bullet NO \rightleftharpoons M{-}NO \tag{7}$$

Bonding of NO to transition metals is referred to as the attachment of the N atom to the metal, M−N−O (Figure 1.2 (a)), while the M−N−O bond angles, commonly, may be essentially linear (considerable charge transfer to the metal) or up to 120° bent (charge transfer from the metal). [56,59] Within the M−N−O group, the M−N bond is usually strong, whereas the N−O bond is relatively weak.

(a) (b)

Figure 1.2 (a) Simple illustration of NO binding to a metalloporphyrin center as the nitrosyl cation (NO^+) with a linear M−N−O group (left) or the nitroxyl anion (NO^-) with a bent M−N−O group (right). (b) Molecular orbitals involved in dπ−π* bonding between metal and •NO.

Simultaneously, in the molecular orbital approach, this procedure of bond between NO and metal can be generally described as the superposition of two components, donation of electron density from NO to the metal and a back-donation. [56,60] The former involves a sigma orbital on the N atom (σ_2 shown in Figure 1.1), while the latter contains a dπ−π* interaction which occurs from dπ orbitals of metal to the NO π* orbitals (Figure 1.2 b). In addition, the overlap and extension of the interactions depend to a large extent on the oxidation state and identity of the metal ions as well as specific properties of the complex structure, such as its configuration, impact of ligands, and coordination number. [61] A high metal charge benefits the σ-binding strength for any ligand and declines in the π-back donation. Compared with CO, although this bonding is approximately the same as that of CO to transition metals, nitric oxide is prone to accept electron than carbon monoxide because it is much more electronegative than CO. This reactivity also results in a higher affinity for metal ions than O_2 and CO.

Because of the covalent nature of the M−N−O interaction and the difficulty of assigning formal oxidation states to the metal and the NO in nitrosyl complexes, a description of the metal−NO interaction was proposed by Feltham and Enemark in 1974 to provide a general formalism that deals with the ambiguous electronic structure of the metal nitrosyls. It was presented as $\{M–NO\}^n$ moiety where n stands for the sum of electrons number associated with the metal d and NO π^* orbitals. [62,63] In this scheme, mostly complexes have slightly bent arrangements with M−N−O bond angles deviations from 180° of up to 10°, whereas only a few keep the truly linear structure. According to the Walsh's rules for this six-coordinate complex, the bending of M−N−O angle will increase accompanying the weakening of the metal−ligand bond trans to the nitrosyl when n of $\{M–NO\}^n$ unit enlarge from 6 (Figure 1.3). [64–67] Thereby, a variety of spectroscopic techniques used to determine the nature of the M−N−O interaction and molecular structure also change and reflect the binding between NO and the central metal. For example, the values of ν_{NO} are particularly sensitive to the electron content n. Generally, $\{M–NO\}^n$ complexes display values of ν_{NO} at around 1840–1960 cm^{-1} (n = 6), 1600–1720 cm^{-1} (n = 7) and 1340–1620 cm^{-1} (n = 8). [68]

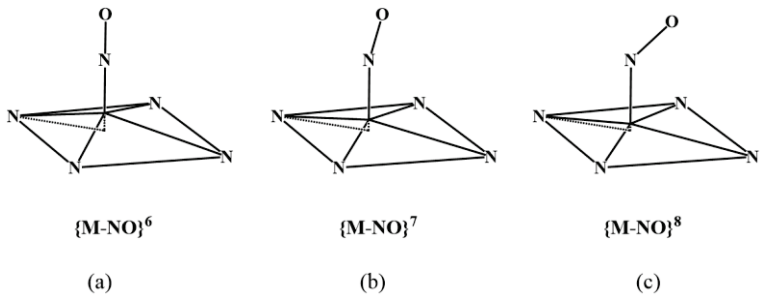

Figure 1.3 Probable structures of the six-coordinate group in nitrosyl complexes $\{M-NO\}^n$ with n = 6, 7 and 8. [64–67]

1.1.3. Metal nitrosyl coordination complexes for NO release

Sodium nitroprusside ($Na_2Fe^{II}(CN)_5NO·2H_2O$, SNP) prepared in the middle of the nineteenth century by Playfair, was first demonstrated in 1929 to induce a significant reduction in the blood pressure of a severely hypertensive patient without noticeable side effects. [69–72] People noted that SNP exhibited long-lived electronic excited states upon photoexcitation with 350−580 nm radiation, resulting in the dissociation of the nitrosyl ligand. [73–75] It is also the first iron nitrosyl

complex that causes muscle relaxation by releasing NO through its interaction with sulfhydryl-containing molecules present *in vivo*. Hence, this character is utilized in the medical community where SNP is used as a NO delivery agent and garnered significant attention.

There are also two famous iron-sulfur cluster species named as Roussin's black ($K[Fe_4(NO)_7S_3]$, RBS) and red salts ($K_2[Fe_2(NO)_4S_2]$, RRS), which carry numerous NO equivalents and have high absorptivity in optical spectra leading to potential attractive in tissues (shown in Figure 1.4). [54,76–78] Interestingly, photolysis of RRS in aerobic aqueous solution gives rise to the quantitative formation of RBS and the RBS produce undergoes further photodecomposition to generate NO and Fe^{3+} species. [79,80] Due to their high solubility's in non-polar solvents, Roussin's salts can penetrate the endothelial cell membrane easily and deliver NO for hours, corresponding to the early report demonstrated that RBS anion acted as a vasodilator upon irradiation with UV light (< 400 nm) and RRS was used in photo-induced NO delivering for sensitizing radiation killing of hypoxic cells. [81–86] Besides these, Roussin's salts are also found a bacteriostatic effect, presumably related to the interaction of released NO and iron-sulfur proteins.

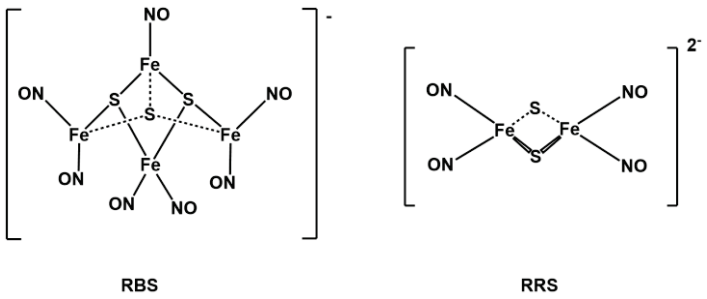

Figure 1.4 Structure of Roussin's black (left) and red salt (right).

An essential requirement for successful use of metal nitrosyls as exogenous NO donors in the organism is their structural integrity in biological conditions. Unfortunately, many iron nitrosyls display unpredictable stability under aqueous environments resulting in hydrolytic decomposition, disproportionation reactions or ferric hydroxide precipitation. [63] Some compounds release NO spontaneously before triggered in specific sites and some even remain toxic after NO liberation. Those behaviors restrict the use of iron NO precursors severely. Although iron nitrosyls derived

from designed ligands can solve problems, other suitable transition metal alternatives have gained attention to develop in efforts.

Generally, ruthenium complexes are more kinetically stable than their iron analogs. For this reason, ruthenium nitrosyls have received considerable attention in environmental remediation and in biomedical applications. [82,87] Initial research on the Ru–NO complexes started from compounds with simple ligands with the formula $[Ru(NH_3)_4(X)(NO)]^{3+}$ (X = NH_3, sulfite, pyridine, imidazole, salen and related salophen etc.), in which a ammine ruthenium specie precursor $Ru(NH_3)_6^{3+}$ which can produce $Ru(NH_3)_5NO^{3+}$ was an important nitrosyl compound to study systematic mechanistic of metal–NO bond formation until the discovery that NO is a mammalian bioregulatory agent. [88–90] Ruthenium nitrosyls by far have been tried to incorporate into different types of polymeric materials or inorganic solids due to their inherent thermal stability. Mascharak and co-workers observed that dye molecules or conjugated fluorophore group can be directly coordinated to Ru centers in related ruthenium nitrosyls which even allows detection in solution via the fluorescence signaling. [91–93] Borovik et al. immobilized the ruthenium nitrosyl complexes by modifying the salen ligand to allow for copolymerization with a mesoporous ethylene glycol dimethylacrylate material. [94] Tfouni entrapped soluble complex $[Ru(salen)(OH_2)(NO)]^+$ in a porous silicate sol-gel to prepare an immobilized and regenerable NO source. [95] The great advantage of ruthenium complexes is their great stability over long periods of time under physiological conditions, while relatively low quantum yield for NO release and the in general requirement UV light for NO release are crucial disadvantages. Ongoing investigations are needed to overcome these critical limitations in order to prove to be suitable systems for applications as anticancer drugs in physical systems. [91,96–100]

Commonly, the occurrence of transition metal complexes is Fe and Ru metals, however, to date more research have included Mn, Cu, Os, Ir, Au, Ni, Cr, Co and so on. [57,101–114] Overall, the applications of these materials with incorporated metal nitrosyls are appropriate and practical for investigating the roles of NO in biology area and need to be further studied.

1.1.4. Photoactive release of NO from metal nitrosyl complexes

For treating relevant diseases, the nitric oxide releasing complexes must be contained in or incorporated with biocompatible materials so that NO can be transported to a designated local area and release NO selectively to targeted sites. As the half-life of nitric oxide is relatively short (in seconds), the release area of NO is normally confined to the region around where the NO donors are placed. [115] NO releasing materials are in general triggered by pH change, enzyme degradation, thermal or chemical variety, or photoinduction to elicit a desired response. [116–121] Photoactive NO releasing materials (photo-NORMs) have gained increasing attention because they can deliver NO under precise control (over the time, location and dosage) to selected biological targets by using light as an external medium and thereby can be explored as a new strategy of photodynamic therapy (PDT). Photo-NORMs must be stable in aqueous solutions in the dark and relatively non-toxic, the residue in the organism can be eliminated in an appropriate time interval. While the activity of photo NO donating complex must be triggered only by irradiation at a specific wavelength. Furthermore, photo-NORMs that can effectively release their cargo upon low intensity light exposure at long wavelengths are also beneficial to reduce tissue damage. In theory, the near-infrared (NIR) light which can penetration through mammalian tissue is primarily limited to the range of around 700–1000 nm, on the other hand, it happened high scattering in tissues when light longer than 800nm. [122,123] Metal nitrosyls complexes are desirable photo-responsive candidates because mostly of these complexes release NO by exposing to the light of various wavelengths.

As mentioned above, iron–nitrosyl complexes usually lack stability and some of them have toxicity problems under physiological conditions, the issues of relatively low quantum yield for NO releasing and UV light triggered for ruthenium complexes are also needed to solve, as well as manganese compound has a limited stability in aqueous media. Plenty of strategies have been proposed to move forward with metal-NO complexes. A variety of metal nitrosyls coordinated with quinoline, pyridyl moiety, carboxamido-N or thiolato-S donors to be activated by longer visible wavelengths or near-infrared light and rapidly release NO under irradiation. [63,82,96,110,124,125] In physicality, large number of metal complexes were embedded in various structures, such as gels, thin films, polymer fibers, microparticles, and nanoparticles. [41,126–130] For example, Schiller and his colleagues entrapped a ruthenium photo-NORM molecule which was insoluble in aqueous

solution in nanofibrous non-wovens with electrospinning to release NO into a biological environment upon low intensity illumination. [131]

1.2. Carbon monoxide and its generation from CO releasing molecules

1.2.1. The biological activities of carbon monoxide

Carbon monoxide (CO), an odorless, colorless and tasteless but toxic gas which typically produced by insufficient oxygen, was described as “the silent killer” for a long time. Like NO, CO was recently considered as a signaling gas molecule in living organisms involving multiply of bioregulatory functions. Compared with O_2, CO holds much more diffusion and affinity for hemoglobin which is oxygen-transport metalloprotein thereby easily generates carboxyhemoglobin (COHb) and ultimately is removed from respiratory organs. [132,133] The principal task of hemoglobin is to release oxygen which carries from the lung to provide energy for the metabolism process of the organism. When CO occupied more than 50 % of the total hemoglobin, it will inhibit aerobic respiration circulation by interfering with the oxygen-carrying ability subsequently leading to coma, respiratory depression or other fatal outcomes. [134,135] While at low concentrations, carbon monoxide exerts remarkable influences on tissues, such as vasodilatation, anti-inflammatory, inhibition of cell proliferation, neurotransmission and anti-apoptosis, consequently can be used as a potential therapeutic agent for wound healing, organ transplant and cardiovascular diseases. [132,136–143]

Exogenous carbon monoxide is primarily generated through incomplete oxidation of carbon-containing compounds, while endogenous carbon monoxide (CO) is overwhelmingly generated by the heme physiological degradation reaction with the presence of heme oxygenase (HO) enzymes in mammalian cells. [144,145] There are three isozymes of HO with dissimilar tissue localization and distinct functions, which are respectively known as inducible isoform HO-1 and constitutive isoforms HO-2, HO-3. [146–150] HO-1 is a stress protein which exists in endoplasmic reticulum of tissues that respond to regulation by multiple stress stimulation and protects the cells from oxidative stress. HO-2 is mainly active in the vasculature and nervous system in the brain, while HO-3 is a slightly active heme-binding protein which shares around 90 % amino acid

homology with HO-2. Both HO-1 and HO-2 can participate in the reaction of heme catabolism in which the electrons are supplied by NADPH-dependent cytochrome reductase. In addition to CO, Fe^{2+}-protoporphyrin IX (Heme) is broken down to ferrous iron ion (Fe^{2+}) and biliverdin which is subsequently reduced to bilirubin by biliverdin reductase. The generated ferrous iron ions are converted into ferritin through binding protein and activation of iron response elements. [151–153]

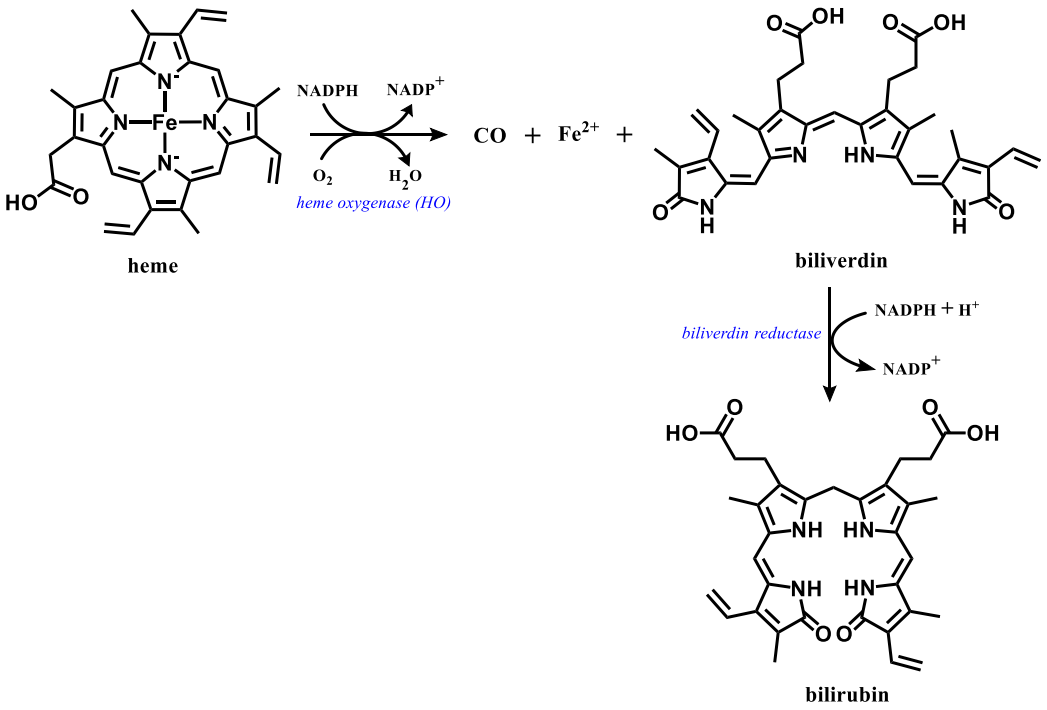

Scheme 1.2 The pathways of heme degradation and formation of carbon monoxide by heme oxygenase *in vivo*.

Like NO, one of the main molecule targets of CO is to produce cyclic guanylyl cyclase (cGMP) by activating soluble guanylyl cyclase (sGC). CO associates with the histidine-ligated hemoprotein that have a pentacoordinate metal center in which the heme cofactor covalently bonded to iron via an axial histidine. [1,154] This action of CO is much weaker than that of NO due to the ability of NO that binding bursts with imidazole group in the heme molecule and subsequently Fe^{2+} exposure which CO doesn't have. This corresponded to the dramatic bent hem and massive N-terminal subdomain shift proceeded by NO with fully activated state compared to the initial large hem pivot shift introduced by CO. [155] Another interaction of CO and sGC is completed by the combination of CO with NOS to stimulate NO production. In addition, CO was

reported to exhibit more critical signaling roles in anaerobic conditions than NO because of the limitation of NOS under hypoxic conditions. [156]

Another target to realize protective effect of CO involves regulation of various ion channels that activated by the changes of membrane potential and/or the increase of intracellular ions concentration. The most noticeable ion channels are potassium ions (K^+) channels, which are also named as big potassium (BK) channels (Maxi-K or slo1), containing voltage-activated potassium channels (K_v), calcium-activated potassium channels (BK_{Ca}) and ATP-sensitive potassium channels (K_{ATP}). The stimulation of BK channels accelerates to stabilize of membrane potential and diminish cell activation resulting in relax vascular smooth muscle cells. [152,157] CO affects the L-type calcium ions (Ca^{2+}) channels through inducing the generation of reactive oxygen species (ROS) that can interact with cysteines located on the C-terminal tail of Ca^{2+} channels. This inhibition of Ca^{2+} channels reduces the calcium ions influx and thereby can be applied in coronary heart disease. [158,159] Besides the K^+ channels and Ca^{2+} channels, CO can also affect sodium ions (Na^+) channels and other channels to conduct multifold functions. [160–162] After accomplishing its mission, around 80% of CO is exhaled through the lung with the form of COHb as well as a fraction of CO is oxidized to CO_2 at a quite slow rate to be expelled from the organism.

In addition, CO can interact with the metal ion in metalloclusters of specific microbial proteins through a haem-independent approach to complete the reversible oxidation of CO to CO_2 in the global carbon cycle. [163]

1.2.2. Bonding of carbon monoxide in metal complexes

The possession of unpaired electrons of NO and the ability of chemically rearrange in aqueous solution for H_2S help improve their chemical activities, unlike them, CO seems the least chemically reactive molecule and quite stable in biological systems. Carbon monoxide molecule is isoelectronic with nitrogen molecule (N_2), cyanide ion (CN^-) and nitrosonium cations (NO^+), containing ten valence electrons which can be represented by the configuration $(\sigma_{2s})^2(\sigma^*_{2s})^2(\pi_{2p})^4(\sigma_{2p})^2$ distributing over triple bond between carbon and oxygen atoms and one lone pair electrons on each of the atoms (:C≡O:). [164,165] The molecular orbital (MO) of CO (sp hybridized) is the result of contribution from atomic orbitals (AO) of carbon and oxygen (shown

in Figure 1.5). The bonding molecular orbitals stem predominantly from the oxygen atom orbitals and the antibonding molecular orbitals mainly from carbon. A σ bond is produced by the combination of sp_z-hybrid orbital of carbon atom and the p_z-orbital of the oxygen, while the p_x- and p_y-orbitals of the both atoms form two π bonds. [150,166–169]

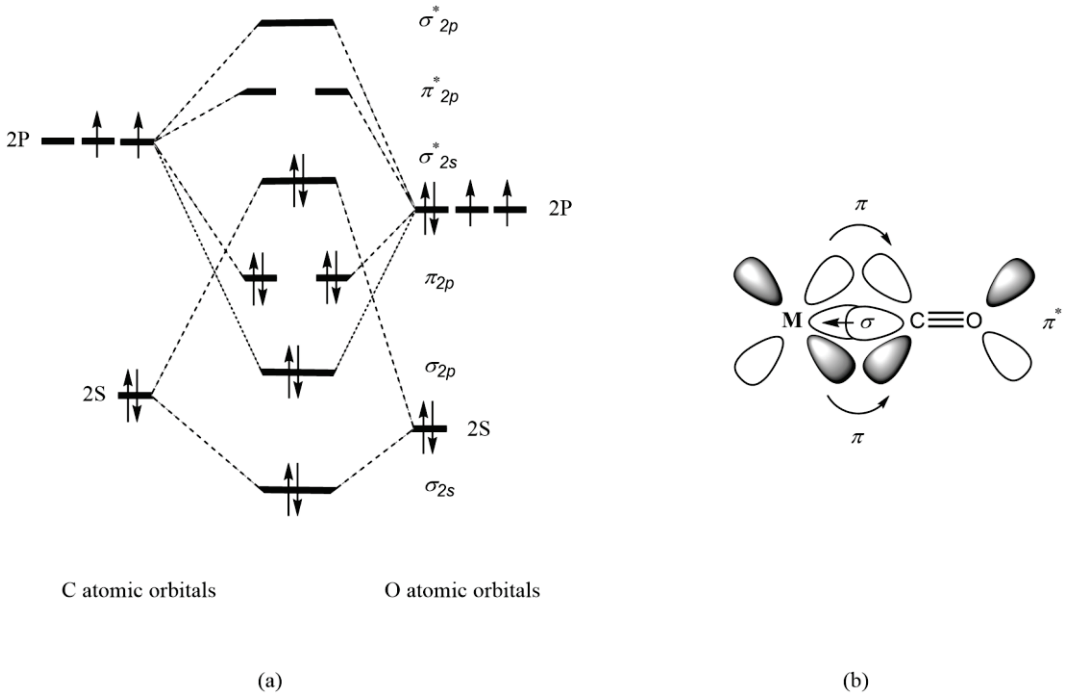

Figure 1.5 (a) Simplified molecular orbital diagram of CO and (b) the bonding between CO with a metal center.

This configuration leads to one lone pair of electrons leave on the oxygen 2s-orbital and another lone pair stay in a carbon sp_z-hybrid orbital. The HOMO (σ^*_{2s}) of CO is a slightly antibonding orbital polarized on the carbon atom, through which can act as a Lewis base in chemical reactions by donating electron pair into an empty metal (or other main group element) orbital forming a σ bond between the carbon atom and the acceptor atom. This is propitious to contribute to a higher reactivity of carbon monoxide than nitrogen because the HOMO of N_2 molecule is a bonding orbital occupied by balanced electrons. Meanwhile, the LUMO (π^*_{2p}) of CO is also polarized on the carbon atom and can accept electrons from the electron rich donors. When bonded with a metal atom, CO donates its electrons to d-orbital of metal atom thus also forms a σ bond with missive negative charge on the central metal atom. To remove the excess negative charge and host the stability of the CO-M bond, the metal donates back electron density to the antibonding π*

molecular orbital on the CO which overlapped with filled d-orbitals of the metal. This process is called π back-donation, which weaken the carbon-oxygen bond as well as strengthen the carbon-metal bond and support CO in acting as a Lewis acid. The extent of π back-donation will also affect the vibrational frequency of carbon-oxygen bond which can be reflected in IR spectrum. The characteristic vibrational frequencies in various bonding generally range from 1650 cm^{-1} to 2200 cm^{-1}, while the ν_{CO} of free carbon monoxide is usually found around 2143 cm^{-1}. [170] In addition, within the M-C-O group, the carbon-oxygen bond is generally strong, whereas the carbon-metal is relatively weak. This contrasts with the metal nitrosyl complexes mentioned above where the nitrogen-oxygen bond is weak while the nitrogen-metal bond is relatively strong. The binding mode helps CO cleavage from metal complexes.

1.2.3. Metal carbonyl coordination complexes for CO release

Carbon monoxide releasing molecules are preferably constructed of transition metal carbonyl complexes with one or more CO ligands and possible ancillary ligand for many decades. They can be presented as a simple formula $M_xL_y(CO)_z$, where M is the metal ion, L is coordinated ligand, as well as the stoichiometric coefficients x and z must be ≥1. When CORMs are triggered, CO will liberate from associated CO releasing molecules (equation 8).

$$M_xL_y(CO)_z \rightarrow M_xL_y(CO)_{z-n} + n\,CO \quad (1 \leq N \leq z) \qquad (8)$$

From the point of therapeutic use, metal carbonyl complexes which involved this process must satisfy some essential requirements, such as reasonable solubility in aqueous solutions and stability for storage under ambient mediums (including aerobic conditions). Moreover, they and their metabolites after decomposition should be non-toxic or low-toxic and do not interact with biological systems.

The first generation of CORMs was introduced by Motterlini *et al.* in 2002 and they studied the behaviors of three water-insoluble commercial metal carbonyls, iron pentacarbonyl ($Fe(CO)_5$), dimanganese decacarbonyl ($Mn_2(CO)_{10}$, CORM-1), and tricarbonyldichlororuthenium (II) dimer ($(Ru(CO)_3Cl_2)_2$, CORM-2) as CO donors. [171] $Fe(CO)_5$ and CORM-1 release CO by exposing to a

cold light source over around 60 mins, however, $Fe(CO)_5$ is highly toxic and is limited for further development. CORM-2 releases CO spontaneously through ligand exchange by forming a new bond with S in DMSO solution. Furthermore, to improve the solubility in water solution, tricarbonylchloro(glycinato) ruthenium (II) ($Ru(CO)_3Cl(NH_2CH_2COO)$, CORM-3) was developed and rapidly liberated CO in vivo biological models. [172] Besides triggered by ligand substitution, CORM-3 can also be driven by thermal degradation. CO will thermally dissociate from the metal complexes when heated, with the vacant site occupied by solvent ligand. The thermal strategy is basically used for the synthesis of simple metal carbonyls but is limited employed in physiological environment because of the contradictory attributes of activated temperature (approximated to room temperature) and the stability of initiators under such conditions.

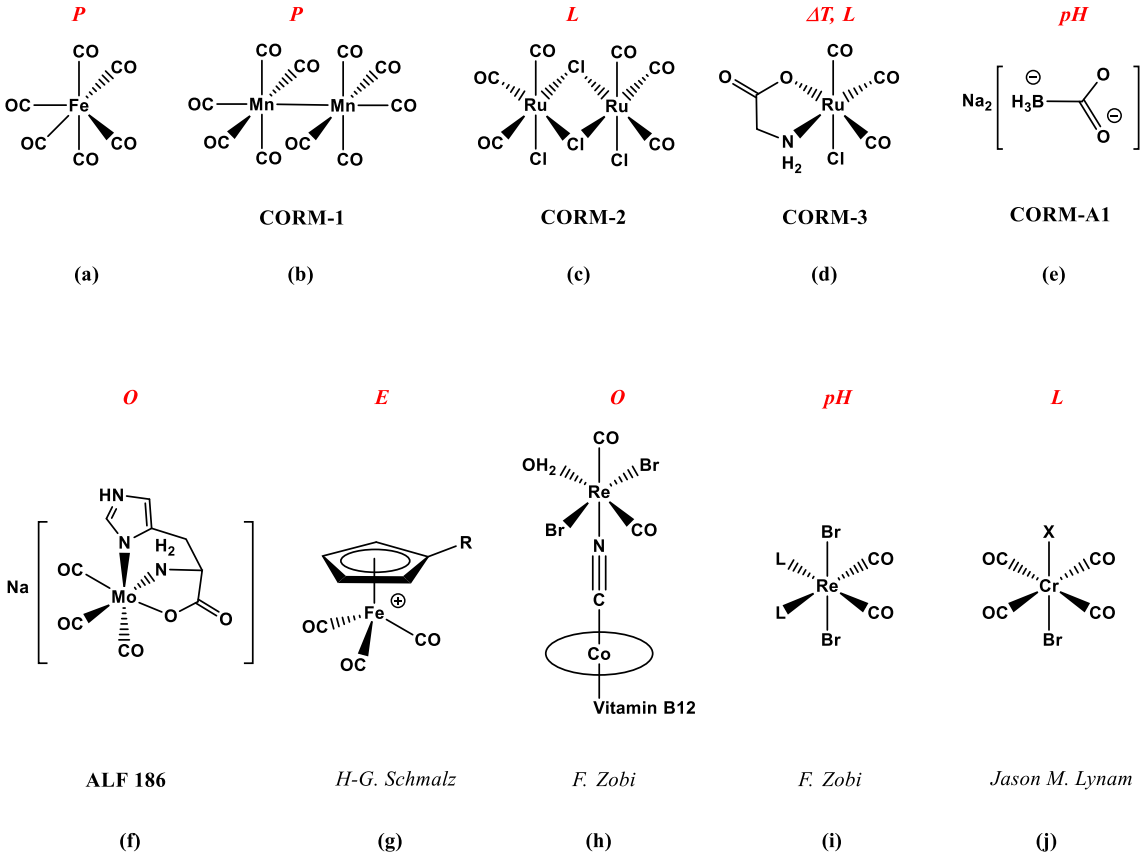

Figure 1.6 Selection of metal-based CORMs (X = halide, in italic: *p* = photolysis, ΔT = thermal trigger, *pH* = pH change, *E* = enzyme trgger, *o* = oxidation and *L* = ligand substitution/exchange).

Among the first generation of CORMs, the sodium boranocarbonate ($Na_2(H_3BCO_2)$, CORM-A1, Figure 1.6e) is highly soluble in aqueous solutions and does not contain transition metal center. It

liberated CO through two steps (protonation and hydrolysis) yielding H_3B–CO which rapidly lost CO upon acidification. [173,174] What is more, its rate of CO release was negative correlated with pH value and the decomposition almost stopped at pH > 8.5. The pH dependent CORMs, commonly utilize strong π donor ligand (such as O^{2-}, OH^-, OR^-, NH_2^- or NR_2^-) to free adjacent coordinated CO, and can be used in specific tissues. [169]

Contrary to CORM-A1, Na[Mo(CO)3(histidinato)] (ALF186, Figure 1.6 f) release CO much faster in at neutral pH than in acidic conditions which was observed by the oral and intraperitoneal experiment. [175] This molecule is classified as an oxygen triggered CORM and ROS species are considered to promote the reaction. In fact, there also abundant dissolved molecular oxygen in living organisms which can be directly interacts with the metal atom resulting in the breakdown of existing M-CO bonds and subsequently CO release. Besides, NOS species (such as NO, $ONOO^-$), disulfide bonds, metal ions and other elements can also intervene in the oxidation of CORM candidates through different mechanisms.

Another possible pathway under mild conditions for CO release is decomposition of metal carbonyls complexes triggered by enzymes, which based on enzymatic reactions of intracellular enzymes with ligands of a specific tissue. The most famous known enzyme-triggered CORMs (ET-CORMs, Figure1.6 g) are η^4-acyloxy-cyclohexadiene-$Fe(CO)_3$ complexes developed by Schmalz and his co-workers. [176] The unsaturated hydrocarbon $Fe(CO)_3$ complexes were stimulated by an esterase that attacked the targeting ester group and produced a tautomeric dienol-$Fe(CO)_3$ complex intermediate. Then the temporary cleaved Fe-CO bond and finally led to the CO delivery process. Furthermore, a series of iron complex with a penicillin G amidase (PGA)-cleavable unit was demonstrated that worked indeed in cell assays. [177] In conclusion, Studies concerning ET-CORMs present a new platform for providing selective controlled CO release in specific cellular environments.

Diverse approaches can trigger carbon monoxide releasing molecules. Up to now, CORMs principally focus on the metal carbonyls complexes, therefore the choice of the metal ion is critically important. In theory, almost all transition metal CORMs with an appropriated ancillary ligand can be triggered. However, the metals of group 3, 4 and 5 generally form M-CO bond only under strong reducing conditions, and the complexes of group 9 and 10 are mainly electronically

unsaturated leaving unstable status as well as the necessary abandon of artificial and radioactive complexes. The complexes of Cr, Mn, Fe, Mo, Ru, W and Re from group 6, 7 and 8 are the most potential agents for CORMs, especially the complexes with kinetically stable 18 electrons. [169,178–184] In addition, models of CORMs must consider the toxicity of metal residues to tissues and their metabolic pathway after decomposition.

1.2.4. Photolytic release of CO from metal carbonyl complexes

Photo-CORMs or photoactivated CORMs, as their name implies, are complexes that use light as an external trigger to achieve precise spatial and temporal control over CO releasing. Such photo-CORMs generally require different wavelengths of incident light due to the nature of compound and the strength of the M-CO bond (for metal carbonyls) or R-CO bond (for pure organic carbonyls).

As previously mentioned, CORM-1 and $Fe(CO)_5$ are first reported photo-CORMs which need exposure to cold light while in some degree are not amenable to modification. [171] Therefore, studies on the photo induced metal carbonyls have been further developed, particularly on the sides of control light sensitivity and water solubility. Then Schatzschneider and co-workers established systematically the behavior study of $[Mn(CO)_3(tpm)]PF_6$ (CORM-L1, figure1.7 a) with and without irradiation. [185,186] This tris(pyrazolyl)methane (tpm) manganese tricarbonyl complex liberated CO upon irradiation with UV light in aqueous buffer, subsequently bringing about two of three CO ligands separation. Its bioavailability experiments on HT29 human colon cancer cells demonstrated that CORM-L1 reduced efficiently the viability of cancer cells and the flexibility of the tpm ligand architecture facilitated the preparation of water-soluble bioconjugates. In 2010, Ford and his co-works raised the term “photoCORM” and presented an air-stable, water-soluble photoactivated tungsten carbonyl complex containing the trianionic tris(sulphonatophenyl)phosphine ligand (Figure 1.7 b). This moiety $Na_3W^0(CO)_5$(TPPTS) released approximately one CO under irradiation, and the excess generated CO was produced through the oxidative process of a slow thermal reaction. [180] The group of Schatzschneider synthesized a series of ruthenium(II) dicarbonyl complexes with functionalized 2,2′-bipyridine

(bpy) or bpy related ligands that can conjugate to a peptide nucleic acid (PNA). [187] These metal-PNA bioconjugates help to apply in the bio-sensing and biomedical applications.

The first published photo-CORM activated by visible light is complex cis, trans, cis-dicarbonyl bis(2-thiolato-κS-ethylamin-κN) iron (II) (CORM-S1, figure1.7 c) reported by Westerhausen and his co-workers in 2011. [188] CORM-S1 exhibited light-induced CO release upon irradiation with LEDs at 470 nm in aqueous solution and was also indirectly proved by the measurement of activity of voltage- and Ca^{2+}-activated potassium channels in excised membrane patches. Ford used a rhenium(I) luminescent molecule fac-[Re(bpy)$(CO)_3$(thp)](CF_3SO_3) (bpy = 2,2′-bipyridine, thp = tris(hydroxymethyl)phosphine, figure1.7 d) to track the transformation of this photo-CORM before to its photolysis product in aerated aqueous solution. [189] This moiety with a band at 515 nm released CO with a quantum yield of 0.11 when irradiated at 405 nm, accompanying with strong luminescence shift of photoproduct that exhibited a band at 585 nm, therefore can be used as an indicator to demonstrate the location where CO was released in cells. Through providing proper low-lying orbitals of ligands or increasing the extent of π back-bonding in the metal–CO bonds, Mascharak and his colleagues built $[Mn(L)(CO)_3]^+$ (L = ligands) systems with nitrogen-containing bidentate or tridentate ligands and auxiliary ligands to increase the ability of CO liberation. Among these complexes, fac-[MnBr(azpy)$(CO)_3$] (azpy = 2-phenylazopyridine) finished CO dissociation upon exposure to broadband light ($\lambda \geq 520$ nm) in the mixture media of H_2O and ACN. [190] Furthermore, the group of Ford enhanced the CO uncaging by doping water-soluble upconversion nanoparticles (UCNP) in a phospholipid-functionalized poly(ethylene glycol) layer (PEG layer) of lanthanide ions. [191] This system allowed the photochemical process to be activated by irradiation with infra-red light (NIR light) at 980nm and contributed to the photodynamic therapy. Coincidentally, Askes et al. recently reported an approach making use of mixing CORM-1 with a triplet-state photosensitizer to complete the CO delivery triggered by a red light at 635 nm. [4] Compared to the modification based on upconversion, this strategy utilized lower intensity red light to sensitize the complexes in solid form.

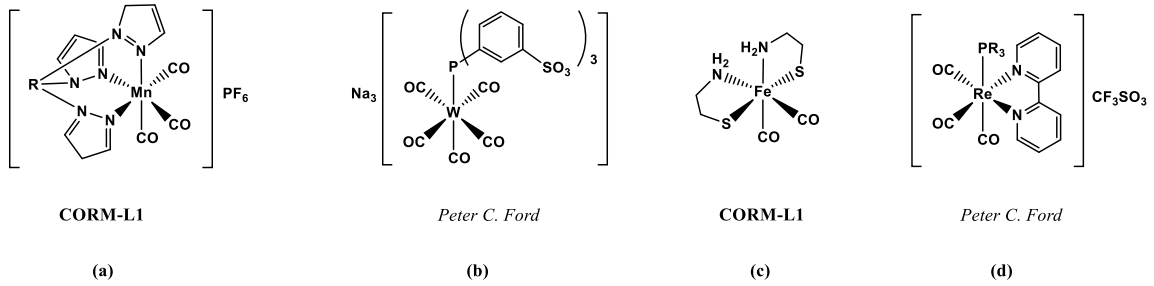

Figure 1.7 Selection of metal-based photo-CORMs.

In summary, the potential of photo-CORMs to act as an exogenous therapeutic candidate has so far been well established. In this field, early studies mainly focused on the feasibility test of photo-CORMs and developed in ultraviolet-initiated complexes. Up to now, the growth of photo-CORMs stimulated by visible and NIR light seems reasonably considerable and the interest in this aspect is still continuously increasing.

1.3. General overview of NO and CO releasing materials

1.3.1. NO and CO releasing molecules conjugates materials

To achieve the biocompatible drug transfer in tissues, NO and CO releasing molecules are commonly incorporated with or encapsulated in variety of materials, which are called nitric oxide and carbon monoxide releasing materials (NORMAs and CORMAs). The NORMAs and CORMAs are therapeutic extensions of controlled NO and CO delivering devices. Diverse strategies are contributed to the gas storage in solid status as well as the specific trigger for the molecule liberation in organisms, such as the macromolecular conjugates, nanostructured versatile carriers doping and surface encapsulation techniques.

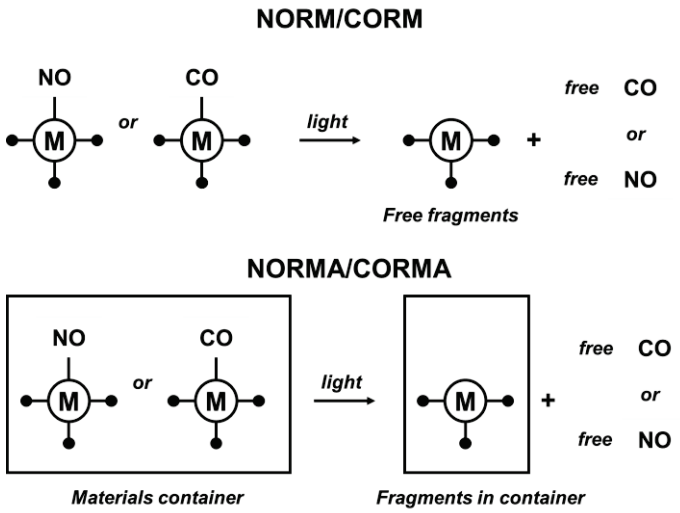

Figure 1.8 Illustration of NORM/CORM and NORMA/CORMA via incorporation of or encapsulation into materials with gas molecules. [192]

Nanoparticles are commonly easily synthesized with desired size, leading to affluent physicochemical characteristics and thus being propitious to act as tailored functional units for the conjugation of biological applications. For instance, the group of Schoenfisch synthesized N-diazeniumdiolate-modified gold nanoparticles through place-exchange reactions and these NO donors generated NO spontaneously in aqueous media. [193] The amount of NO storage and the dynamic rate of NO release can be controlled over the type and amount of amine. Thus, the capacities of surface plasmon resonance, fine biocompatibility, nontoxicity and the high affinity for thiol ligands offered by gold nanoparticles (GNP), open a new promising direction for the specific target delivery in vivo. In addition, other metallic nanoparticles that also hold abilities like gold (such as copper, platinum) and ability of magnetic targeting (iron) obtained abroad attention. [194–196]

Besides, the malfunction of silica nanoparticles also allowed their feasible to serve as skeleton frame of light-induced molecules. [197] This kind of carrier is usually prepared with sol-gel method to keep its porous structures and particularly does not affect photo-properties of attached chromophores. Another type fantastic inorganic nanoparticles are semiconductor quantum dots (QDs), which can enhance the photochemical NO/CO generation because of their high absorption coefficient and can improve the water solubility of complexes resulting from their simplicity of modification. Ford described water-soluble CdSe/ZnS core/Shell quantum dots and confirmed

that the QDs were effective sensitizers to photochemical reactions to enable energy transfer with high efficiency. [126]

Conjugation with biocompatible macromolecules is an attractive strategy to photo-NORMs and -CORMs for developing in therapeutic applications. For example, NO-releasing dendrimers macromolecules prepared from functional primary and secondary amines can increase the storage capacity for gas molecule through the dendritic effect, which has been proved by kinetic studies of Schoenfisch. [198] The group of Schatzschneider covalently connected photo-CORM, $[Mn(CO)_3(tpm)]^+$ (tpm = tris(pyrazolyl)methane), to functionalized amino acids and model peptides (part of the tumor suppressor protein) via Sonogashira cross-coupling and via1,3-dipolar cycloaddition. [184] This peptides-derivative facilitated CO dissociation under microwave irradiation not through altering the photolysis properties of manganese moiety but through accelerating the reaction time and reducing the amounts of by-products.

Metal–organic frameworks (MOFs, porous coordination polymers) are favorable solid-storage material for gaseous molecules owing to the high inner surface areas and ordered various-size pore channels with breathing effect. The so-called breathing effect in fact, is the reversible swelling of flexible MOF pores due to the solvent adsorption. Metzler-Nolte and coworkers prepared iron-based MOFs by a rapid microwave-assisted solvothermal method from iron(III) chloride and terephthalic acid and its derivatives. [199] These materials controlled the CO releasing rate by binding CO to accessible unsaturated coordination sites (CUS) in the frameworks. What is more, varying the MOF crystal size or morphology also helps to achieve the “gate-opening /closing” of CO delivery.

1.3.2. Encapsulated NO and CO releasing materials

Unlike approaches mentioned above, the group of Schiller non-covalently embedded the photosensitive metal carbonyls into polymer matrices via the electrospinning technique or miniemulsion. [192,200] The NORMAs or COMAs release NO or CO effectively into surrounding medium upon exposure to light and remain the toxic metal metabolites in the scaffold. It is noteworthy that the polymer is introduced a porous structure morphology to propel CO liberation because of loss of CO. This strategy allows water-insoluble NORMs and CORMs being

accessible to aqueous environment and biological tissues by encapsulation in water-soluble and biocompatible polymer frames.

Furthermore, Meinel and colleagues developed an oral carbon monoxide release system (OCORS) to deliver CORM tablets based on CORM-2 for the treatment of gastrointestinal diseases. [201] CORM-2 blending in a citric acid buffer and coated sodium sulfite crystals were encapsulated into the shell consisted of a semi-permeable membrane of cellulose acetate coating and PEG. The water medium diffused through the membrane and caused swelling of the coating layer around the Na_2SO_3 crystals leading to rapid dissolution. Thus, dissolved sulfite salts initiated CO-release through ligand substitution. The membrane thickness ensures CORM stability during storage and to some extent limits the CO release. The OCORS system is functional independent of environment in biology, providing precise control over sustained CO delivery.

1.4. Scope of the thesis

The present thesis focuses on the light-responsive nitric oxide releasing molecules (NORMs) and carbon monoxide releasing molecules (CORMs) based on transition metal ruthenium (Ru) and manganese (Mn) complexes. A general introduction and brief development of NORMs and CORMs are given in the first chapter. Chapter 2 describes series of photolabile $\{RuNO\}^6$ nitrosyls containing carboxamido-N and pyridine donors which fluorine substitution at different positions within the molecules thereof. In this section, the synthesis and characterization of metal nitrosyls are introduced as well as the influence of fluoro-substitution on NO-releasing studies are also investigated. In addition, the photo behaviors and mechanism analysis of the fluorinated ruthenium carbonyl complexes with same ligands as $\{RuNO\}^6$ nitrosyls are represented in chapter 3. Next, the Chapter 4–6 demonstrate water soluble photo-CORMs based on manganese(I) tricarbonyls center which conjugated to a fluorobenzene group, dabsyl chromophoric ligand and nitrobenzodiazole fluorophore group, respectively. A fluorinated manganese-based photo-CORM in chapter 4 combines with ^{19}F spectroscopy, aiming to provide a new strategy for tracking the photolysis of donor molecules through the NMR spectral change. Furthermore, the photo-CORMs presented in chapter 5 and 6 release CO under irradiation with visible light, simultaneously achieving the colorimetric and/or fluorometric response.

2. Fluorinated ruthenium NO releasing molecules

This chapter describes series of light-triggered fluorinated ruthenium nitrosyl complexes with a carboxamide-bis-pyridyl group. Fluorine ion was used to substitute different pyridyl-H within the ligand molecules and the formed ligands further reacted with ruthenium precursor to obtain the six-coordinate photo-NORMs Ru(X-Fbpb)(NO)Cl. These fluorinated ruthenium nitrosyls were highly stable under solution conditions and aerobic environment. Upon exposure to low intensity UV light at 405 nm, all photo-NORMs achieved NO release with ruthenium oxidation state changes from +2 to +3. The photochemical reactions were detected via fluorescence assay with the presence of NO_{550} probe.

2.1. Introduction

2.1.1. Ruthenium nitrosyls for NO release

As previously mentioned, light-induced metal NO releasing molecules have attracted considerable interest. A variety of NORMs based iron, manganese and ruthenium are reported. Among these transition metal nitrosyls, ruthenium complexes have a great advantage on stability especially over long periods under physiological medium as well as the disadvantage of relatively low quantum yield for NO release and the requirement of UV light for photoactivation. [145] Alteration of the coordinated ligand frame was required to overcome this deficiency.

The carboxamide-bis-pyridine based ligand was applied to synthesis $\{Ru\text{-}NO\}^6$ photo-NORMs. The pyridyl ligands and the deprotonated amido ligands will activate the Ru-NO moiety toward photolysis of NO by increasing electron density onto the nitrosyl group due to the strong π-donation. [202] Moreover, their propensity toward water solubility and biocompatibility render chelated complexes applicable to physiological situations where NO is needed as a drug agent. Consequently, the tetradentate ligands facilitate NO liberation and stabilize ruthenium complexes in high oxidation states that remain after photolysis. Thus, the photochemical reaction of NO can be achieved within a short time with low recombination rates. Within the octahedral structures,

ligands trans bound to NO resulting in red shifts of absorption and N-O stretching frequency due to the increase in the in-plane ligand field strength. [111]

2.1.2. Fluorescence assay for the determination NO release

The most common approach for determination NO release is to form fluorescent triazole derivatives by using o-diamino aromatics, which can react with NO^+ or N_2O_3 under aerobic conditions. [203,204] However, majority of these NO probes are generally affected by pH and interferent such as •OH and $•NO_2$, leading to a limited detection environment. 5-amino-6-(3-(dimethylamino)phenyl)-1-naphthonitrile (NO_{550}) is a highly selective fluorescence indicator for NO detection. [205] This NO scavenger is developed by Anslyn and co-workers and can react with NO^+ in solution to generate a fluorescent diazo ring compound 9-(dimethylamino) dibenzo [*c,h*] cinnoline-1-carbonitrile (AZO_{550}) shown in Scheme 2.1.

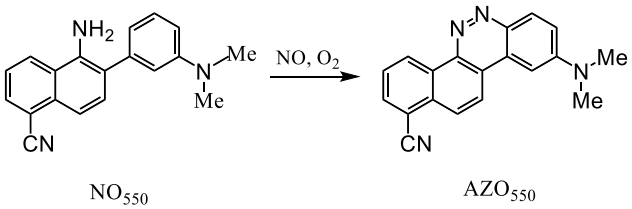

NO_{550} AZO_{550}

Scheme 2.1 Probe NO_{550} and its detection mechanism. [179]

For the fluorescence assay, at least 20 % DMSO in PBS buffer is required to dissolve NO_{550} because of its limited aqueous solubility. Once capturing NO, an emission band that centered at 550 nm grew and fluorescence intensity increased until no free NO liberated. The fluorescence intensity was found linear correlated with NO concentration ($R^2 = 0.997$) and the reaction kinetic was considered as multiexponential, allowing a superior for NO detection under both intra- and extracellular conditions.

2.2. Results and Discussion

The following chapter describes the preliminary synthesis and general characterization of the photoactivated nitric oxide releasing ruthenium complexes with a fluorinated carboxamide ligands. These fluorinated ruthenium molecules were stable under dark conditions and in oxygen-free aqueous media. Among the $\{Ru\text{-}NO\}^6$ complexes substituted with fluorine ion at different positions within the molecules, Ru(6-Fbpb)(NO)Cl (ortho position substitution) represented excellent photo-response upon illumination. The DFT calculations are given to discuss the molecular configurations and the influence on the NO release.

2.2.1. Synthesis and Characterization of ruthenium nitrosyls Ru(X-Fbpb)(NO)Cl

According to the literature procedure, the intermediate fluorinated ligand N'N-1,2-phenylene-bis (2-pyridine-carboxamide) (F-bpb) was obtained from the reaction of fluorinated picolinic acid and 1,2-phenylenediamine in the presence of triphenylphosphite with a fluorinated carboxamide ligands. [145,206]

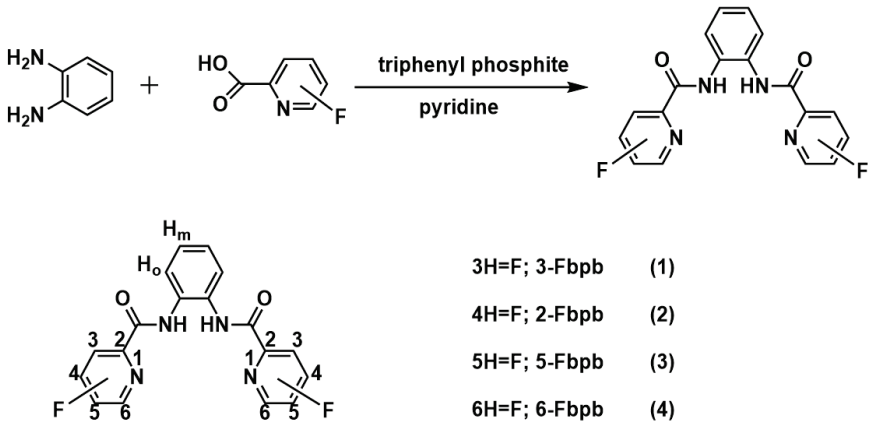

Scheme 2.2 Methodologies that were adopted for synthesis of ligands (1−4).

The ruthenium nitrosyls were further uniformly synthesized by the reaction of $Ru(NO)Cl_3(H_2O)_2$ with the deprotonated ligands (by addition of NaH) in dry N,N-dimethylformamide (DMF). The conjugation with two negative charged carboxamide-nitrogen atoms and pyridine nitrogens facilitates the stabilization of Ru^{II} states.

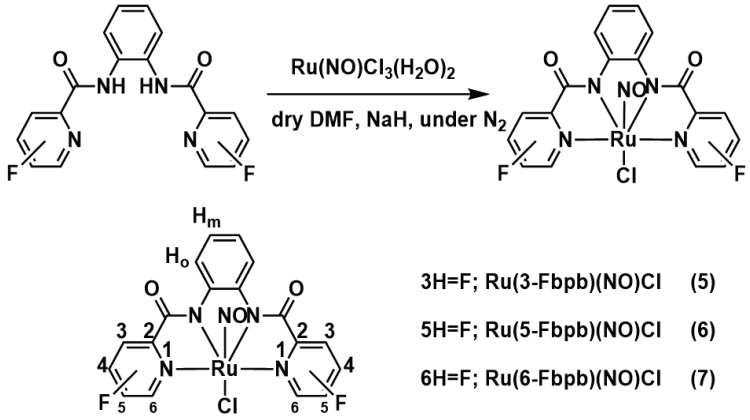

Scheme 2.3 Methodologies that were adopted for the synthesis of Ru(X-Fbpb)(NO)Cl (5-7).

Comparison of the ^{1}H NMR spectra of F-bpb and Ru(F-bpb)(NO)Cl revealed the absence of the -C(O)NH- amide proton of the free ligand at 10.26 ppm after the complexation reaction. A shift of the phenylene protons after the reaction further indicated the coordination of the metal ion, with the phenylene protons ortho to the amido nitrogen showing the most significant shift. [202] Furthermore, the pyridine proton adjacent to the coordinating pyridine nitrogen shifted to lower field. All observed aromatic protons observed represented the expected signal multiplets for the given substitution pattern.

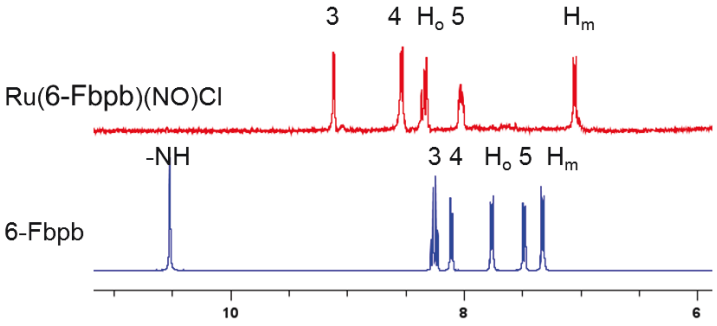

Figure 2.1 Partial ^{1}H NMR spectra of ligand (4) and Ru(6-Fbpb)(NO)Cl (7) in DMSO-d_6.

Additionally, the respective ^{19}F NMR spectrum of ruthenium nitrosyls demonstrated certain chemical shifts ($\Delta\delta_{Ru(3\text{-}Fbpb)(NO)Cl}$ = 26 ppm, $\Delta\delta_{Ru(5\text{-}Fbpb)(NO)Cl}$ = 2 ppm, $\Delta\delta_{Ru(6\text{-}Fbpb)(NO)Cl}$ = 8 ppm). In addition to the corresponding IR spectra, these results confirmed the metal coordination through the appearance of a new stretching frequency ν_{NO} at 1852 cm^{-1} and the disappearance of the NH band at 3313 cm^{-1}, which is accordance with reported data for similar complexes. Amide I stretching frequency $\nu_{C=O}$ shifted slightly from 1668 cm^{-1} of free ligands to 1620 cm^{-1}, and the

corresponding amide II $\nu_{C\text{-}N}$ at 1510 cm^{-1} and amide III $\delta_{N\text{-}H}$ at 1303 cm^{-1} of ligand were replaced by a band at 1384 cm^{-1}.

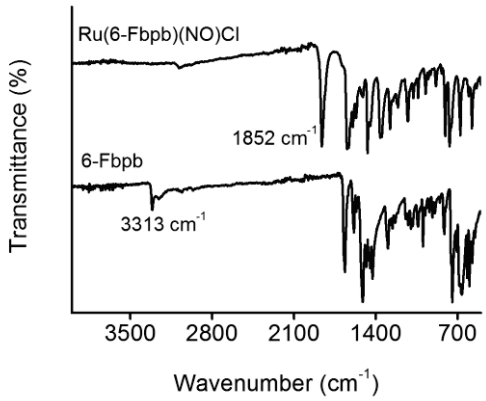

Figure 2.2 IR spectra of ligand 6-Fbpb and Ru(6-Fbpb)(NO)Cl.

Despite several attempts Ru(F-bpb)(NO)Cl could not be crystallized for single crystal x-ray analysis so far, the complex structures can be confirmed the employed characterization methods and DFT calculations. The ability of BP86 to predict the correct complex geometries was verified with the nonfluorinated complex Ru(bpb)(NO)Cl, for which crystal structure data is available. Important calculated bonding parameters of the complexes are given in Table 2.1. Calculated and experimental data agree well for Ru(bpb)(NO)Cl. DFT predicts a nearly linear NO coordination with a (Ru-N-O) angle of 174.1°. Employing the 3-Fbpb and 5-Fbpb co-ligands leads only to minor changes in the bonding parameters of the final complexes. The three complexes discussed until now all belong to the C_s point group, with the mirror plane containing the ruthenium and nitric oxide. However, mutual repulsion between the fluorine atoms in Ru(6-Fbpb)(NO)Cl results in a symmetry lowering and a geometry belonging to the C_1 point group.

Table 2.1: Calculated bond lengths in pm and angles for the ruthenium nitrosyl complexes. Experimental values are given in parentheses.[1] As Ru(6-Fbpb)(NO)Cl exhibits only C_1 symmetry the two (Ru–N) bonds towards to coligand are not equivalent and two bond lengths are given for ($Ru–N_{1,L}$) and ($Ru–N_{2,L}$). [202,207]

[1] All computer studies in the dissertation were calculated by Dr. Johannes Steinmetzer.

	Bond lengths / Å				Angle / °
Compound	($Ru–N_{NO}$)	$(N–O)_{NO}$	($Ru–N_{1,L}$)	($Ru–N_{2,L}$)	(Ru–N–O)
Ru(bpb)(NO)Cl	1.742 (1.753)	1.163 (1.144)	1.996 (1.990)	2.124 (2.130)	1.741 (1.724)
Ru(3-Fbpb)(NO)Cl	1.744	1.163	1.990	2.130	1.742
Ru(5-Fbpb)(NO)Cl	1.744	1.162	1.994	2.129	1.743
Ru(6-Fbpb)(NO)Cl	1.745	1.161	2.000 1.993	2.165 2.169	1.742

2.2.2. UV-Vis evaluation of Ru(X-Fbpb)(NO)Cl under illumination

A series of experiments of Ru(X-Fbpb)(NO)Cl were performed at 405 nm at room temperature until no further spectral changes were observed. The electronic absorption spectra were measured in nitrogen bubbled aqueous phosphate buffer (PB): DMSO (8:2, v/v) medium and also in DMSO: ACN (1:9, v/v) solution every 10 min over a course of two hours.

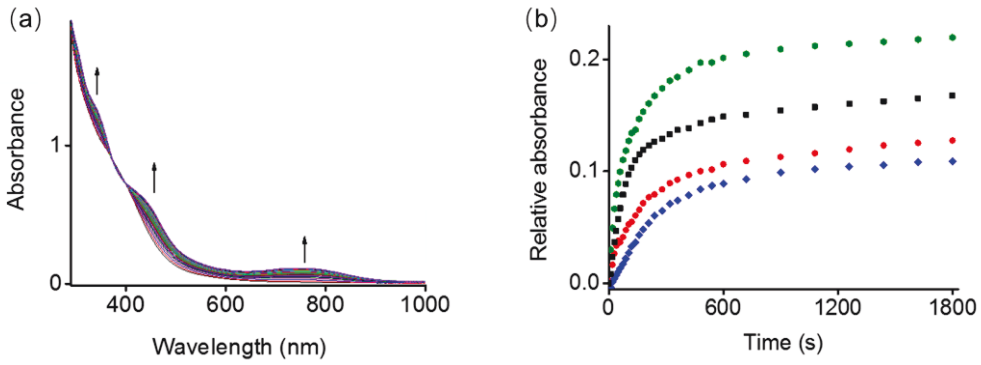

Figure 2.2 (a) Absorbance spectra of Ru(6-Fbpb)(NO)Cl (7) in DMSO/ACN solution (0.1 mM) irradiated at 405 nm for 30 min. (b) Photo-kinetics of ruthenium nitrosyls (Ru(6-Fbpb)(NO)Cl (7) (hexagon), Ru(bpb)(NO)Cl (square), Ru(3-Fbpb)(NO)Cl (5) (circle), Ru(5-Fbpb)(NO)Cl (6) (diamond) at 456 nm against time.

Upon irradiation with a low intensity UV lamp (10 mW/cm^2, λ = 405 nm), a 0.1 mM solution of Ru(6-Fbpb)(NO)Cl (7) exhibited two main absorption bands at 317, 456 nm respectively and a

broad absorption band in the range of 600-900 nm were shown in Figure 2.2 a. With illumination time increasing, the absorption bands grew gradually and increased with an isosbestic point at 395 nm. Simultaneously occurred the color change of the solution from light yellow to dark. When solutions of the complexes Ru(3-Fbpb)(NO)Cl (5) and Ru(5-Fbpb)(NO)Cl (6) in DMSO/ACN (1:9) are exposed to UV light under same conditions, similar spectral changes have been observed. The resulting optical spectral changes are consistent with substitution of bound NO by ACN (solvent) molecules.

$$\text{Ru(X-Fbpb)(NO)Cl} \xrightarrow{h\nu} \text{Ru(X-Fbpb)(sol)Cl} + \text{NO}$$

The NO dissociation rates (k_{NO}) of 5-7 are 2.83 × 10^{-3} s^{-1}, 2.62 × 10^{-3} s^{-1} and 3.57 × 10^{-3} s^{-1}, respectively. Under our conditions (DMSO/ACN solution, 10mW/cm^2, λ_{exc} = 405 nm, 7.5 cm distance from excitation lamp), Ru(bpb)(NO)Cl showed a reaction release rate of k_{NO} = 3.09 × 10^{-3} s^{-1}. While Mascharak et al. determined a NO dissociation rate of k_{NO} = 1.23 × 10^{-2} s^{-1} in ACN solution (7 mW/cm^2, λ_{exc} = 302 nm, 3 cm distance from excitation lamp).

A possible photo-release of NO and conversion to the solvato species is indicated by the formation of the bathochrome band around 440 nm. No back reaction is observed when the light is turned off, which means no NO recombination without irradiation. The photoproducts display a broad low-energy band in the range of 600–900 nm, which arises from F-bpb^{2-} to Ru(III) charge transfer transition (ligand to metal charge transition, LMCT). Similar low-energy LMCT bands have been observed in the photoproducts of other ruthenium nitrosyls. [207,208]

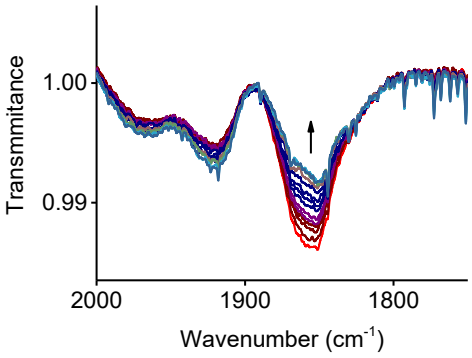

Figure 2.3 Time evolution of liquid-phase IR spectra during irradiation of Ru(6-Fbpb)(NO)Cl (7) solution (10 mM) recorded every 10 min for 120 min.

The photoreactions were also measured under dark conditions. No changes in absorbance were observed in the phosphate buffer media or ACN solution for longer than 12 h, confirming the stability of compounds in solution environment on the part of oxidation and decomposition. Moreover, it is clearly observed that the characteristic vibration bands of carbonyls at 1852 cm^{-1} gradually decreased with irradiation at high concentrations (10 mM) in DMSO solution from the liquid-phase IR spectra for Ru(6-Fbpb)(NO)Cl (Figure 2.3).

The donor strength of F-bpb^{2-} therefore effects the NO releasing rate to a limited extent while a change in the trans ligands from neutral pyridine to Cl^- increases it. The greater effect of the trans ligand and its negative charge on the overall photo lability of NO in this class of metal nitrosyls are particularly noteworthy. [209]

2.2.3. Fluorescence assay and investigation of the NO-release mechanism

To investigate the photo-triggered release of NO, a time-dependent fluorescence assay was performed at room temperature upon irradiation.

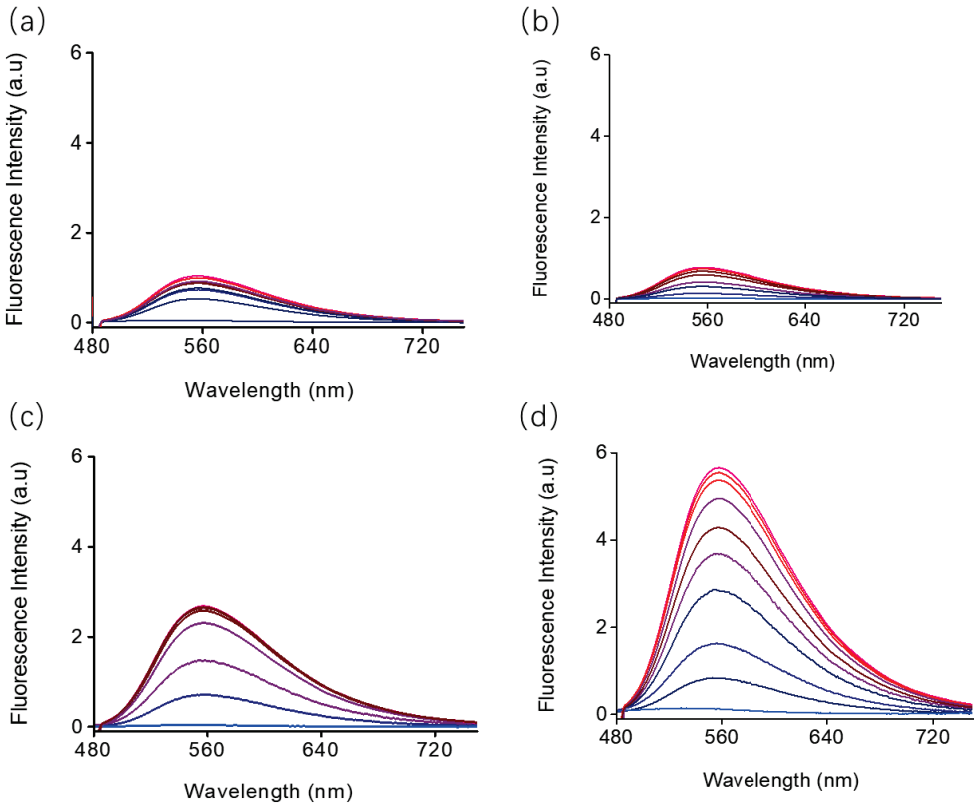

Figure 2.4 Fluorescence spectra of Ruthenium nitrosyls in DMSO/H_2O solution (0.1mM) irradiated with

405 nm for 2h. (a) Ru(3-Fbpb)(NO)Cl, (b) Ru(5-Fbpb)(NO)Cl, (c) Ru(bpb)(NO)Cl, (d) Ru(6-F bpb)(NO)Cl.

A common approach for fluorescent NO detection involves the use of o-diamino aromatics under aerobic conditions. These species react with NO^+ or a NO^+ donor, such as N_2O_3, to produce fluorescent triazole derivatives. For NO/NO^+ detection, we used the new NO_{550} probe from Anslyn et al. NO_{550} (5-amino-6- (3-(dimethylamino)phenyl)-1-naphthonitrile) displays a rapid and linear response to NO with a red-shifted 1500-fold turn-on signal emerging from a dark background. High selectivity was observed against other reactive oxygen and nitrogen species.

Unambiguously photo triggered the release of NO from ruthenium nitrosyls after illumination at 405 nm with low intensity (10 mW/cm^2) was shown using NO_{550} in buffered aqueous solution (DMSO:H_2O, 20:80, v/v, pH = 7.4). Subsequent fluorescence measurements showed that a signal turn on was already observed within the first 5 min and increased continuously until 90 min of irradiation. This indicates the photo triggered NO release from the fluorinated ruthenium carboxamide ligands. Comparison of experiments allows an estimation of the influence of complexes incorporation on the NO release, which is in accordance with the results observed from the UV-Vis spectra. The rate of NO release of Ru(3-Fbpb)(NO)Cl and Ru(5-Fbpb)(NO)Cl are similar, approximately 2 times slower than Ru(bpb)(NO)Cl, while Ru(6-Fbpb)(NO)Cl is nearly 2 times faster than Ru(bpb)(NO)Cl; which can be explained by the electronegativity change of fluoride substitution. This also leads to the distinct equivalent amount of NO release for each molecule ruthenium nitrosyl complexes.

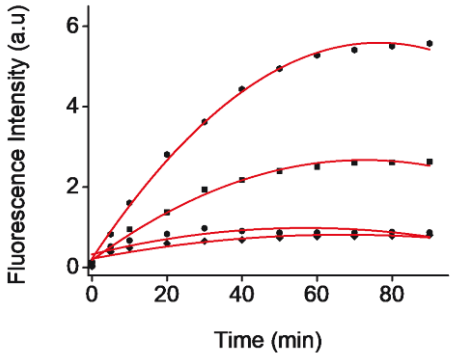

Figure 2.5 Plot of fluorescence intensity of NO_{550} at 550 nm *vs* time (solid line as monoexponential curve fitting, (Ru(6-Fbpb)(NO)Cl, hexagon; Ru(bpb)(NO)Cl, square; Ru(3-Fbpb)(NO)Cl, circle; Ru(5-Fbpb)(NO)Cl, diamond.).

Fluorine substitutions on pyridyl positions represent an obvious induction and electron withdrawing effects. The presence of electronegative fluorine at the ortho position of the aromatic ring may withdraw electron density of the π-electrons and reduce the stacking interaction, which affects the molecular configurations leading to a longer Ru-NO bond length (1.745 Å) of Ru(6-Fbpb)(NO)Cl compared to the other ruthenium nitrosyl complexes (Table 2.1). An increase of HOMO-LUMO energy gap and a red-shifted spectrum can be observed after substitution.

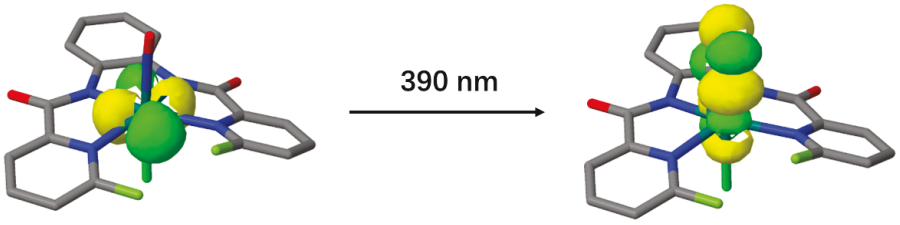

Figure 2.6 Illustrations of the bright MLCT state (S_1) at 405 nm as predicted by TD-DFT. Transfer of electron density from the metal center onto the L leads to CO release. Hydrogens were omitted for clarity.

To further investigate the mechanism of the photochemical NO release upon illumination, TD-DFT calculations were performed. All investigated complexes exhibit similar frontier orbitals. The HOMO-1 and HOMO are π_L-orbitals located on the carboxamide moiety of the co-ligands. The d_π-orbitals responsible for the (Ru-NO)-bonding have mainly ruthenium d character and lie energetically about 2 eV below the HOMO in all complexes. They are responsible for the π-backbonding interaction between the ruthenium and the nitric oxide. The correlating (Ru-NO)-antibonding d^*_π-orbitals correspond to the LUMO and LUMO+1, consisting of antibonding linear combinations between $d_{\pi, Ru}$ and the π^*_{NO} orbitals with mainly nitric oxide character. Excitations from the d_π-orbitals into these d^*_π-orbitals can result in photodissociation of nitric oxide (Figure 2.6). Overall the electronic structure of the present complexes is indicative of a $Ru^{II}(NO^+)$ configuration, as found for other ruthenium nitrosyls with linearly coordinated NO. These data indicate that the photoreactions originate from an admixture of d_π orbitals combinations of d-orbitals of ruthenium center and π^*_{NO} orbitals. In addition, MLCT transitions into π^*_{NO}-orbitals lead to the Ru(III)-NO(0) moiety, subsequently occurs an interconversion of singlet excited state and lower energy triplet excited states. [131,210] Such triplet species contribute to the photochemical activity of NORMs.

In brief, these results confirm that the ruthenium complexes can be triggered by UV light with low intensity to release coordinated NO in solution. The photochemical reactions of NORMs start from the admixture of d_{π} orbitals that consisted of d orbitals of ruthenium center and antibonding π orbitals of nitrosyl ligands.

2.3. Summary and Conclusion

In conclusion, a series of ruthenium complexes with fluorinated carboxamide ligands that release NO upon low intensity irradiation are introduced in this chapter. DFT and TD-DFT calculations are given to describe the conjugation of ruthenium nitrosyls and investigate the NO release mechanism. It is clearly confirmed that the photochemical reactions originate from the admixture of d_π orbitals that consisted of d orbitals of ruthenium center and antibonding π orbitals of nitrosyl. Furthermore, the substitution of fluorine at the ortho position of the aromatic ring conducted as withdrawing functional group influenced electron density of the π-electrons and reduced the stacking interaction. This leads to a longer bond length of Ru-NO in Ru(6-Fbpb)(NO)Cl compared to bond length in Ru(bpb)(NO)Cl, facilitating photolysis of NO.

2.4. Experimental section

2.4.1. General procedure

Materials and instrumentation.

1,2-diaminobenzene, triphenyl phosphite, NaH, $RuCl_3 \cdot 3H_2O$ and fluoropyridine-carboxylic acid were purchased from commercial sources. All solvents were purified and dried by standard techniques prior to use during syntheses to avoid exposure to dioxygen and moisture. ^{1}H NMR, ^{13}C NMR and ^{19}F NMR spectra were recorded AV 400 MHz Bruker NMR spectrometer using $CDCl_3$ and DMSO-d_6 as the solvents. Tetramethylsilane (TMS) as an internal standard for ^{1}H NMR, whereas trichlorofluoromethane (CCl_3F) as an internal standard for ^{19}F NMR. All IR (ATR) spectra were recorded on a Bruker Vertex 70 FT-IR spectrometer. UV-Vis spectra were recorded on an Analytik Jena Specord S 600 UV-Vis spectrometer and absorption spectra were recorded on a Cary 50 Varian spectrophotometer. Fluorescence spectra were recorded on a Perkin Elmer LS50B luminescence spectrometer. Mass spectra were obtained by the use of a Finnigan MAT SSQ 710 or MAZ95XL device. Elemental analysis was performed on a Vario EL III CHNS instrument.

General experimental methods for UV-Vis and fluorescence studies.

1 mM stock solution of NORMs was prepared in nitrogen-bubbled DMSO, which was used for all the studies. Unless not otherwise mentioned, the DMSO stock solutions were diluted with phosphate buffer (PB, pH 7.4) or ACN solution, and the effective final concentration was made as 0.1 mM. Thus, the diluted solution was used for all spectroscopic studies. All luminescence measurements were done using $\lambda_{ex} = 470$ nm with an emission slit width of 3 nm. Each spectrum was recorded at room temperature with a quartz cuvette at regular time intervals of UV light exposure (UVP Benchtop 2 UV Transilluminator, ≤ 10 mW/cm^2) at different wavelengths (365 nm and 405 nm).

Photolysis Experiment.

For UV-Vis spectroscopic measurements, the DSMO stock solution was further diluted with

phosphate buffer (PB:DMSO, 9:1, v/v, pH 7.4) and acetonitrile (ACN:DMSO, 9:1, v/v), Solution of NORMs (0.1 mM) in a quartz cuvette were exposed to different light sources (365 nm and 405 nm, 10 $mWcm^{-2}$) with an interval of every 10 min over a period of 2 h to confirm the photoactivities of ruthenium nitrosyls. The power of the light sources was determined with a PM100USB power meter. Absorbance values at specific wavelength were obtained from the respective spectra, and the observed rate constant k_{NO} was calculated from the equation:

$$A_t = A_\infty + (A_0 - A_\infty)\{\exp(-k_{NO} \times t)\} \qquad (Equation\ 2.1)$$

where A_t is the absorbance at time t after irradiation, A_0 and A_∞ are the initial and final absorbances. [207,211] The reaction rate constant values k_{NO} is obtained by fitting the absorbance values to the equation *versus* irradiation time.

The fluorescence assay was performed in an oxygen-free mixture of DMSO and phosphate buffer (PB:DMSO, 8:2, v/v). 3 mL solution containing excess NO_{550} (50 µM) and Ru-NO complex (16 µM) was recorded upon irradiation at every 5 min intervals for 90 min to investigate the photo-triggered NO release studies.

2.4.2. Synthesis and measurements

Synthesis of N, N'-(1,2-phenylene)bis(X-fluoropicolinamide), ligands.

The ligands (1-4) were prepared according to the modified method by Vagg et al. [186,209] A solution of fluoropyridine-carboxylic acid (6 mM, 0.8466 g) in pyridine (2.4 mL) was added to a pyridine solution (0.6 mL) that contained 1,2-diaminobenzene (3 mM, 0.324 g). After the addition of triphenyl phosphite, the mixture was stirred at 80 ℃ overnight. The reaction mixture was filtered and the residue was washed with dry diethyl ether several times to yield a corresponding white solid ligand.

N,N'-(1,2-phenylene)bis(3-fluoropicolinamide), 3-Fbpb (1):

^{1}H NMR (400 MHz, $CDCl_3$), δ (ppm):10.26 (s, 2 H), 8.23 (d, J = 8.24 Hz, 2H), 8.09 (dd, J = 7.80 Hz, 2 H), 7.76 (dd, J = 7.60 Hz, 2H), 7.44 (dd, J = 6.05 Hz, 2 H), 7.36 (dd, J = 6.05 Hz, 2H). ^{13}C NMR (150 MHz, $CDCl_3$), δ (ppm): 149, 148, 137, 130, 126, 126, 124, 122. ^{19}F NMR (400 MHz,

$CDCl_3$), δ (ppm): -122. IR (ATR): ν = 1637, 1602, 747, 615, 502 cm^{-1}. ESI-MS (m/z) $C_{18}H_{12}N_4F_2O_2$, calculated for: 354.31, observed: 354.

N,N'-(1,2-phenylene)bis(4-fluoropicolinamide), 4-Fbpb (2):

^1H NMR (400 MHz, $CDCl_3$), δ (ppm):10.39 (s, 2 H), 8.23 (d, J = 8.24Hz, 2 H), 8.09 (dd, J = 7.80 Hz, 2 H), 7.76 (dd, J = 7.60 Hz, 2 H), 7.44 (dd, J = 6.05 Hz, 2 H), 7.36 (dd, J = 6.05 Hz, 2 H). ^{13}C NMR (150 MHz, $CDCl_3$), δ (ppm): 149, 148, 135, 132, 127, 126, 124, 122. ^{19}F NMR (400 MHz, $CDCl_3$,) δ (ppm): −100. IR(ATR): ν = 1653, 1601, 743, 653, 581 cm^{-1}. ESI-MS (m/z) $C_{18}H_{12}N_4F_2O_2$, calculated for: 354.31, observed: 354.

N,N'-(1,2-phenylene)bis(5-fluoropicolinamide), 5-Fbpb (3):

^1H NMR (400 MHz, $CDCl_3$), δ (ppm): 10.05 (s, 2 H), 8.23 (d, J = 8.24 Hz, 2 H), 8.09 (dd, J = 7.80 Hz, 2 H), 7.76 (dd, J = 7.60 Hz, 2 H), 7.44 (dd, J = 6.05 Hz, 2 H), 7.36 (dd, J = 6.05 Hz, 2 H). ^{13}C NMR (150 MHz, $CDCl_3$), δ (ppm): 149, 148, 137, 130, 126, 125, 124, 122. ^{19}F NMR (400 MHz, $CDCl_3$,) δ (ppm): -121. IR (ATR): ν = 1637, 1598, 734, 623, 577 cm^{-1}. ESI-MS (m/z) $C_{18}H_{12}N_4F_2O_2$, calculated for: 354.31, observed: 354.

N,N'-(1,2-phenylene)bis(6-fluoropicolinamide), 6-Fbpb (4):

^1H NMR (400 MHz, $CDCl_3$), δ (ppm):10.39 (s, 2 H), 8.23 (d, J = 8.24, 8.22, 0.95 Hz, 2 H), 8.09 (dd, J = 7.80, 1.05 Hz, 2 H), 7.76 (dd, J = 7.60, 4.76, 1.15 Hz, 2 H), 7.44 (dd, J = 6.05, 3.49 Hz, 2 H), 7.36 (dd, J = 6.05, 3.49 Hz, 2 H). ^{13}C NMR (150 MHz, $CDCl_3$), δ (ppm): 149, 148, 137, 130, 126, 125, 124, 122. ^{19}F NMR (400 MHz, $CDCl_3$,) δ (ppm): -68.19. IR (ATR): ν= 1637, 1601, 757, 633, 521 cm^{-1}. ESI-MS (m/z) $C_{18}H_{12}N_4F_2O_2$, calculated for: 354.31, observed: 354.

Synthesis of Trichloronitrosylruthenium, $Ru(NO)Cl_3(H_2O)_2$.

$Ru(NO)Cl_3(H_2O)_2$ was synthesized according to a published method. [131,202] Ruthenium(III) chloride hydrate ($RuCl_3(H_2O)_3$, 2.00 g, 0.0096 mol) was dissolved in 18 ml diluent hydrochloric acid (HCl, 1 M) and heated to 100 ºC. 5 mL aqueous solution of sodium nitrite ($NaNO_2$, 1.99 g, 0.0288 mol) was added dropwise over a period of one hour to form a dark red solution. After 1 h, the solvent was removed from the purple reaction mixture under vacuum with rotary evaporator at 90 ºC. Then the remaining dark purple oil was dissolved in ethanol. The NaCl precipitate formed in the reaction was separated from product via vacuum filtration. Ethanol was removed in vacuum

with a rotary evaporator. The extremely hygroscopic purple residue was dried and stored in a desiccator.

IR (ATR): ν = 1884 cm^{-1}.

Synthesis of NORMs, Ru(X-Fbpb)(NO)Cl.

A slurry of NaH (0.015 g, 0.625 mM) in 2 mL DMF was added to a stirred solution of Ligand (0.1198 g, 0.314 mM) in 3 mL of dry DMF. The color of the solution turned clear yellow when the evolution of hydrogen gas stopped. A solution of $Ru(NO)Cl_3(H_2O)_2$ (0.082 g, 0.314 mM) in 4 mL dry DMF was added to the reaction mixture. The color of the solution turned dark brown immediately. The solution was refluxed under nitrogen atmosphere for 20 h. The dark brown solution was cooled to room temperature and filtered to remove NaCl. Then the mixture was concentrated to 2 mL. Diffusion of Et_2O into this solution yielded a dark brown solid (72%).

Ru(3-Fbpb)(NO)Cl (5):

^{1}H NMR (400 MHz, DMSO-d_6), δ (ppm): 8.95 (1H, d, J = 8.0 Hz, ArH); 8.57 (2H, d, J = 5.6 Hz, ArH); 8.26 (1H, t, J = 8.8 Hz, ArH); 8.15 (1H, d, J = 7.6 Hz, ArH); 7.43- 7.21 (3H, m, ArH). ^{13}C-NMR (125 MHz, DMSO-d_6): δ (ppm) 164, 157, 145, 144, 128, 126, 123, 122. ^{19}F NMR (400 MHz, DMSO-d_6), δ (ppm): -148. IR(ATR): ν =1846cm^{-1} (ν_{NO}, s), 1935 cm^{-1} and 1586 cm^{-1} (ν_{CO} stretchings). ESI-MS (m/z) $C_{18}H_{10}F_2N_4O_3ClRu$, calculated for: 519, observed: 508. Elemental analysis $C_{18}H_{10}F_2N_4O_3ClRu$, calculated: C = 41.67%, H = 1.94%, F = 7.32%, Ru = 19.48%, N = 13.50%, O = 9.25%, found: C = 43.44%, H = 2.11%, N = 13.17%

Ru(5-Fbpb)(NO)Cl (6):

^{1}H NMR (400 MHz, DMSO-d_6), δ (ppm): 8.95 (1H, d, J = 8.0 Hz, ArH); 8.57 (2H, d, J = 5.6 Hz, ArH); 8.26 (1H, t, J = 8.8 Hz, ArH); 8.15 (1H, d, J = 7.6 Hz, ArH); 7.41- 7.21 (3H, m, ArH). ^{13}C-NMR (125 MHz, DMSO-d_6): δ (ppm) 163, 157, 145, 143, 128, 125, 113, 122. ^{19}F NMR (400 MHz, DMSO-d_6), δ (ppm): -119. IR(ATR): ν =1861 cm^{-1} (ν_{NO}, s), 1645 cm^{-1} (ν_{CO} stretchings). ESI-MS (m/z) $C_{18}H_{10}F_2N_4O_3ClRu$, calculated for: 519, observed: 478. Elemental analysis $C_{18}H_{10}F_2N_4O_3ClRu$, calculated: C = 41.67%, H = 1.94%, F = 7.32%, Ru = 19.48%, N = 13.50%, O = 9.25%, found: C = 42.73%, H = 2.51%, N = 12.87%

Ru(6-Fbpb)(NO)Cl (7):

^{1}H NMR (400 MHz, DMSO-d_6), δ (ppm): 8.95 (1H, d, J = 8.0 Hz, ArH); 8.57 (2H, d, J = 5.6 Hz, ArH); 8.26 (1H, t, J = 8.8 Hz, ArH); 8.15 (1H, d, J = 7.6 Hz, ArH); 7.24- 7.41 (3H, m, ArH). ^{13}C-NMR (125 MHz, DMSO-d_6): δ (ppm) 164, 158, 147, 141, 127, 126, 121, 120. ^{19}F NMR (400 MHz, DMSO-d_6), δ (ppm): -60. IR(ATR): ν =1852 cm^{-1} (ν_{NO}, s), 1956 cm^{-1} and 1633 cm^{-1} (ν_{CO} stretchings). ESI-MS (m/z) $C_{18}H_{10}F_2N_4O_3ClRu$, calculated for: 519, observed: 541[Na^+]. Elemental analysis $C_{18}H_{10}F_2N_4O_3ClRu$, calculated: C = 41.67%, H = 1.94%, F = 7.32%, Ru = 19.48%, N = 13.50%, O = 9.25%, found: C = 41.99%, H = 1.89%, N = 13.82%.

3. Fluorinated ruthenium CO releasing molecules

This section focuses on a collection of ruthenium-based CO releasing molecules with identical ligands system of ruthenium nitrosyl complexes described in chapter 2. This series products originate from a compound Ru(bpb)(CO)(H_2O), which is a complex published by group Viswanathamurthi and group Akermark and worked as an efficient catalyst. [212,213] The photolysis of this compound has been evaluated by Dr. Bohlender in our group and the results showed that Ru(bpb)(CO)(H_2O) cannot be triggered by light to release CO. Inspired Ru(X-bpb)(NO)(Cl) complexes, substitution with fluorine was applied for facilitating the CO dissociation. These ruthenium carbonyls are stable under physiological conditions, except Ru(5-Fbpb)(CO)(H_2O) is degradable in solution environment. In addition, Ru(6-bpb)(CO)(H_2O) can release CO upon illumination with light at 405 nm. It is clearly confirmed this modification successfully improved the photoactivity.

3.1. Introduction

3.1.1. Ruthenium carbonyls for CO release

Transition metal ruthenium lies in the second row with a large d-orbital splitting leading to ruthenium carbonyls are commonly considered as having a low spin Ru(II)-CO^0 electron configuration. This also contributes to more air-stable and less labile of light-responsive ruthenium carbonyl complexes compared to other metal carbonyl complexes. Ruthenium pyridyl complexes are widely employed in biomedical and biophysical field for their well-known photophysical and photochemical properties. Ruthenium (II) bipyridyl complexes were found not accumulate in the nucleus and were transferred by endocytosis or by active transport. Cheng et al. represented that outer membrane protein (OmpF) involved in the transportation of polypyridyl ruthenium complexes into Escherichia coli. [214] This provided a solution to metal metabolites after photodegradation. Thereby, ruthenium based pyridyl derivatives were introduced as potential CO donors to biological targets. Strategies to improve the sensitivity to visible light gained an

increasing interest.

3.1.2. Myoglobin assay for the determination CO release

To quantify the amount and rate of CO liberated from CORMs, real-time and reliable methods are required. Myoglobin assay is a very common technique to monitor CO release from metal carbonyl complexes based on spectral changes in absorption, which was first introduced by Motterlini and co-workers in 2002. [171,215,216] This method uses haem containing protein myoglobin (Mb) as a CO scavenger. Horse heart myoglobin is commonly used in this assay because its protein impurities can be eliminated as a source of isosbestic point loss/ translation at enough low concentrations. Firstly, sodium dithionite was added to convert commercially myoglobin source (metmyoglobin, Fe^{3+}) to deoxymyoglobin (deoxy-Mb, F^{2+}). The formed deoxy-Mb can react rapidly with free CO to generate carboxymyoglobin (CO-Mb) with a rate constant of k = 0.38 μM/s (binding constant = 16.9 μM/s). This reaction of deoxy-Mb with CO can be followed by UV-Vis spectroscopy through observing the spectral change in the Q-bands of heme group. The absorption band of deoxy-Mb at 557 nm decreases and divides into two new absorption bans of CO-Mb respectively at 540 nm and 577 nm. This assay is generally performed at simulant physiological conditions (pH= 74, 37 °C). In addition, a small excess of reducing agent (sodium dithionite) is needed to eliminate the influence of incoming oxygen which also can bound with deoxy-Mb rapidly and prevent release CO upon oxidation. It is noted that accurate starting concentration of myoglobin can be corrected with reference extinction coefficients of ε_{540} = 15.40 $mM^{-1}cm^{-1}$ and ε_{560} = 13.80 $mM^{-1}cm^{-1}$. The resulting proportion of CO-Mb converted from deoxy-Mb can be evaluated by determination the absorption band at 540 nm.

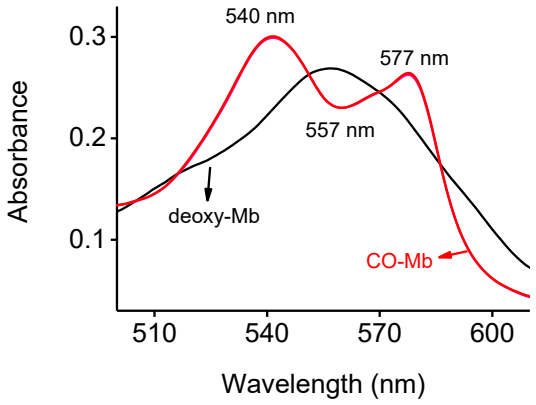

Figure 3.1 Q-bands region of absorption spectra for deoxymyoglobin and carboxymyoglobin in phosphate buffer (pH = 7.4).

However, the concentration of CO-Mb formed over time cannot be applied to calculate a reliable rate constant due to the possible multiple CO ligands in CORMs. [216] When a CORM complex contains more than one CO ligands in the molecule, the fragments result from photoreaction after its first CO release might accelerate or decelerate further CO liberation. Therefore, a concept of half-life ($t_{1/2}$) is commonly used to quantitatively determinate CO releasing. It is described as the time taken for a conversion of half initial concentration of generated CO-Mb from CORM solution.

3.2. Results and Discussion

The ruthenium carbon monoxide releasing complexes contain identical ligands represented in the chapter 2. The following chapter describes the preliminary synthesis and general characterization of the light-triggered molecules. Since substitution with fluorine ion at different positions within the molecules, Ru(X-Fbpb)(CO)(H_2O) show diverse photo behaviors in oxygen-free aqueous buffer media. Among them, Ru(6-Fbpb)(CO)(H_2O) exhibits photo-response upon illumination. The DFT calculations are given to discuss the molecular configurations.

3.2.1. Synthesis and Characterization of ruthenium carbonyls Ru(X-Fbpb)(CO)(H_2O)

Ru(X-Fbpb)(CO)(H_2O) were synthesized by the reaction of triruthenium dodecacarbonyl $Ru_3(CO)_{12}$ with the fluorinated ligands X-Fbpb in N, N-dimethylformamide (DMF) under reflux. In this reaction, the Ru^0 precursor acts as a reducing agent to reduce the ligands without additional deprotonation candidates.

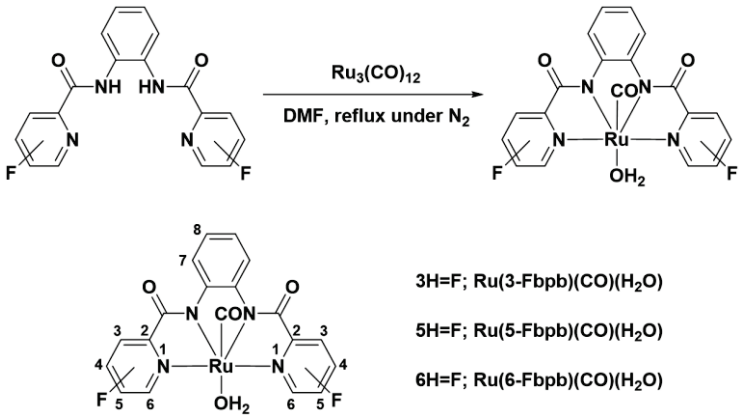

Scheme 3.1 Reaction pathways for the synthesis of ruthenium carbonyl complexes Ru(X-Fbpb)(CO)(H_2O).

High reaction temperatures (almost above 110 °C) are essential to allow decomposition and reaction of $Ru_3(CO)_{12}$. During reaction, the crystal water or residual water molecules within the DMF solution bound trans to ruthenium center (σ-donating), remaining even after intensive drying of the solvent. Crystal of Ru(bpb)(CO)(H_2O) can be obtained from DMF at −20 °C with high stability under air conditions over several months. Due to crystallizations of fluorinated

ruthenium carbonyls are failed, the complex structures can be confirmed the employed characterization methods and DFT calculations. In addition, Ru(bpb)(CO)(H_2O) can be dissolved in common organic solvents while Ru(Fbpb)(CO)(H_2O) can only be dissolved in DMSO and DMF solutions. The complexes are stable in solid state even under air conditions. However, the corresponding solutions will turn to a green color at different rates, resulting from an oxidation reaction to form $Ru^{(III)}$ species.

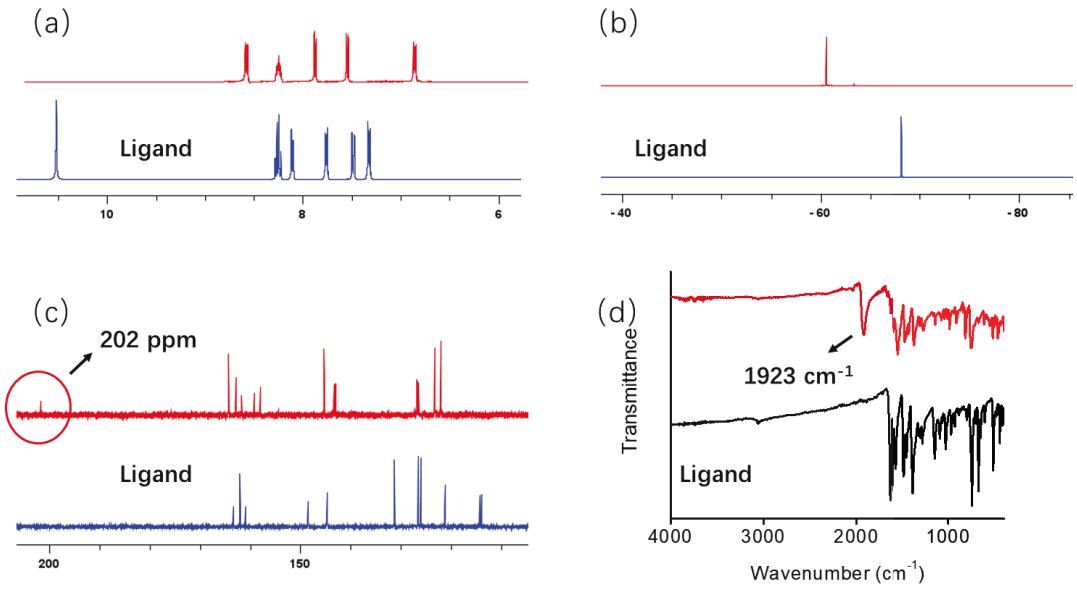

Figure 3.1 Partial (a) ^{1}H NMR spectra, (b) ^{19}F NMR spectra, (c) ^{13}C NMR spectra in DMSO-d_6 and (d) IR spectra of ligand and Ru(6-Fbpb)(CO)(H_2O).

NMR spectra of ligands and the corresponding ruthenium (II) carbonyl complexes were recorded in DMSO-d_6 at room temperature to confirm the presence of the coordinated ligand in the complexes. Comparison ^{1}H NMR of the ligands and Ru(6-Fbpb)(CO)(H_2O) reveals the absence of characteristic peak [-C(O)NH-] at 10.26 ppm after the complexation reaction, suggesting the successful coordination through deprotonated amide nitrogen. A shift of the phenylene protons after reaction further indicates the coordination of the metal ion, where the phenylene protons ortho to the amido nitrogen (H7, at 7.7 ppm) shows the most downfield significant shift. Furthermore, the pyridine protons demonstrate the chemical shift to lower field and phenylene proton (H8, at 7.3 ppm) shifts to a higher field (6.9 ppm). All aromatic protons observed show the expected signal multiplets for the given substitution pattern. In ^{13}C NMR spectra, signals at

161.4−164.3 ppm and 157.8−159.1 ppm of Ru(6-Fbpb)(CO)(H_2O) are assigned to the carbonyl carbon (C=O) and the pyridyl carbon. [213] Peaks around 31.2−39.6 ppm correspond to benzene carbon. Additionally, a peak at 201.6 ppm is due to the C≡O carbon resonance. The respective ^{19}F NMR spectra of ruthenium nitrosyls were recorded to further confirm the involvement of the pyridine group. Certain chemical shifts were observed (Δ_δ = 8 ppm for Ru(6-Fbpb)(CO)(H_2O)). In addition to the corresponding IR spectra, this result confirms the metal coordination and introduction of CO through the appearance of the stretching frequency $\nu_{C\equiv O}$ at 1923 cm^{-1} and the disappearance of the NH band at around 3313 cm^{-1}. The band at 1539−1669 cm^{-1} are assigned to carbonyl amide I ($\nu_{C=O}$) stretching frequency upon complex formation. The corresponding amide II (ν_{C-N}) at 1468 cm^{-1} and amide III (δ_{N-H}) at 1262 cm^{-1} result from the deprotonation of amide functionality. Further the band of pyridine ring deformation at 600-630 cm^{-1} in the ligands shifts to a higher frequency at 640-660 cm^{-1} in ruthenium complexes. Similar changes can be observed in the other ruthenium carbonyl complexes.

DFT calculations were performed to analyze the structure of ruthenium carbonyl complexes. Calculated and experimental data agree well for Ru(bpb)(CO)(H_2O). [213] DFT predicts a nearly linear CO coordination with a (Ru-C-O) angle of 175.8 °. The tetradentate ligands (F-bpb) in its deprotonated form provides two neutral pyridine N and two anionic carboxamido N donors in the nearly plane of the neutral complex; the axial positions are occupied by carbonyl and water ligand. The geometry around the Ru(II) center is axially distorted octahedral. The planes of pyridyl and benzene rings slightly deviate from each other and tilt away from the tertiary pyridyl plane. Coordination bonds of the ruthenium center to the negative charged carboxamide group (Ru-N_{amide}) are about 0.1 Å shorter compared to the interaction within the Ru-N_{py} bonds. The axial carbon monoxide is almost linearly bound to the ruthenium center with a distance of 1.795 Å and the length of the C≡O bond is 1.173 Å. The long bond length of Ru-O_{water} (2.163 Å) is assigned to the weak σ-bond and lack of π-bonding between the ruthenium and water ligand. Moreover, the distance of Ru-C_{CO} (1.795 Å) results from the σ-donor and of π-acceptor carbonyl ligand.

Table 3.2: Calculated bond lengths (Å) and angles (°) for the ruthenium carbonyl complexes. Experimental values are given in parentheses. As Ru(6-Fbpb)(CO)(H_2O) exhibits only C_1 symmetry the two (Ru-N) bonds towards to coligand are not equivalent and two bond lengths are given for (Ru-$N_{1,L}$) and (Ru-$N_{2,L}$).

	Bond lengths / Å					Angle / °
Compound	(Ru-C_{CO})	(C-O)$_{C\equiv O}$	(Ru-$N_{1,L}$)	(Ru-$N_{2,L}$)	(Ru-O_{water})	(Ru-C-O)
Ru(bpb)(CO)(H_2O)	1.790	1.172	1.978	2.123	2.164	1.758
Ru(3-Fbpb)(CO)(H_2O)	1.792	1.174	1.980	2.130	2.163	1.757
Ru(5-Fbpb)(CO)(H_2O)	1.794	1.172	1.984	2.132	2.162	1.756
Ru(6-Fbpb)(CO)(H_2O)	1.795	1.173	1.980 1.973	2.125 2.129	2.163	1.757

3.2.2. UV-Vis evaluation of Ru(X-Fbpb)(CO)(H_2O) under illumination

To evaluate CO release abilities at different wavelengths (365 nm and 405 nm), comparison experiments of ruthenium carbonyl complexes were performed until no further spectral changes were observed. The electronic absorption spectra were undertaken in nitrogen-bubbled aqueous PB: DMSO (80:20, v/v) in 10 mins intervals and were shown in Figure 3.2.

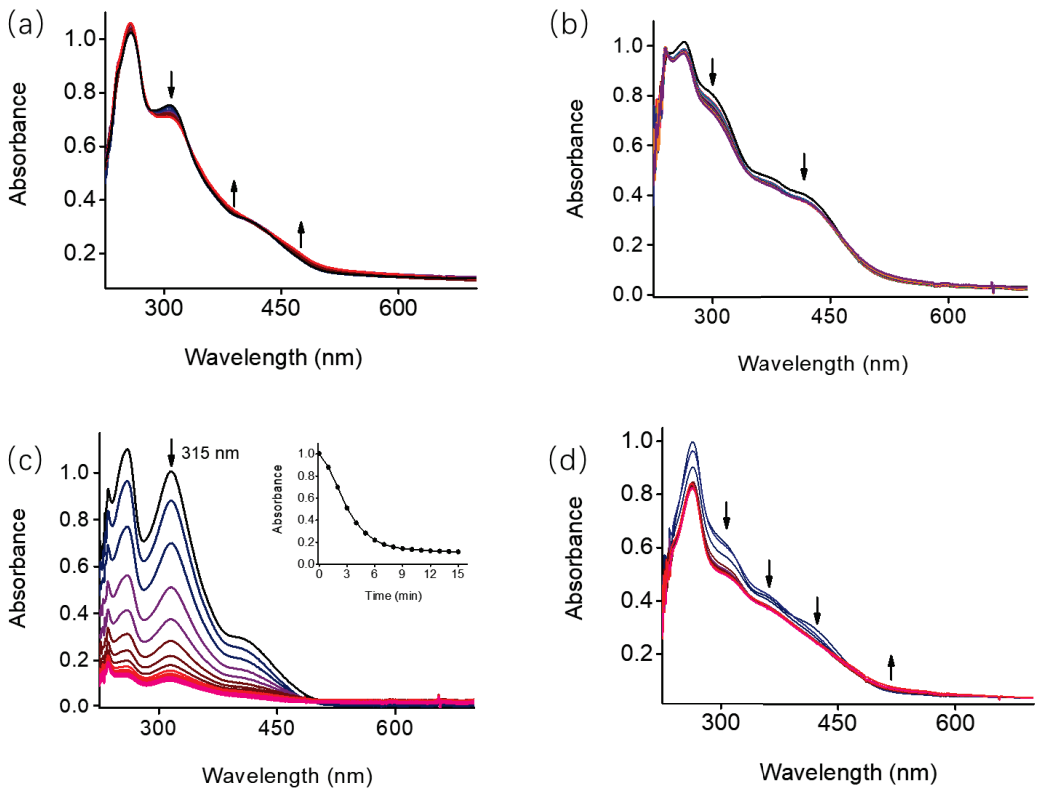

Figure 3.2 Absorbance spectrum of Ruthenium carbonyls in DMSO/H_2O (20:80, v/v) solution (0.1 mM) upon irradiation with 405 nm at 10 mW cm^{-2} in 10 mins intervals for 120 min. (a) Ru(bpb)(CO)(H_2O), (b) Ru(3-Fbpb)(CO)(H_2O), (c) Ru(5-Fbpb)(CO)(H_2O) inset: absorbance at 315 nm as a function of irradiation time, (d) Ru(6-Fbpb)(CO)(H_2O).

For Ru(bpb)(CO)(H_2O), two main absorption bands at 308 nm and 415 nm respectively were observed in the Figure 3.2 a. The former is explained by a metal to ligand charge transfer (MLCT) from d_{Ru} to π^*_{CO}. This absorption band decreased gradually and presented a slight redshift upon illumination. The absorption band at 415 nm changed to blurred and smooth because the absorption minimum at 385 nm increased and a broad absorption at 436−600 nm grew. Additionally, two isosbestic points were formed at 279 nm and 339 nm.

There were also two main absorption bands of Ru(3-Fbpb)(CO)(H_2O) at 298 nm and 415 nm, which was shown in Figure 3.2 b. Both absorption bands decreased with irradiation time increasing and no isosbestic point was observed, indicating the stability on the compound in solution. Figure 3.2 c is the evolution of absorption spectra for Ru(5-Fbpb)(CO)(H_2O) under illumination with light at 405 nm within 15 min. Two strong absorption bands at 315 nm and 408 nm represented a dramatical decline; ultimately the latter almost completely disappeared. Moreover, an alike tendency was found upon exposure to light at 365 nm, indicating a violent reaction of the compound. However, IR spectra of Ru(5-Fbpb)(CO)(H_2O) in solvent environments (Figure 3.3) demonstrated that the spectral variation cannot attribute to the CO release but the degradation in solution. Once completely dissolved in solvents, IR spectra of compound solution was immediately performed. The characteristic stretching frequency $\nu_{C\equiv O}$ at around 1923 cm^{-1} disappeared, confirming the instability of Ru(5-Fbpb)(CO)(H_2O) in such solutions. For Ru(6-Fbpb)(CO)(H_2O), there were three main absorption bands at 306 nm, 357 nm and 415 nm respectively observed from Figure 3.2 d. With illumination time increasing, all three absorption bands decreased gradually and a new broad absorption band at 490−600 nm grew and increased with an isosbestic point at 486 nm revealed that the cleanly photoreaction proceeds.

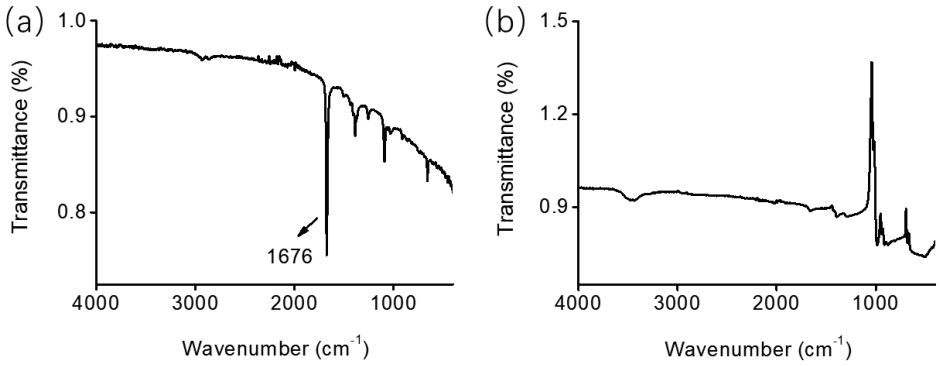

Figure 3.3 IR spectra of Ru(5-Fbpb)(CO)(H_2O) in solvent environment (a) ACN and (b) DMSO.

The UV-Vis experiments were also measured in phosphate buffer (80:20, PB:DMSO, v/v), under dark conditions. The ruthenium carbonyls Ru(bpb)(CO)(H_2O), Ru(3-Fbpb)(CO)(H_2O) and Ru(6-Fbpb)(CO)(H_2O) were stable and no changes in absorbance were observed in the phosphate buffer under dark conditions for longer than 12 h. This proves the exceptional stability of these three compounds in solution on the part of oxidation and decomposition. While decomposition of Ru(5-Fbpb)(CO)(H_2O) under dark conditions were also detected, further supporting the instability of substance in solution media which was independent of light.

3.2.3. Myoglobin assay for ruthenium carbonyl complexes and investigation of the CO-release mechanism

To determinate CO release from ruthenium CORMs, series of myoglobin (Mb) assays were performed. A fresh solution of ruthenium carbonyls respectively in oxygen-free DMSO was added to a buffered solution of myoglobin to get a 20 μM corresponding compound mixture. Then sodium dithionite was added. Upon illumination of this mixture with light (365 nm and 405 nm, 10 mW/cm^2), no obviously spectral changes were observed for Ru(bpb)(CO)(H_2O), Ru(3-Fbpb)(CO)(H_2O) and Ru(5-Fbpb)(CO)(H_2O), indicating no CO release from these carbonyl complexes. The typical overlaid spectra for 405 nm irradiation of Ru(6-Fbpb)(CO)(H_2O) was depicted in Figure 3.3 a. The absorbance of deoxymyoglobin (deoxy-Mb) at 557 nm decreased and the characteristic absorbance bands of carboxymyoglobin (Mb-CO) at 540 and 578 nm in the Q-band region grew and stabilized, thereby confirming the binding of CO to myoglobin. The

amount of CO per CORM was calculated from these data and amounted to the near-complete release of one equivalent CO for each molecule Ru(6-Fbpb)(CO)(H_2O) (Figure 3.3 b) and $t_{1/2} = 46$ min.

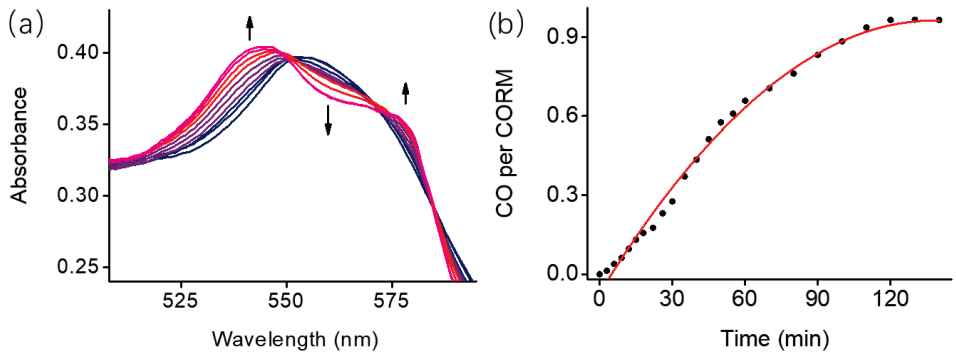

Figure 3.3 (a) Absorbance spectra of 20 µM Ru(6-Fbpb)(CO)(H_2O) in a heterogeneous 35 µM myoglobin solution under a nitrogen atmosphere irradiated for 140 min at 405 nm. (b) CO release per CORM of Ru(6-Fbpb)(CO)(H_2O) *versus* time.

In addition, a further myoglobin assay solution was undertaken in the dark for 140 min, to investigate the influence of sodium dithionite on CO-release from Ru(6-Fbpb)(CO)(H_2O). The characteristic absorbance band did not decrease demonstrably and there were no absorbance changes at 540 and 577 nm were observed. This confirms the stability of Ru(6-Fbpb)(CO)(H_2O) in the myoglobin solution under dark conditions and the stability against sodium dithionite. Hence, the release of CO was actually triggered by light illumination and not by the sodium dithionite.

Furthermore, considering the instability of Ru(5-Fbpb)(CO)(H_2O) in solution, the capability of light-induced CO release from solid state was investigated. A cuvette loaded 2 mg complex was determined with a portable CO sensor (Dräger Pac7000) under illumination with a 405 nm LED arrays (10 mW/cm^2) over a period of 20 hours. As a result, no CO release was detected from the unchanged spectra during measurement time. These data negate the possible function of Ru(5-Fbpb)(CO)(H_2O) as a CO releasing molecule. In addition, no CO signals were observed for the rest ruthenium carbonyl complexes.

TD-DFT calculations were performed to examine the electronic nature and CO release abilities of ruthenium carbonyl complexes. Calculations were obtained at the BP86/def2-TZVP level of

theory. [141,217,218] All investigated complexes exhibit similar frontier orbitals. The metal ions are Ru(II) in the low-spin state with a closed-shell electron configuration ground state for the ruthenium carbonyls. The HOMO-1 and HOMO are π_L-orbitals located on the carboxamide moiety of the co-ligands. The former HOMO-1 orbitals are consisted of d_π orbitals of the metal and are non-bonding towards CO. While HOMO orbitals bound with respect to CO ligand with a constitution of amide and phenylene orbitals and lie energetically about 2.1 eV below the HOMO in all complexes. They are responsible for the π-back donation interaction between the ruthenium and the carbon monoxide. Furthermore, the LUMO and LUMO+1 orbitals corresponding to antibonding d_π^*-orbitals are mainly contributed by $d_{\pi^*\text{pyridine}}$ -orbitals, $d_{\pi\text{-Ru}}$ orbitals and CO character. Similar to Ru(6-Fbpb)(NO)Cl described in chapter 2, ruthenium carbonyl substituted with fluorine at ortho position holds a longer Ru-CO bond length compared to the other ruthenium complexes, facilitating the release of CO from the metal. Upon illumination, the photoreaction of Ru(6-Fbpb)(CO)(H_2O) originates from the admixture of $d_\pi \rightarrow \pi^*_{\text{ligand}}$ MLCT character, subsequently $\pi_{\text{Ru-CO}}$ bond is weakened to release the CO from the metal remaining corresponding solvent molecule for originally bounded carbonyl.

In brief, these results confirm that the Ru(6-Fbpb)(CO)(H_2O) can be triggered by UV and visible light with low intensity to release one equivalent coordinated CO. The photochemical reaction of this ruthenium carbonyl starts from the admixture of d_π orbitals that consisted of d orbitals of ruthenium center and antibonding π orbitals of carbonyls.

3.2.4. Quantitative ^{19}F NMR analysis for Ru(6-Fbpb)(CO)(H_2O) upon irradiation

Time-dependent ^{19}F NMR spectroscopy was used to monitor the photodegradation of Ru(6-Fbpb)(CO)(H_2O). 4 mg photo-CORM was dissolved in 6 mL nitrogen-bubbled DMF and DMSO solution respectively. There is one initial signal peak at −60.97 ppm of the compound in DMF solution (Figure 3.4 b). Upon illumination, quite slightly chemical shifts toward high-field were observed, indicating that the chemical environment of CORM residue has changed. Moreover, ^{19}F NMR spectra demonstrated that a new peak at −61.10 ppm grew after 30 min irradiation and increased gradually. Interestingly, no obvious change was found in DMSO solution that is shown in Figure 3.4 a, which is explained by solvent effects.

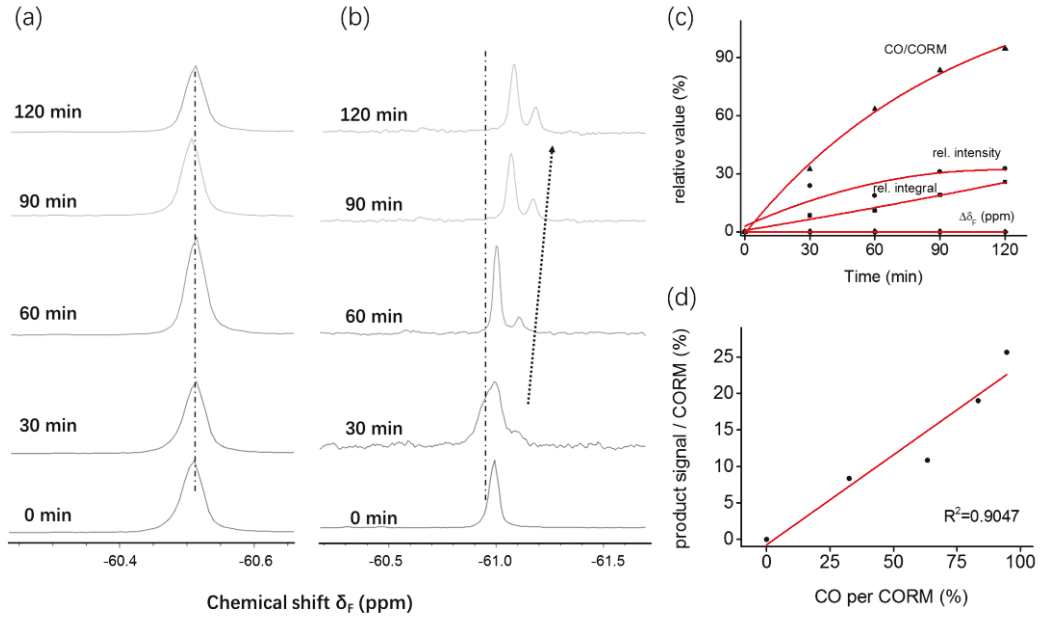

Figure 3.4 Comparison of ^{19}F NMR spectra of Ru(6-Fbpb)(CO)(H_2O) in (a) DMSO and in (b) DMF upon exposure to light at 405 nm using DMSO-d_6 as the deuterated solvent. (c) Plot of relative value *versus* irradiation time (triangle), released CO per CORM (diamond), ^{19}F NMR signals relative intensity (squire), ^{19}F NMR signals relative integral (circle) and relative chemical shifts $\Delta\delta_F$ (ppm). (d) Plot of ^{19}F NMR signals relative integral *versus* released CO per CORM from myoglobin assay.

All information of Ru(6-Fbpb)(CO)(H_2O) from all spectra were collected to quantitatively analysis the photoreaction, including chemical shifts, signal intensities and peak integrals. The data are listed in Table 3.2 of next subchapter. Relative changes were given to represent CO liberation process and were compared with data from myoglobin assay. Figure 3.4 c showed relative integrals and relative intensities exhibit similar tendency with irradiation time increasing. To establish an intuitive single variable system for this mono-carbonyl molecule, less variance relative integrals were extracted for further evaluation. Thus, the amount of photo-product represented by integrals was compared with the amount of released CO recorded from myoglobin assay. As a result, a linearity curve with a correlation coefficient $R^2 = 0.9047$ was depicted in Figure 3.4 d. This makes it reliable for ^{19}F NMR spectroscopy to quantitatively analysis CO release from CORM Ru(6-Fbpb)(CO)(H_2O).

3.3. Summary and conclusion

In summary, a collection of ruthenium-based CO releasing molecules with fluorinated carboxamide ligands are synthesized. Substitution with fluorine influence the photoactivity of carbonyl complexes. Among them, Ru(6-bpb)(CO)(H_2O) are highly stable under aerobic conditions as well as in solution environment. It releases CO upon illumination with low intensity light at 405 nm. DFT calculations confirm the photolysis of CO of Ru(6-bpb)(CO)(H_2O) starts from the admixture of d orbitals of metal center and antibonding π orbitals of ligands. Furthermore, quantitative ^{19}F NMR is well established to discrimination the photochemical reaction. In this work, a new peak grew and increased gradually in the time-dependent ^{19}F NMR spectra. The amount of photo-product represented by integrals of peaks was basically same with the amount of released CO recorded from myoglobin assay, which confirmed the feasibility of ^{19}F NMR spectroscopy to quantitatively analysis CO release from mono-carbonyl CORM. This strategy opens a new direction for detecting photo-CORMs containing fluorine.

3.4. Experimental section

3.4.1. General procedure

Materials and instrumentation.

1,2-diaminobenzene, triphenyl phosphite, triruthenium dodecacarbonyl ($Ru_3(CO)_{12}$) and fluoropyridine-carboxylic acid were purchased from commercial sources. All solvents were purified and dried by standard techniques prior to use during syntheses to avoid exposure to dioxygen and moisture. ^{1}H NMR, ^{13}C NMR and ^{19}F NMR spectra were recorded AV 400 MHz Bruker NMR spectrometer at room temperature using $CDCl_3$ and DMSO-d_6 as the solvents. Tetramethylsilane (TMS) as an internal standard for ^{1}H NMR, whereas trichlorofluoromethane (CCl_3F) as an internal standard for ^{19}F NMR. All IR (ATR) spectra were recorded on a Bruker Vertex 70 FT-IR spectrometer. UV-Vis spectra were recorded on an Analytik Jena Specord S 600 UV-Vis spectrometer and absorption spectra were recorded on a Cary 50 Varian spectrophotometer. Mass spectra were obtained from a Finnigan MAT SSQ 710 or MAZ95XL device. Elemental analysis was performed on a Vario EL III CHNS instrument. Fluorescence spectra were recorded on a Perkin Elmer LS50B luminescence spectrometer.

General experimental methods for UV-Vis study and myoglobin assay.

0.1 mM stock solution of CORMs in DMSO/H_2O (2:8) was used for all the studies. Photocycles with UV-A excitation light (λ = 366 nm) were performed on a Cary 5000 UV-Vis/NIR spectrometer, which equipped with a 250 W mercury lamp (10 mW/cm^2). The cuvette was held at a fixed distance of 20 cm from the grid in the illumination apparatus. Absorption spectra were taken after each irradiation for a certain period of time at different wavelengths.

Solution of ruthenium carbonyls (100 μM) in a quartz cuvette was exposed to UV light at 365 nm and 405 nm at every 10 min intervals to investigate the absorption spectrum.

The light-induced CO release under illumination with a 405 nm LED arrays (10 mW/cm^2) was also detected by a PAC7000 electrochemical CO Sensor (Drägerwerk AG & Co. KGaA, Lübeck, Germany) within an enclosed setup.

CO release study.

A solution of the corresponding complex in DMSO: PBS (20:80, v/v, volume V = 3.0 mL) was transferred to a stirred quartz cuvette (1 cm pathlength) at 20 °C in a UV-Vis absorption spectrometry setup. The volume of CORM solution and volume of myoglobin solution should be equal.

$$C_{CO\text{-}Mb} = (A_t^{540} - A_0^{540}) / [d \times (\varepsilon^{540} - \varepsilon_0^{540})] \quad \text{(Equation 3.1)}$$

where A_t^{540} is the absorbance at 540 nm at each timepoint *t,* A_0^{540} is the initial absorbance at 540 nm, d is pathlength of the cuvette (d = 1 cm) and ε^{540} (15.40 mM^{-1} cm^{-1}) is the extinction coefficient at 540 nm according to literature. [216] ε_0 is corrected initial extinction coefficient in phosphate buffer and is obtained from the following equation:

$$\varepsilon_0^{540} = (A_0^{540}) / [d \times (C_0^{\text{deoxy-Mb}}/2)] \quad \text{(Equation 3.2)}$$

where $C_0^{\text{deoxy-Mb}}$ is calculated with starting absorbance at 560 nm $A_{\text{deoxy-Mb}}^{560}$ and extinction coefficient ε^{560} (13.80 mM^{-1} cm^{-1}) at 560 nm.

^{19}F NMR analysis for Ru(6-Fbpb)(CO)(H_2O) upon irradiation.

^{19}F NMR spectra of Ru(6-Fbpb)(CO)(H_2O) were recorded AV 400 MHz Bruker NMR spectrometer at room temperature using DMSO-d_6 as the solvents with trichlorofluoromethane (CCl_3F) as an internal standard.

Table 3.2 Characteristic peak data of Ru(6-Fbpb)(CO)(H_2O) in nitrogen-bubbled DMF solution upon irradiation with light at 405 nm (10 mW/cm^2) compared to the amount of liberated CO recorded from myoglobin assay.

Time (min)	ν(F1) (ppm)	Intensity (abs)	ν(F2) (ppm)	Intensity (abs)	CO per CORM (%)
0	−60.9967	86469.0	0	0	0
30	−60.9967	76304247.5	−61.0971	18192105	0.3255
60	−61.0064	206981035.5	−61.1103	38615999	0.6339

90	−61.0307	164325113	−61.1506	51095711	0.8335
120	−61.0738	159379225	−61.1757	52046541	0.9463

Chemical shifts and relative intensity of signal peak are calculated and shown in the following table.

Table 3.3 Relative intensity and chemical shifts of Ru(6-Fbpb)(CO)(H_2O) in nitrogen-bubbled DMF solution upon irradiation with light at 405 nm (10 mW/cm^2) compared to the relative amount of liberated CO recorded from myoglobin assay.

Time (min)	**rel.int (%)**	**$\Delta\delta_{F1}$ (ppm)**	**$\Delta\delta_{F2}$ (ppm)**	**$\Delta\delta_{(F2-F1)}$ (ppm)**	**Relative Integral**
0	0	0	0	0	0
30	23.8415	0	0	0.1004	0.0912
60	18.6568	−0.0097	−0.0132	0.1039	0.8915
90	31.0943	−0.034	−0.0535	0.1199	0.8099
120	32.6558	−0.0771	−0.0786	0.1019	0.7437

3.4.2. Synthesis and measurements

Synthesis of N, N'-(1,2-phenylene)bis(X-fluoropicolinamide), ligands.

The ligands were prepared according to the modified method by Vagg et. al. [202] The synthesis details and characterization analysis have been described in Chapter 2.

Synthesis of Ru(X-Fbpb)(CO)(H_2O).

Ru(X-Fbpb)(CO) (H_2O) was synthesized according to an adapted procedure $Ru_3(CO)_{12}$ (0.088g, 0.14 mM) was added to a deoxygenated DMF solution of ligand (0.1452 g, 0.41 mM). The color of the solution turned red or brown immediately. The reaction was refluxed under nitrogen atmosphere for 20 h. Then the mixture was stand and cooled to room temperature. Filtering and washing with H_2O and Et_2O, a bright orange-blown solid would be collected.

Ru(Fbpb)(CO)(H_2O)

^{1}H NMR (400 MHz, DMSO-d_6), δ (ppm): 9.02 (1H, d, J = 4.76 Hz, ArH); 8.57 (2H, d, J = 6.06 Hz, ArH); 8.16 (1H, dt, J = 7.72 Hz, ArH); 8.15 (1H, d, J = 1.40 Hz, ArH); 7.69− 7.60 (H, m, ArH), 6.92 (1H, dd, J = 6.09 Hz, ArH). ^{13}C NMR (125 MHz, DMSO-d_6): δ (ppm) 165, 161, 154, 149, 140, 128, 125, 123, 122. IR(ATR): ν =1911 cm^{-1} (ν_{CO}, s). ESI-MS (m/z) $C_{19}H_{14}N_4O_4Ru$, calculated for: 464, observed: 445 [Ru(bpb)(CO)(H_2O)-H_2O]. Elemental analysis $C_{19}H_{14}N_4O_4Ru$, calculated: C = 49.24%, H = 3.05%, Ru = 21.81%, N = 12.09 %, O = 13.81%, found: C = 48.95%, H = 3.39%, N = 12.81%.

Ru(3-Fbpb)(CO)(H_2O)

^{1}H NMR (400 MHz, DMSO-d_6), δ (ppm): 8.95 (1H, d, J = 8.0 Hz, ArH); 8.57 (2H, d, J = 5.6 Hz, ArH); 8.26 (1H, t, J = 8.8 Hz, ArH); 8.15 (1H, d, J = 7.6 Hz, ArH); 7.43− 7.21 (3H, m, ArH). ^{13}C NMR (125 MHz, DMSO-d_6): δ (ppm) 164, 157, 145, 144, 128, 126, 123, 122. ^{19}F NMR (400 MHz, DMSO-d_6,) δ (ppm): −148. IR(ATR): ν =1917 cm^{-1} (ν_{CO}, s) ESI-MS (m/z) $C_{19}H_{12}F_2N_4O_4Ru$, calculated for: 500, observed: 454 [Ru(3-Fbpb)(CO)(H_2O)- CO-H_2O]. Elemental analysis $C_{19}H_{12}F_2N_4O_4Ru$, calculated: C = 45.70%, H = 2.42%, F = 7.61%, Ru = 20.24%, N = 11.22%, O = 12.81%, found: C = 44.99%, H = 2.39%, N = 11.50%.

Ru(5-Fbpb)(CO)(H_2O)

^{1}H NMR (400 MHz, DMSO-d_6), δ (ppm): 9.28 (1H, J = 8.0 Hz, ArH); 8.54 (2H, J = 5.6 Hz, ArH); 8.09 (1H, , J = 8.8 Hz, ArH); 8.02 (1H, s, J = 7.6 Hz, ArH); 6.91 (3H, , ArH). ^{13}C NMR (125 MHz, DMSO-d_6): δ (ppm) 202, 164, 163, 158, 145, 143, 142, 127, 123, 122. ^{19}F NMR (400 MHz, DMSO-d_6,) δ (ppm): −121.92. IR(ATR): ν =1931 cm^{-1} (ν_{CO}, s). ESI-MS (m/z) $C_{19}H_{12}F_2N_4O_4Ru$, calculated for: 500, observed: 454 [Ru(5-Fbpb)(CO)(H_2O)- CO-H_2O].

Elemental analysis $C_{19}H_{12}F_2N_4O_4Ru$, calculated: C = 45.70%, H = 2.42%, F = 7.61%, Ru = 20.24%, N = 11.22%, O = 12.81%, found: C = 45.31%, H = 2.39%, N = 11.35%.

Ru(6-Fbpb)(CO)(H_2O)

^{1}H NMR (400 MHz, DMSO-d_6), δ (ppm): 8.65 (1H, dt, J = 8.0 Hz, ArH); 8.32 (2H, m, J = 5.6 Hz,

ArH); 7.95 (1H, d, J = 8.8 Hz, ArH); 7.64 (1H, m, J = 7.6 Hz, ArH); 6.92 (3H, dt, ArH). ^{13}C NMR (125 MHz, DMSO-d_6): δ (ppm) 164, 158, 147, 141, 127, 126, 121, 120. ^{19}F NMR (400 MHz, DMSO-d_6,) δ (ppm): −60.33. IR(ATR): ν =1923 cm^{-1} (ν_{CO}, s). ESI-MS (m/z) $C_{19}H_{12}F_2N_4O_4Ru$, calculated for: 500, observed: 454 [Ru(6-Fbpb)(CO)(H_2O)- CO-H_2O]. Elemental analysis $C_{19}H_{12}F_2N_4O_4Ru$, calculated: C = 45.70%, H = 2.42%, F = 7.61%, Ru = 20.24%, N = 11.22%, O = 12.81%, found: C = 46.07%, H = 2.39%, N = 11.12%.

4. Fluorinated manganese CO releasing molecule

The following section focuses on a manganese tricarbonyl photo-CORM with a fluorobenzenesulfonyl functional group. This CORM-FBS demonstrated a strong stability in aqueous buffer media under dark conditions. Upon irradiation with low intensity light, CORM-FBS complex rapidly release almost all three CO, which were detected by myoglobin assay and time-dependent liquid IR spectra. Additionally, the photolysis of carbon monoxide occurred in a stepwise way forming mono- or dicarbonyl species with additional solvent molecules as ligands for further photoreaction. In this study, ^{19}F NMR spectroscopy was employed to detect photo-product iCORM-FBS and was confirmed applicable for quantitative evaluation CO release. This provides a reliable method of monitoring the photochemical activities from fluorine containing CO releasing molecules.

4.1. Introduction

4.1.1. Quantitative ^{19}F NMR spectroscopy

Nuclear magnetic resonance (NMR) spectroscopy has been performed to determinate of the substances content and products characterization because of its high speed, sensitivity and precision. [219] Compared to traditional ^{1}H and ^{13}C NMR, ^{19}F NMR has a broader chemical shift range (approximately 400 ppm for organics) and high resolution to avoid signal overlap with each other, leading to ^{19}F NMR is more suitable for the quantitative analysis of compound in a biological background. Therefore, this technology has been applied to the identification of molecule structures, quantitative studies of pharmaceutical agent and drug metabolism as well as monitoring of the reaction process. For example, Komber et al. used ^{19}F NMR to characterize generated main perfluorooctanesulfonate isomers from a commercial mixture via quantification of the individual -CF_3 branched isomers. [220] This group also reported kinetic studies on the stepped reaction of decafluorobiphenyl with thiophenol by employing this spectroscopy to determine rate constants. [221] Furthermore, Althelm and colleagues prepared a collection of fluorinated boronic

acid-appended salts to identify and discriminate diol containing bioanalytes under physiological conditions. [222,223] Characteristic ^{19}F NMR signals were processed into 2D quick response-like barcodes to present directly visual images and compare the interaction of receptors with analytes. So far, growing studies on the research methodology of ^{19}F NMR for the quantitative analysis of fluorinated complexes have been reported and this spectroscopy is expected to widen the application scope with improving high-magnetic field NMR instrument and high-sensitivity probe.

4.1.2. Manganese tricarbonyl CORMs

As mentioned previously in chapter 1.2.2, the carbon-metal-oxygen bond is influenced by the π back-donation process which results from antibonding π* molecular orbital on the CO and the d-orbitals of metal center. Among variety of metal carbonyl complexes, ruthenium-, iron-, rhenium-, and manganese-carbonyl CORMs were well studied. Ruthenium complexes are generally stable and require UV light to liberate CO with low quantum yield. While manganese complexes are much more attractive due to their 3d metal orbitals leading to a fast CO release and the Mn center commonly bonds with poly-carbonyl ligands. Moreover, Lehnert et al. insisted that ruthenium complexes were generally directly excited from a bonding d_π-π* orbital to an antibonding π*-d_π orbital (the single excited state). [87] The manganese complexes can undergo photolabilization by the direct single excited state and an indirect way which needed a higher singlet excited state of electron excitation corresponding to the triplet state (d_{xy}→ π*-d_π).

In general, a series of Lewis bases including arenes, amines and other heterocyclic moieties facile coordinate to manganese carbonyls to form a variety of six coordinated fac-Mn(I) tricarbonyl complexes. These photo-CORMs release CO when irradiated with UV to visible light. However, studies mainly focus on the spatially and temporally precisely controlled CO release and biological activity profiles in vivo, few refers the primary photophysical and photochemical steps. Although majority of CORMs can release almost all three coordinated carbonyl ligands, it remains difficult to confirm reaction occurs in a stepwise or concerted way for a long time.

To investigate the light-triggered carbon monoxide release, Kurz et al. used two manganese (I) complexes $Mn(CO)_3(tpm)(PF_6)$ (tpm = *tris*(pyrazolyl)methane) and $Mn(CO)_3(bpzaa)$ (bpzaa = *bis*(pyrazolyl)acetic acid) as representative compounds with spectroscopic methods. [224]

They found that the manganese centers lose their carbonyl ligands in a stepwise manner and the dicarbonyl intermediates formed after one CO release per CORM. The remaining two carbonyl ligands were then liberated by oxidation to manganese (II) ultimately resulting in final reaction products μ-O-Mn(III) compound. This is also associated to the difference of measured CO release amount via IR spectroscopy and myoglobin assay.

4.2. Results and Discussion

The following section describes the preliminary synthesis and general characterization of the light-responsive carbon monoxide releasing molecule with a fluorobenzenesulfonyl group (CORM-FBS). This CORM-FBS molecule was stable under dark conditions and in oxygen-free aqueous buffer media. Its photoreaction was spectroscopically examined and the photo mechanism was given. The TD-DFT calculations were performed to evaluate the electronic nature of CORM-FBS and CO release abilities.

4.2.1. Synthesis and Characterization of CORM-FBS

4-fluoro-N, N-bis(pyridin-2-ylmethyl)benzenesulfonamide (ligand) was obtained from the reaction of Di-(2-picolyl) amine and 4-fluorobenzenesulfonyl chloride in the presence of triethylamine (NEt_3) at room temperature with a yield of 52 % (Scheme 4.1).

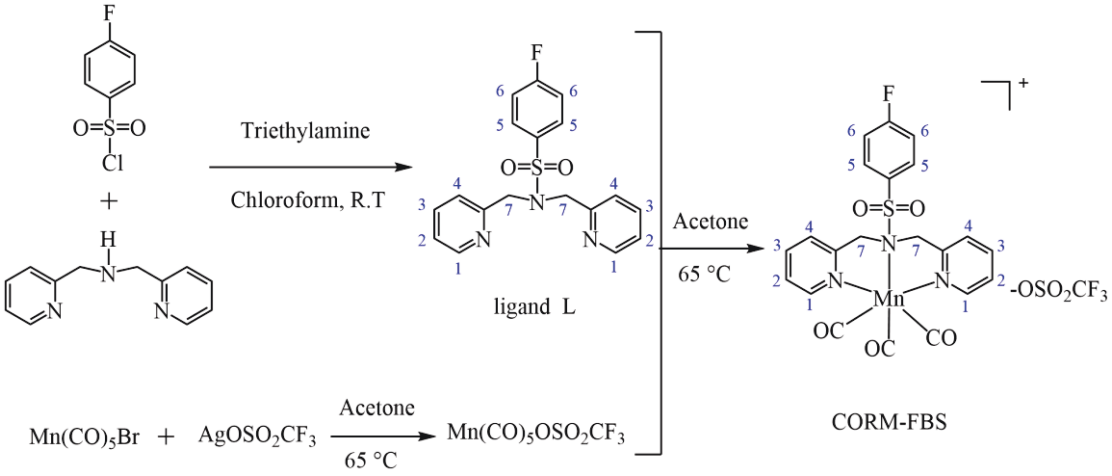

Scheme 4.1 Synthesis of ligand L and CORM-FBS.

Isolated compound ligand L was further allowed to react with $Mn(CO)_5Br$ followed by silver triflate to obtain the desired complex CORM-FBS. Analytical and spectroscopic data confirmed the successful synthesis and purity of ligand and CORM-FBS. The solid-state X-ray crystal structure of CORM-FBS shows that the three carbonyl ligands occupying one face are facially coordinated to the Mn(I) center and opposite to the facially coordinated dipicolyl amine moiety

(Figure 4.2 b). The complex demonstrated a pseudo octahedral structure. The angles of the S-N-Mn were found to be 110.65 º, illustrating that the hybridization of the sulfonamide nitrogen has changed from sp^2 to sp^3 upon binding to manganese center, which was in accordance with related tricarbonyl complexes. [218] The Mn–N (sp^3) bond length (2.158 (13) Å) was found to be unusually longer than the other Mn–N (sp^2) bond distances (generally ~2.050 (14) Å to 2.067 (14) Å) and confirms the superior coordinating ability of the sp^2 hybridized pyridine nitrogens compared to the sp^3 hybridized amine, which mainly owing to the steric effects of fluorobenzenesulfonyl group. [225,226] In addition, the Mn-N (sp^3) bond length (2.158 (13) Å) was much longer than the distance of S-N bond (1.732 (13) Å), showing the strong bond introduced by the tripodal nature of the ligand.

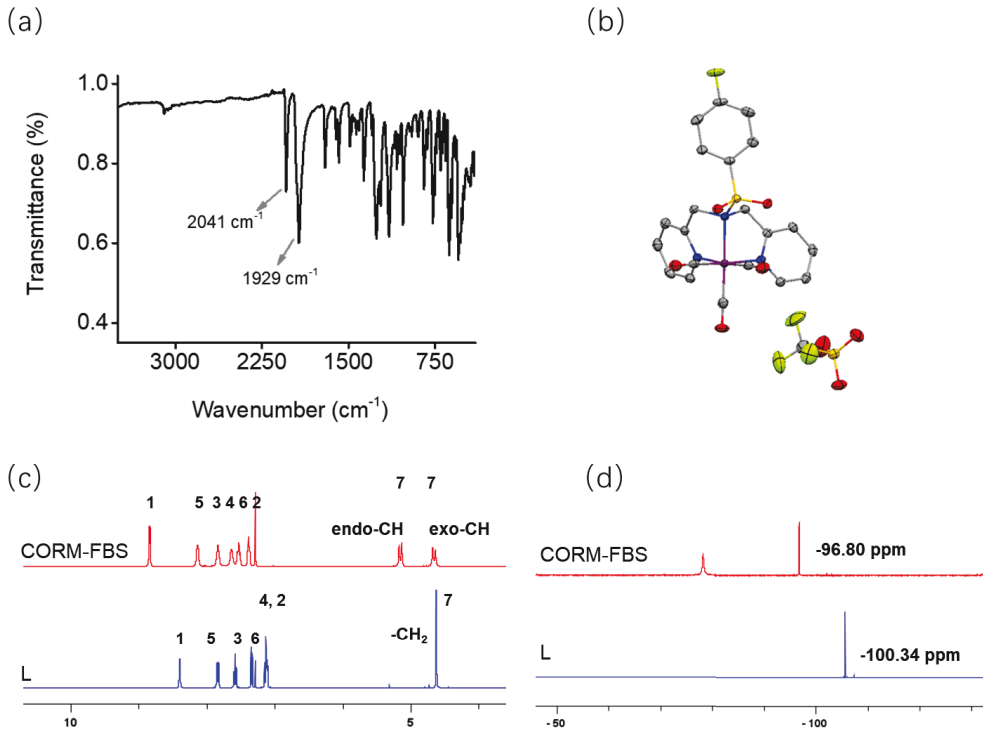

Figure 4.2 (a) IR spectrum of CORM-FBS. (b) X-ray crystal structure of CORM-FBS. Solvent molecules, triflate anion and hydrogens in crystal structure are omitted for clarity; gray = carbon, blue = nitrogen, red = oxygen, purple = manganese, green=fluoride and yellow = sulphur. (c) ^{1}H NMR spectra of ligand L and CORM-FBS in $CDCl_3$. (d) ^{19}F NMR spectra of ligand L and CORM-FBS in $CDCl_3$.

The IR spectrum of CORM-FBS represents two ν_{CO} bands (2041 and 1929 cm^{-1}) instead of three due to the high symmetry (no splitting at 1929 cm^{-1}). Furthermore, comparison of ^{1}H NMR

spectra of ligand and CORM-FBS shows that the methylene protons of the dipicolyl amine moiety have singlet multiplicity for L (δ = 4.62 ppm) and turn two doublets for CORM-FBS (δ = 5.17−5.13 and 4.68−4.64 ppm), which is explained by the fact that one pair projects towards and the other pair projects away from the carbonyl ligands. The two nonequivalent magnetically methylene group are considered as endo- and exo-CH protons (Figure 4.2 c). In addition, chemical shifts of the phenylene protons and pyridine protons after reaction further indicates the coordination of the metal ion. All protons demonstrate chemical shift to lower field and the H4 protons at 7.65 ppm meta to the pyridyl nitrogen show the most downfield significant shift ($\Delta\delta$ = 0.55 ppm). In ^{19}F NMR spectra (Figure 4.2 d), phenylene fluorine signal peak shifts to -96.80 ppm from −100.34 ppm of ligand and the peak around −78.17 ppm, corresponding to triflate functional group (-OSO_2CF_3) of CORM-FBS.

4.2.2. UV-Vis evaluation of ligand and CORM-FBS under illumination

To evaluate CO release abilities, absorption spectra of CORM-FBS upon irradiation at 405 nm were performed until no further spectral changes were observed. The electronic absorption spectra were undertaken in nitrogen-bubbled aqueous phosphate buffer in 10 seconds intervals and were shown in Figure 4.3.

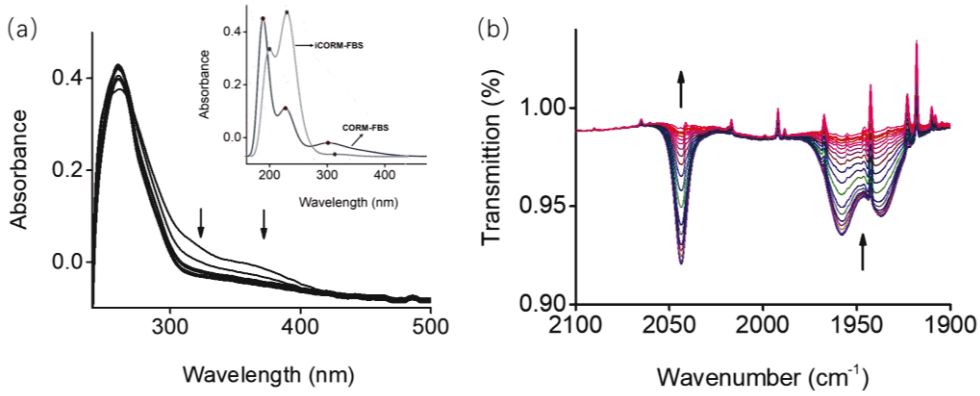

Figure 4.3 (a) Evolution of absorption spectra of CORM-FBS (20 μM) in phosphate buffer (DMSO:PB, 1:99, v/v, pH=7.4) during blue light irradiation (405 nm, 8 mW/cm^2) for 120 s. Time between spectra is 10 s. Inset: Theoretical absorbance spectra model of CORM-FBS and photoproduct iCORM-FBS without solvent. (b) Time evolution of liquid-phase IR spectra during irradiation of CORM-FBS solution (10 mM,

DMSO) recorded every 30 seconds over a course 18 min.

Two main absorption bands respectively at 260 nm and 360 nm were shown in Figure 4.3 (a). The former band is commonly assigned to polycyclic aromatic hydrocarbons. An indistinct shoulder absorption band at around 304 nm interlaced with the less intense absorption band at 360 nm was also observed. With illumination time increasing, the broad absorption region decreased gradually remaining an isosbestic point at 425 nm and the absorption band at 360 nm increased with a small range red-shift. This results from the metal to ligand charge transfer (MLCT) from d_{Mn} to π^*_{py}, corresponding to the excitation state S_5–S_8 at 350 nm predicted by TD-DFT calculations (ΔE = 0.30 eV, $\Delta\lambda_{max}$ = 27 nm). TD-DFT estimates the excitation S_1 at 400 nm with 3.10 eV, that corresponds to the same HOMO → LUMO transition. Moreover, DFT calculations predicts that CORM-FBS conformer contains three absorption bands respectively at 188 nm (ε = 3.7 × 10^4 mol^{-1} L cm^{-1}), 228 nm (ε = 1.3 × 10^4 mol^{-1} L cm^{-1}) and 303 nm (ε = 3.6 × 10^3 mol^{-1} L cm^{-1}), while the iCORM-FBS exhibits absorption bands in the region at 202 nm (ε = 1.4 × 10^4 mol^{-1} L cm^{-1}), 232 nm (ε = 1.8 × 10^4 mol^{-1} L cm^{-1}) and 313 nm (ε = 3.0 × 10^2 mol^{-1} L cm^{-1}). These data are essentially in agreement with the spectral records.

The photoreaction was also measured under dark conditions. No changes in absorbance were observed in the phosphate buffer media over a course 12 h, confirming the stability of compound CORM-FBS in solution environment. Additionally, time-dependent liquid-phase IR spectra for CORM-FBS upon exposure to light at 405 nm was performed. It is clearly to observe the carbonyls characteristic vibration bands at 2043 cm^{-1}, 1957 cm^{-1} and 1936 cm^{-1} in pure DMSO solution decreased gradually with illumination time increasing, ultimately disappeared after 15 min. This confirms that all three equivalents coordinated CO release. No back reaction was observed even when the light was turned off.

4.2.3. Myoglobin assay for CORM-FBS and investigation of the CO-release mechanism

To determinate CO release from CORM-FBS, a myoglobin assay was performed at room temperature. A fresh solution of CORM-FBS in nitrogen-bubbled DMSO was added to a buffered

solution of myoglobin to obtain a mixture of 15 µM CORM-FBS and 60 µM myoglobin. Then excess sodium dithionite was added to deplete possible incoming oxygen. Upon illumination of this mixture with light (405 nm, 8 mW/cm^2), the absorbance of deoxy-Mb at 557 nm decreased and the characteristic absorbance bands of Mb–CO at 540 and 578 nm in the Q-band region grew and stabilized (Figure 4.4 a). These confirm the deliberation of CO and subsequently binding of CO to myoglobin. Moreover, a further myoglobin assay solution was kept in the dark for 60 min to investigate the influence of sodium dithionite on CO-release from CORM-FBS. The characteristic absorbance band did not reduce and no absorbance changes of Q-band region were observed. This indicates stability of CORM-FBS in the myoglobin solution under dark conditions and the stability against sodium dithionite. Hence, the release of CO was driven by light illumination and not by the sodium dithionite. Therefore, these data show that CORM-FSB releases CO upon irradiation at 405 nm. The concentration of liberated CO was calculated from these data and amounted to the near-complete release of three equivalents CO for each molecule CORM-FBS (Figure 4.4 b) with $t_{1/2}$ = 43 s.

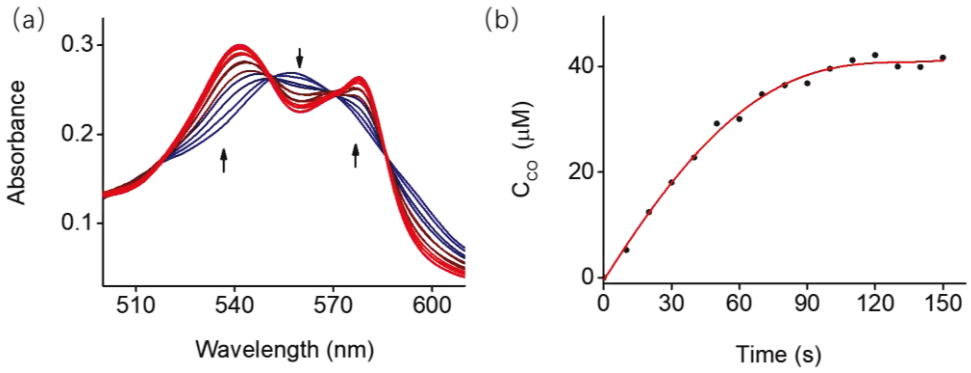

Figure 4.4 (a) Conversion of deoxy-Mb to Mb–CO in a mixture of CORM-FBS (15 µM) and deoxy-Mb (60 µM) in phosphate buffer (pH = 7.4) upon exposure to light (405 nm, 8 mW/cm^2). (b) Concentration of CO release from CORM-FBS *versus* time.

To further investigate the mechanism of CO release upon irradiation and identify molecular orbitals associated to this photodegradation, TD-DFT calculations were performed. Several excited states (S_5–S_7) were identified between 350 and 331 nm that correspond to excitations from the three Mn-CO bonding d_π-orbitals to antibonding linear combinations between π^*_{py} orbitals. This weakened the electron density at the Mn center thereby undermined the π-back

donation interaction between manganese and CO, resulting in the CO release completely. Low lying excited states (S_1–S_4, shown in Figure 4.5) were identified between 400 nm and 368 nm that are responsible for mixed MLCT and ligand field states (LF) with local $d_\pi \rightarrow d^*_\sigma$ orbitals. These transition states represented that the populated d^*_σ orbitals were directly antibonding towards the CO ligands leading to CO dissociation. These data indicate that the photochemical activity of CORM-FBS at 405 nm occurs from ligand field (LF) excitation states. Additionally, the fluorophenyl moiety was identified not involved in the photoreaction.

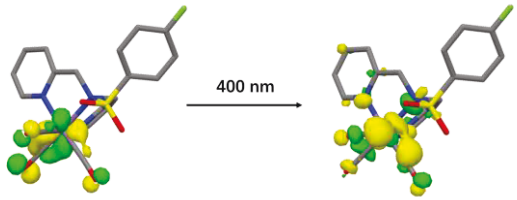

Figure 4.5 Illustrations of the MLCT state (S_1) at 400 nm as predicted by TD-DFT. Transfer of electron density from the metal center onto the ligand leads to CO release. Hydrogens were omitted for clarity.

This result confirms that the CORM-FBS can be introduced by low intensity light and that the photo-induced liberation of CO is not influenced by the fluorophenyl moiety. It is further established that the CORM-FBS is a stable CO releasing molecule and that CORM-FBS release all three carbonyl CO upon illumination with low intensity light.

4.2.4. Characterization of the inactive product after irradiation

Besides CO, Mn product also generates from the photo dissociation of CORM-FBS. To investigate the inactive photo-product that is usually considered as iCORM, diverse characterization approaches are performed.

^{1}H NMR spectroscopy of photo-product demonstrated that observed proton signals without chemical shift, indicating the ligand L still combined with the Mn center (Figure 4.6 a). While the broader signal peaks upon illumination compared to the initial CORM-FBS exhibited the paramagnetic nature of the product, which corresponds to the oxidation status of manganese.

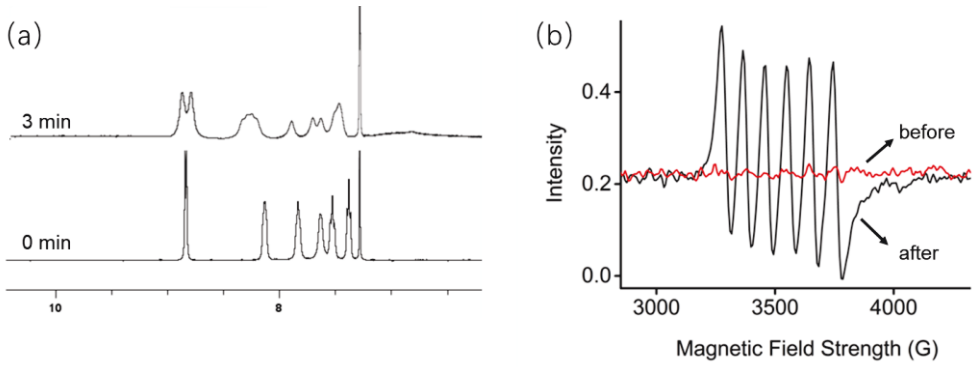

Figure 4.6 (a) Time-dependent partial ^{1}H NMR spectra of CORM-FBS before and after photolysis (405 nm, 8 mW/cm^2). (b) X-band ESR spectra (at 295 K) of CORM-FBS (4 mM) before and after photolysis in DMSO: water (1:1, v/v). Microwave frequency, 9.87 GHz; modulation amplitude, 0.6 Mt; modulation frequency, 100 kHz and power of the microwave source, 1.262 mW.

Meanwhile, the comparison of X-band ESR spectrum (at 295 K) further confirmed the change of oxidation status of manganese. The spectra of photolyzed solution of CORM-FBS represented a six-line spectrum indicative of a paramagnetic Mn(II) species (Mn^{II} -d_5) with a high spin state (Figure 4.6 b) in photo-product, which is contrary to the initial diamagnetic low-spin state of Mn^{I} -d_6 in CORM-FBS.

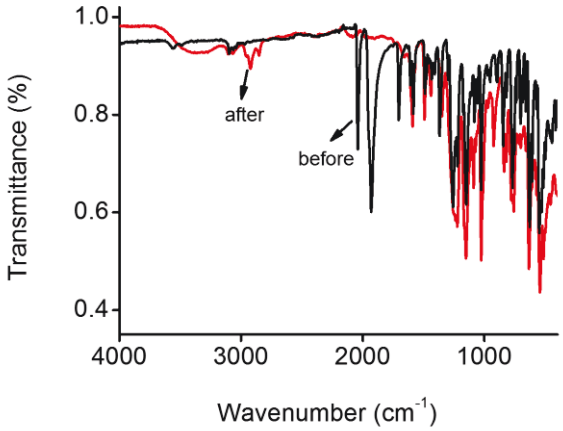

Figure 4.7 IR spectra of CORM-FBS before and after photolysis.

In addition, the ATR-IR spectra showed that the absence of the CO vibrational bands (1900–2100 cm^{-1}) after the irradiation at 405 nm. This is accordance with data from the myoglobin assay in aqueous solution and time-dependent liquid-phase IR spectra previously demonstrated. These results clearly confirm that all three CO ligands were released from CORM-FBS upon illumination. Consequently, the remaining positions where occupied by original carbonyls are

populated by ambient solvent molecules, which can be described as a conversion from $[MnL(CO)_3]^+$ to $[MnL(solvent)_3]^{2+}$.

4.2.5. Quantitative 19F NMR analysis for CORM-FBS upon irradiation

Time-dependent ^{19}F NMR spectroscopy was used to monitor the photodegradation of CORM-FBS. The first spectroscopy assay was performed at room temperature. The signal peaks became broader and disappeared with the illumination time increasing especially for the triflate functional group ($-OSO_2CF_3$) of CORM-FBS (shown in Table 4.2). This attributed to the paramagnetic nature of manganese(II) species. To reduce the signal linewidth, temperature series in the range of 40 °C to −70 °C in ACN solution were applied. Spectra of ^{19}F NMR at 40 ºC demonstrated that the signals completely disappeared at a faster rate than that at room temperature and detail information was lost (shown in Table 4.1). Low temperature was confirmed to decrease the influence of paramagnetism and spectra results upon illumination within 120 s were depicted in Figure 4.8.

There was one initial characteristic signal peak (F1) found at −101.02 ppm of CORM-FBS in ACN solution before irradiation. Upon exposure to light (405 nm, 8 mW/cm^2), slightly chemical shifts toward low-field were observed, indicating that the chemical environment of CORM residues has changed. Moreover, ^{19}F NMR spectra represented that a new peak (F2) at −102.28 ppm grew after 10 seconds irradiation and increased gradually as well as shifted to low-field. Then a third peak (F3) displayed at −107.60 ppm and increased with 30 seconds excitation. Moreover, signals of F1 and F2 disappeared after 90 seconds and 60 seconds illumination respectively, remaining only one characteristic peak F3 with an ultimately chemical shift $\Delta\delta_F$ = −6.39 ppm.

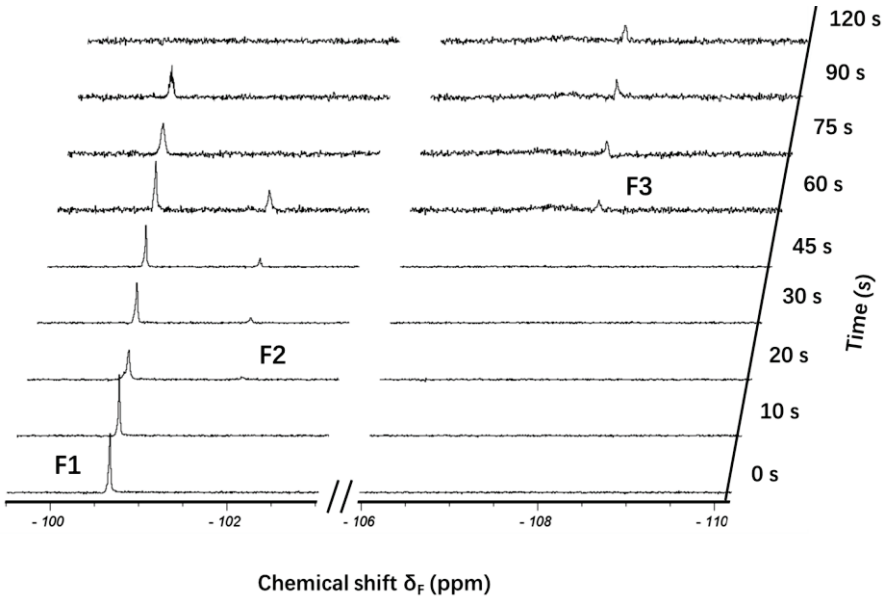

Figure 4.8 Comparison of ^{19}F NMR spectra of CORM-FBS in ACN upon exposure to light at 405 nm with different irradiation time (−70 °C, using CD_3CN-d_3 as deuterated solvent, 8mW/cm^2).

It is clearly illustrated that the process of photoreaction with the conversion from F1 to F3 from the comparison of ^{19}F NMR spectra before and after excitation. Moreover, the quantitative ^{19}F NMR spectra revealed the existence of intermediate through the generation and disappearance of F2, which is assigned to the tricarbonyl species with additional solvent molecules as ligands. [224,227]

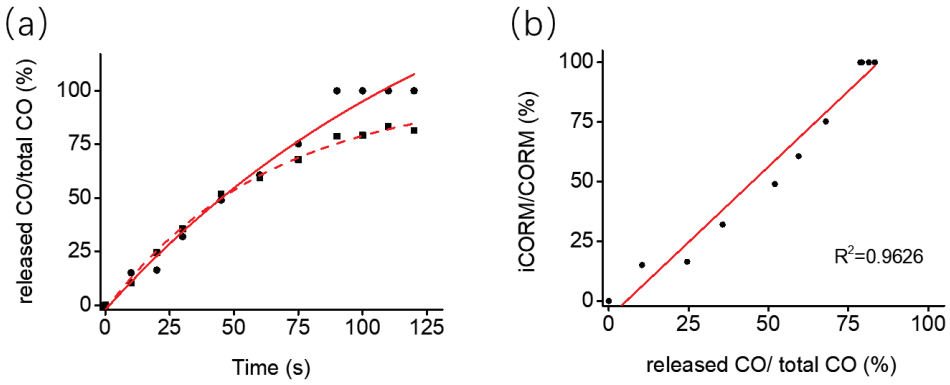

Figure 4.9 (a) Comparison of ^{19}F NMR signal relative intensity change and released CO from myoglobin assay against time. circle: plots from ^{19}F NMR, square: myoglobin assay data. (b) Content of photoproduct (iCORM) calculated with relative intensities *versus* content of released CO from myoglobin assay.

Information of CORM-FBS from all spectra was collected to quantitatively analysis the

photoreaction and the details are listed in Table 4.1 of next subchapter. Relative changes were given to represent CO liberation process and were compared with data from myoglobin assay. To establish an intuitive single variable system for CORM-FBS, less variance relative intensities were extracted for calculation of CORM residues. Figure 4.9 a showed the amount of product obtained from ^{19}F NMR and myoglobin experiments respectively under illumination, in which represented similar tendency. Furthermore, the amount of photo-product represented by relative intensity was compared with the amount of released CO recorded from myoglobin assay. As a result, a linearity curve with a correlation coefficient $R^2 = 0.9627$ was depicted in Figure 4.9 b.

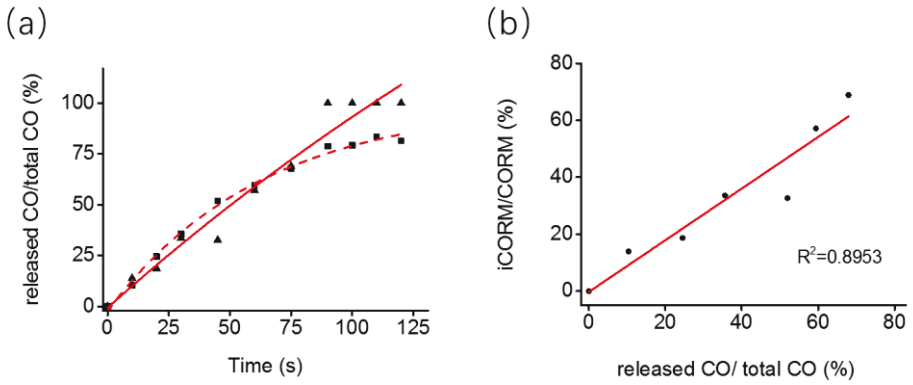

Figure 4.10 (a) Comparison of ^{19}F NMR signal relative integrals and released CO from myoglobin assay against time. circle: plots from ^{19}F NMR, square: myoglobin assay data. (b) Content of photoproduct (iCORM) calculated with relative integrals *versus* content of released CO from myoglobin assay.

In addition, very similar results were obtained by calculating with signal integrals (Figure 4.10), which further supported the feasibility of quantitative analysis from ^{19}F NMR spectra. Overall, ^{19}F NMR offered a reliable method to monitor the photoreaction process of CORM-FBS with good accuracy. Upon irradiation, one CO ligand was photochemically dissociated and replaced by the solvent molecule, remaining residues for further step through the oxidation reaction.

4.3. Summary and Conclusion

In brief, a stable and water-soluble manganese-based tricarbonyl complex with a fluorobenzenesulfonyl group was prepared. This CORM-FBS can rapidly release almost all three CO molecules upon illumination with low intensity light. DFT and TD-DFT calculations gave insight into the CO release mechanism and the properties of the inactive CORM product. For the first time, ^{19}F NMR is performed to quantitatively analysis the photoreaction process of CORM-FBS under irradiation. Despite the paramagnetic of Mn(II) species, the comparison of characteristic spectra reveals that one CO ligand was firstly photochemically dissociated and replaced by solvent molecule with remaining residues for further CO release. The high-speed, good accurate and ease of measurement technology make ^{19}F NMR spectroscopy provide a promising direction to monitor the process of CORM photo-degradation. We expect that with continuously improving quality of NMR spectrometers and mature technique, this approach for the detection and discrimination can be applicable to a wider scope.

4.4. Experimental section

4.4.1. General procedure

Materials and instrumentation.

$Mn(CO)_5Br$, silver triflate, di-(2-picolyl)amine, 4-fluorobenzenesulfonyl chloride and triethylamine were purchased from Sigma-Aldrich. Solvents were purified and/or dried by standard techniques prior to use for all syntheses. ^1H NMR and ^{13}C NMR were recorded on a Bruker AV 400 MHz NMR spectrometer in $CDCl_3$ or DMSO-d_6 at room temperature, ^{19}F NMR spectra were performed in ACN-d_3 at -70 °C and 40 °C. Tetramethylsilane (TMS) served as an internal standard for ^1H NMR, and trichlorofluoromethane (CCl_3F) as an internal standard for ^{19}F NMR. Chemical shifts as related to the signals of the deuterated solvents used. UV-Vis absorption spectra were recorded with a spectrometer Specord S 600 UV-Vis from Analytic Jena. Mass spectra (ESI-MS) were acquired on a Finnigan MAT SSQ 710 or MAZ95XL device. Elemental analysis was performed on a Heraeus Vario EL III CHNS instrument. All IR (ATR) spectra were recorded in a range of 400−4000cm^{-1} on a Bruker Vertex 70 FT-IR. Electron spin resonance (ESR) spectra on solution samples were recorded at X-band frequencies on a Bruker Elexsys E500 spectrometer.

General experimental methods for UV-Vis studies.

A 1 mM stock solution of CORM-FBS and FBS ligand were prepared in nitrogen-bubbled DMSO, which was used for all studies. For spectroscopic measurements, the DMSO stock solution was diluted with 10 mM phosphate buffer (PB, pH 7.4) to acquire a 15 μM solution in 1:99 v/v DMSO:PB, unless not otherwise mentioned. UV-Vis absorption spectra were recorded at room temperature in a quartz cuvette every 10 seconds during UV light exposure (UVP Benchtop 2 UV Transilluminator, ≤8 mW/ cm^2).

Photolysis Experiment.

Solution of CORM-FBS (15 μM) in a quartz cuvette was exposed to different light sources (365 nm and 405 nm; 8 mW/cm^2) at every 20 seconds intervals to investigate the photoinduced CO-

release studies. The power of the light sources was determined with a PM100USB power meter.

CO-release study.

The light-induced CO-release from CORM-FBS was achieved by illumination with LED light (405 nm) in myoglobin assay. The irradiation experiments were performed at fixed light intensities (8 mW/cm^2). The number of equivalents CO-release per CORM-FBS was determined by myoglobin assay by using the following equation.

The volume of CORM solution and volume of myoglobin solution should be equal.

$$C_{CO\text{-}Mb} = (A_t^{540} - A_0^{540}) / [d \times (\varepsilon^{540} - \varepsilon_0^{540})] \quad \text{(Equation 4.1)}$$

where A_t^{540} is the absorbance at 540 nm at each timepoint *t,* A_0^{540} is initial absorbance at 540 nm, d is pathlength of the cuvette (d = 1 cm) and ε^{540} (15.40 mM^{-1} cm^{-1}) is the extinction coefficient at 540 nm according to literature. [216] ε_0 is corrected initial extinction coefficient in phosphate buffer and is obtained from the following equation:

$$\varepsilon_0^{540} = (A_0^{540}) / [d \times (C_0^{\text{deoxy-Mb}}/2)] \quad \text{(Equation 4.2)}$$

where $C_0^{\text{deoxy-Mb}}$ is calculated with starting absorbance at 560 nm $A_{\text{deoxy-Mb}}^{560}$ and extinction coefficient ε^{560} (13.80 mM^{-1} cm^{-1}) at 560 nm. The calculated Mb-CO concentration was plotted against the illumination time. The calculated CO-Mb concentration divided by the CORM-FBS concentration to get the number of CO equivalents released per mole of CORM-FBS.

^{19}F NMR analysis for CORM-FBS upon irradiation.

^{19}F NMR spectra of CORM-FBS were recorded AV 400 MHz Bruker NMR spectrometer at room temperature, 40 °C and −70 °C respectively, using CD_3CN as the solvents with trichlorofluoromethane (CCl_3F) as an internal standard.

Table 4.1 Characteristic peak data of CORM-FBS in nitrogen-bubbled CD_3CN solution upon irradiation with light at 405 nm (8 mW/cm^2) performed at 40 °C. Signal disappeared after irradiated 45 s due to the paramagnetic Mn^{2+} states.

time (s)	ν(F1) (ppm)	Intensity (abs)	ν(F2) (ppm)	Intensity (abs)	rel.int F2/F1 (%)

0	−100.6226	741695.78	0	0	0
10	−100.6279	789885.01	−101.9464	88239.06	11.1711273
20	−100.6275	309358.94	−101.9558	49856.18	16.11596549
30	−100.6261	399194.96	−101.9531	100040.21	25.06048924
45	−100.619	188964.13	−101.9366	48476.63	25.65387939

Table 4.2 Characteristic peak data of CORM-FBS in nitrogen-bubbled CD_3CN solution upon irradiation with light at 405 nm (8 mW/cm^2) performed at room temperature.

time (s)	**ν(F1) (ppm)**	**Intensity (abs)**	**ν(F2) (ppm)**	**Intensity (abs)**	**ν(F3) (ppm)**	**Intensity (abs)**
0	−100.697	2956904.45	0	0	--	--
10	−100.7034	1477084.25	−101.9814	128780.2	--	--
20	−100.7	1998922.92	−101.9836	420688.28	--	--
30	−100.6996	2073539.98	−101.9836	420688.28	−107.6003	57718.45
45	−100.7094	655307.26	−101.9947	247305.3	−108.2003	127448.68
60	--	--	--	--	−108.0652	5158.42
75	--	--	--	--	−108.2018	222186.8
90	--	--	--	--	−108.1866	108394.8

Table 4.3 Characteristic peak data of CORM-FBS in nitrogen-bubbled CD_3CN solution upon irradiation with light at 405 nm (8 mW/cm^2) performed at −70 °C compared to the amount of liberated CO recorded from myoglobin assay.

Time (min)	ν(F1) [ppm]	Intensity [abs]	ν(F2) [ppm]	Intensity [abs]	ν(F3) [ppm]	Intensity [abs]
0	−101.0243	86468.95	0	0	--	--
10	−101.0166	45268.44	−102.2754	8051.7	--	--
20	−101.0185	39371.75	−102.2572	7737.81	--	--
30	−100.7636	763264.27	−102.0364	117282.34	−107.6003	57718.45
45	−100.764	378552.17	−102.0363	61555.86	−107.3821	64773.58

60	−100.7638	173039.42	--	--	−107.4524	51377.81
75	−100.7508	69248.38	--	--	−107.2014	40683.71
90	--	--	--	--	−107.3491	25390.98
120	--	--	--	--	−107.4126	42854.8

4.4.2. Synthesis and measurements

Synthesis of 4-fluoro-N, N-bis(pyridine-2-ylmethyl)benzenesulfonamide (ligand).

Di-(2-picolyl) amine (154 mg, 0.77 mmol) and 4-fluorobenzenesulfonyl chloride (150 mg, 0.77 mmol) were dissolved in 25 mL of dry chloroform ($CHCl_3$). To this solution, triethylamine (0.14 ml) was added and stirred for 5 h at room temperature. The crude mixture was concentrated and subjected to alumina column chromatographic (eluent ethyl acetate and n-hexane in 2:3 (v/v)) purification to result pure oil compound ligand (185 mg, 52%) after evaporation of the solvent.

^{1}H NMR (400 MHz, $CDCl_3$), δ (ppm): 8.39 (2H, d, J = 4.4 Hz, ArH); 7.84 (2H, J = 8.8 Hz, ArH); 7.56 (2H, t, J = 7.5 Hz, ArH); 7.34 (2H, d, J = 7.7 Hz, ArH); 7.14 (2H, d, J = 7.8 Hz, ArH); 7.12 (1H, d, J = 8.6 Hz, ArH); 7.11 (1H, t, J = 3.2 Hz, ArH); 4.62 (4H, s, CH_2). ^{13}C NMR (100 MHz, $CDCl_3$): δ (ppm) 166.23, 163.70, 156.09, 149.14, 135.95, 135.92, 130.15, 130.06, 116.13, 115.91 and 53.59. ^{19}F{^{1}H} NMR (188 MHz, $CDCl_3$), δ(ppm): −105.61.

Synthesis of [MnL(CO)$_3$](CF$_3$SO$_3$); CORM-FBS.

In the dark conditions and under a nitrogen atmosphere, $Mn(CO)_5Br$ (82.2 mg, 0.30 mmol) and silver triflate (76.8 mg, 0.30 mmol) were dissolved in 15 mL dry acetone. The reaction mixture was stirred at 60 °C for 1.5 h. The reaction mixture was filtered under an inert atmosphere to separate the precipitate of silver bromide. To the filtrate, ligand (90 mg, 0.252 mmol) in 10 mL of dry and deoxygenated acetone was added and the reaction mixture was heated under reflux for 60 °C for 1.5 h. The reaction mixture was filtered off and washed with dry diethyl ether for several times to get pure CORM-FBS as a yellow solid (163 mg, 98%). Slow diffusion of ether into a $CHCl_3$ solution of CORM-FBS afforded yellow needle-like crystals suitable for X-ray crystallography.

^{1}H NMR (400 MHz, $CDCl_3$), δ (ppm): 8.84 (2H, d, J = 5.3 Hz, ArH); 8.13 (2H, s, ArH); 7.83 (2H,

s, ArH); 7.64 (2H, s, ArH); 7.52 (2H, s, ArH); 7.38 (2H, t, J = 6.1 Hz, ArH); 5.15 (2H, d, J = 15.9 Hz, CH_2); 4.66 (2H, d, J = 16.4 Hz, CH_2). ^{13}C NMR (125 MHz, $CDCl_3$), δ (ppm): 169, 167, 159, 152, 140, 134, 133, 126, 124, 119, 118, 62 and 31. $^{19}F\{^1H\}$ NMR (188 MHz, $CDCl_3$), δ(ppm): −78.17, −96.80. ESI-MS (m/z) $C_{22}H_{19}F_4MnN_3O_8S_3^-$, calculated for: 648, observed: 496 [CORM-FBS - OSO_2CF_3]. IR (ATR)$_\nu$ = 2037 cm^{-1} and 1928 cm^{-1}. Elemental analysis $C_{30}H_{26}F_3MnN_6O_8S_2$ calculated: C = 40.75%, H = 2.95%, F = 11.72%, Mn = 8.47%, N = 6.48%, O = 19.94%, S = 9.89%, found: C = 40.67%, H = 2.97%, N = 6.25%, S = 9.74 %.

Crystal Data [2] for CORM-FBS:

$C_{25}H_{24}F_3MnN_3O_{10}S_2$ [*][3], Mr = 721.53 $gmol^{-1}$[*], size 0.12 x 0.09 x 0.09 mm^3, space group P $\bar{1}$, a = 7.3643 (2), b = 14.0144 (4), c = 14.5978 (4) Å, α = 78.6520 (10) °, β = 81.8400 (10) °, γ = 88.2530 (10) °, V = 1462.17 (7) $Å^3$, T= -140 °C, Z = 2, $\rho_{calcd.}$ = 1.639 gcm^{-3}[*], μ (Mo-Kα) = 0.681 mm^{-1}[*], multi-scan, transmin: 0.9240, transmax: 0.9400, F(000) = 736 [*], reflections in h(-9/7), k(-18/18), l(-18/17), measured in the range 2.26° ≤ Θ ≤ 27.48°, completeness Θmax = 98.9%, 6631 independent reflections, R_{int} = 0.0192, 16315 reflections with I > 2σ(I), 408 parameters, 0 restraints, $R1_{obs}$ = 0.0332, wR^2_{obs} = 0.0753, $R1_{all}$ = 0.0357, wR^2_{all} = 0.0777, GOOF = 1.073, largest difference peak and hole: 0.397 / -0.438 e $Å^{-3}$.

[2] All single crystal X-Ray analysis in the dissertation were investigated by Dr. Helmar Görls.

[3] [*]: derived parameters do not contain the contribution of the disordered solvent.

5. Light-responsive paper strips as CO releasing material

The following section focuses on a novel manganese tricarbonyl photo-CORM with a strong colorimetric response upon illumination. This CORM-Dabsyl represented excellent stability in aqueous media under dark conditions and could be triggered by low intensity light to release CO. Meanwhile, the photochemical process was conveniently observed with the naked eye by the associated color change. CORM-Dabsyl was loaded on paper strips and these paper strips also achieved CO liberation upon exposure to light with a colorimetric response. It is the first time to use easily disposable and low-cost paper strips as a carrier to release CO. In addition, the ease of preparation and the dramatic difference of color allow this strategy a potential CO releasing material applicable for controlled drug delivery to biological targets.

5.1. Introduction

5.1.1. The introduction of dabsyl chromophore

Metal carbonyl complexes have gained increasing attention for quite long time as CO donors in biological systems. Alteration of the coordinated ligand frame is a promising strategy to develop novel CO releasing molecules. In this present work, a colorimetric dabsyl group was introduced. In the CORM-Dabsyl complex, the N,N'-dimethyl azo sulfonamide group was tethered to di-(2-picolyl)amine to form a symmetrical tridentate carbonyl ligand, which coordinated facially to manganese center. This conjugation promoted to present a visible color change from red to yellow upon irradiation, which resulted from a strong intramolecular charge transfer (ICT) in excited states. It is conveniently to examine CO liberation with the naked eye.

5.1.2. Evaluation CO release from CORMs under solvent free conditions

Besides myoglobin assay described in Chapter 3, diverse approaches are applied to determination CO release form CORMs, such as gas chromatography, IR spectroscopy and electrochemical method. Due to a solution medium is required and limitation of concentration for majority of

these strategies, a novel method without any additives was reported by Hubell at el. [228]

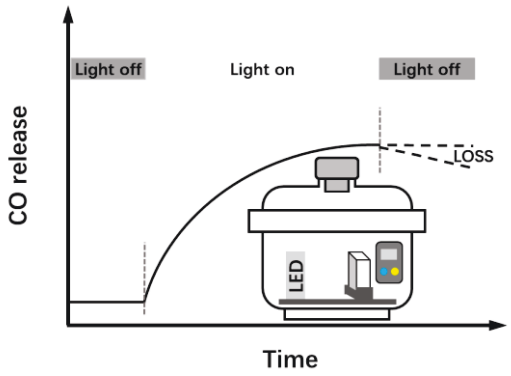

Figure 5.1 Experiment setup for the detection of CO release from CORMs with Draeger Pac 7000 under solvent free conditions.

The arrangement for CO-detection is shown in Figure 5.1, which is performed within an enclosed desiccator. The sample is commonly immobilized on the surface of cuvette with a fixed distance to a tunable LED light source. Alternation of light intensity is done outside the container. A portable CO detector (Draegor Pac 7000) is used for qualitative analyzing the amount of liberated CO. The released CO is calculated as an amount of CO in μM per mg sample and obtained from the following equation:

$$P\,V = n\,R\,T \qquad \text{(Equation 5.1)}$$

where P is the partial pressure of CO, V is the volume of experimental container, n is the number of moles of total gas, R is the gas constant and T is the temperature.

5.2. Results and Discussion

The following chapter describes the preliminary synthesis and general characterization of the light-responsive carbon monoxide releasing molecule with a colorimetric response from a dabsyl ligand. This CORM-Dabsyl molecule was stable under dark conditions and in oxygen-free aqueous media. Its photo-actions were spectroscopically examined and were observed with naked eyes. The DFT calculations and toxicity cell assay are also given.

5.2.1. Synthesis and Characterization of CORM-Dabsyl

$[MnL(CO)_3](CF_3SO_3)$, CORM-Dabsyl was obtained from the reaction of ligand ((E)-4-((4-(dimethylamino)phenyl)diazenyl)-N,N-bis(pyridin-2-ylmethyl)benzenesulfonamide) with the manganese carbonyl precursor with yield of 90% (Figure 5.2).

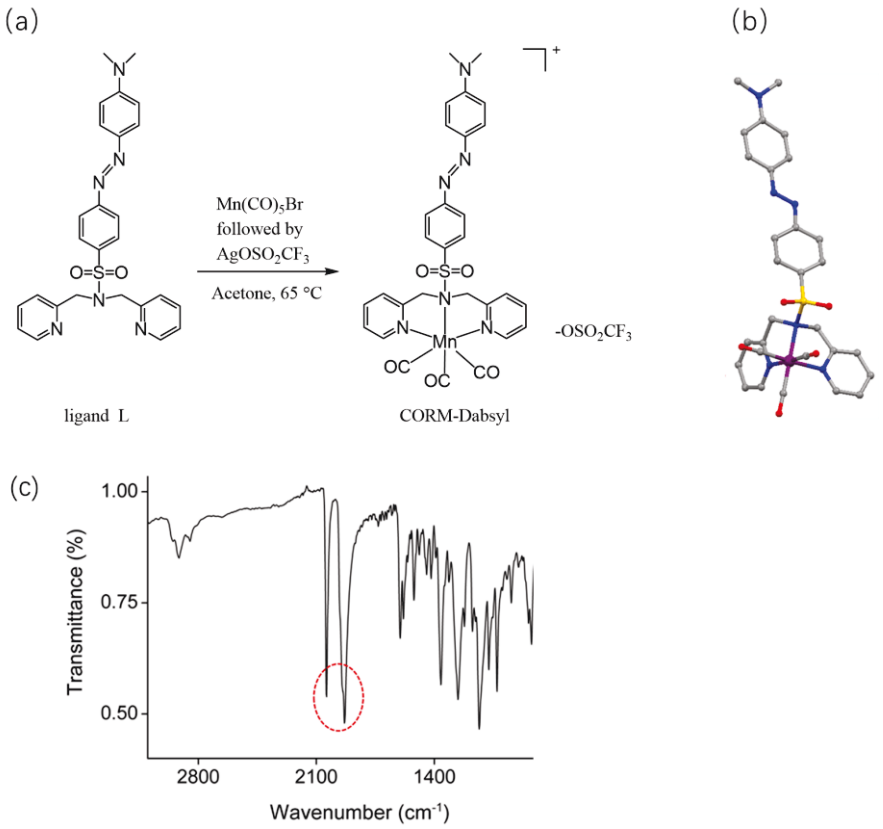

Figure 5.2 (a) Synthesis of CORM-Dabsyl. (b) X-ray crystal structure of CORM-Dabsyl. Solvent molecules, triflate anion and hydrogens in crystal structure are omitted for clarity; gray = carbon, blue = nitrogen, red =

oxygen, purple = manganese and yellow = sulphur. (c) IR spectrum of CORM-Dabsyl.

The analytical and spectroscopic data confirmed the successful synthesis and purity of ligand and CORM-Dabsyl. The solid-state X-ray crystal structure of CORM-Dabsyl (Figure 5.2 b) shows that there are three carbonyl ligands facially coordinated to the Manganese (I) center and opposite to the facially coordinated dipicolyl amine moiety. Based on literature, the Mn–N (sp^2) bond distances are generally in the range from 2.050(4) Å to 2.052(4) Å. While in the architecture, the Mn–N(sp^3) bond length was found to be unusually longer (2.161(3) Å) due to the superior coordinating ability of the sp^2 hybridized pyridine nitrogens compared to the sp^3 hybridized amine. The IR spectrum of CORM-Dabsyl displayed two asymmetric ν_{CO} bands at 2037 and 1928 cm^{-1}, which confirms the exist of three bonded CO. Furthermore, comparison of ^1H NMR spectra of ligand and CORM-Dabsyl shows that the methylene protons of the dipicolylamine moiety have singlet multiplicity for ligand and become two doublets for CORM-Dabsyl, which is explained by the fact that one pair projects towards and the other pair projects away from the carbonyl ligands mentioned in chapter 4. [225]

5.2.2. UV-Vis evaluation of ligand and CORM-Dabsyl under illumination

A comparison experiments of ligand and CORM-Dabsyl was performed at 405nm until no further spectral changes were observed. The electronic absorption spectra were measured in aqueous phosphate buffer (PB): DMSO (99:1, v/v) solution and compared to calculated spectra obtained by the TD-DFT (Figure 5.3 a).

Ligand L shows a strong absorption band at 415 nm (ε = 3.2 × 10^4 mol^{-1} L cm^{-1}), which is assigned to an intramolecular charge transfer (ICT) process from the N, N′-dimethylamine donor moiety to the azo (–N=N–) fragment by means of quantum chemical simulations. Moreover, TD-DFT predicts a bright state (S_2) at 424 nm that corresponds to the HOMO → LUMO ICT-transition on the dabsyl moiety. CORM-Dabsyl exhibits an intense absorption band in the visible region at 500 nm (ε = 3.3 × 10^4 mol^{-1} L cm^{-1}). TD-DFT estimates the bright excitation (S_0–S_2) at 464 nm, that corresponds to the same HOMO → LUMO transition, but with a distinct redshift compared to the ICT transition in L (ΔE = 0.37 eV, $\Delta\lambda_{max}$ = 84 nm).

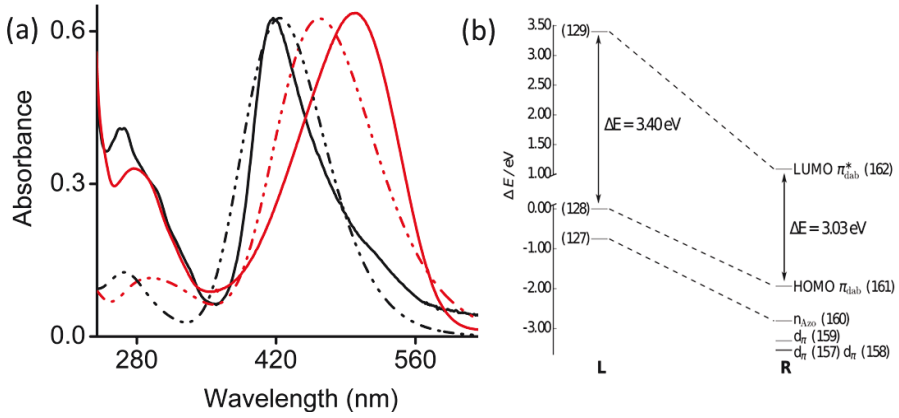

Figure 5.3. (a) Normalized experimental (solid) and theoretical (dashed) absorbance spectra of ligand L (black) and CORM-Dabsyl (red) in aqueous phosphate buffer: DMSO (99:1 v/v, pH 7.4). (b) Energy scheme of the frontier orbitals of ligand L and CORM-Dabsyl obtained at the M06/def2-TZVP level. All energies are in relation to the energy of the HOMO of L (MO 128). The orbital pairs (127, 160), (128, 161) and (129, 162) have the same character in ligand and CORM-Dabsyl.

Compared to ligand L, the CORM-Dabsyl introduces an $[Mn(CO)_3]^+$ fragment with a positive charge into the architecture. Through analyzing the atomic charges in CORM-Dabsyl via the intrinsic atomic orbitals (IAOs) theory, the $[Mn(CO)_3]$ moiety occupies only a charge of +0.4 *e* upon coordination while the majority of the positive charge of +0.6 *e* is delocalized over the co-ligand, which results in the stabilization of the frontier orbitals of CORM-Dabsyl. [229] The DFT calculation found that the HOMO of CORM-Dabsyl is stabilized by 1.94 eV, whereas the LUMO is stabilized by 2.31 eV. This situation contributes a smaller HOMO–LUMO gap in CORM-Dabsyl compared to L and the substantially observable redshift of the bright absorption feature assigned to the S_2 state (Figure 5.3 b).

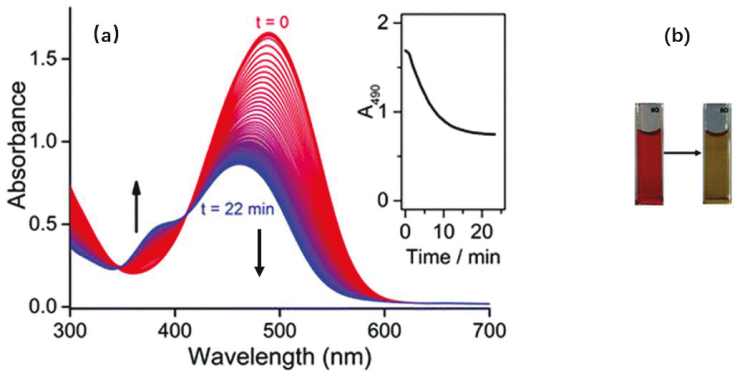

Figure 5.4 (a) Evolution of absorption spectra of CORM-Dabsyl (50 μM) in DMSO solution during blue light irradiation (424 nm, 23 mW). Time between spectra is 40 s. Inset: absorbance at 490 nm as a function

of irradiation time. (b) Pictures of the solution in a cuvette before (left) and after (right) the photoreaction.

The photoreaction was also measured in phosphate buffer (99:1, PB:DMSO, v/v), which can be assumed that the photoreaction quantum yield is similar in phosphate buffer and in neat DMSO because of the similar reaction rate. Both the ligand and CORM-Dabsyl are stable and no changes in absorbance were observed in the phosphate buffer under dark conditions for longer than 12 h. This proves the exceptional stability of the two compounds in solution on the part of oxidation and decomposition. Moreover, there were also no spectral observed of only ligand L under irradiation at 405 nm in PB solution, which weakens the possible effect on the observed absorption changes of UV-Vis spectra upon irradiation of CORM-Dabsyl resulting from photo-induced trans–cis isomerization. From these data, a photoreaction quantum yield of 0.5 ± 0.1% was calculated. The absorbance at 490 nm was observed decrease with a similar initial reaction rate, however, the precipitation of the photoproduct in this medium inhibited the further accurate study on photoreaction.

5.2.3. Myoglobin assay for CORM-Dabsyl and investigation of the CO-release mechanism

To determinate CO release from CORM-Dabsy, a very common technique myoglobin assay based on the spectral changes in absorption was applied. A freshly prepared concentrated solution of CORM-Dabsyl in oxygen-free DMSO was added to a buffered solution of horse skeletal myoglobin (Mb), and small excess sodium dithionite was added to capture the trace of incoming oxygen to prevent reaction with reduced myoglobin. Upon illumination of this mixture with light (405 nm, 8 mW cm^{-2}), the absorbance of deoxy-Mb at 557 nm decreased and the characteristic absorbance bands of Mb–CO at 540 and 577 nm grew and stabilized after 4 min, thereby confirming the binding of CO to Mb. In addition, a further same component myoglobin assay solution was kept in the dark for 60 min, to demonstrate the influence of sodium dithionite on CO-release from CORM-Dabsyl (Figure 5.5 a). The characteristic absorbance band did not decrease distinctly and no absorbance changes at 540 and 577 nm were observed. This confirms not only the stability of CORM-Dabsyl in the myoglobin solution under dark conditions, but also the stability against sodium dithionite. Hence, the release of CO was induced by light illumination

and not by the sodium dithionite. Thus, these data manifest CO release from CORM-Dabsyl upon irradiation at 405 nm. The amount of CO per CORM was calculated from these data and amounted to the near-complete release of three equivalents CO for each molecule CORM-Dabsyl (Figure 5.5). The previously calculated photoreaction quantum yield was therefore multiplied by 3, which gave a quantum yield of CO-release of 1.5 ± 0.2% (with 424 nm irradiation).

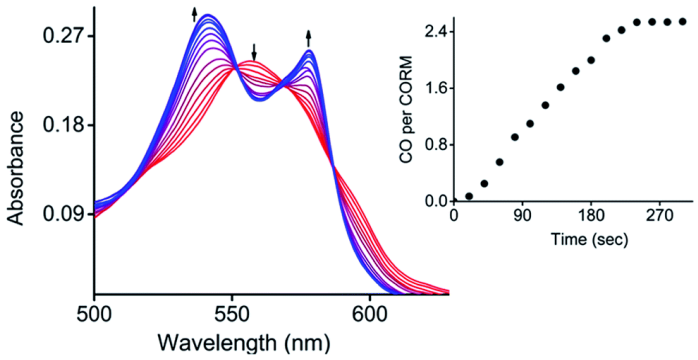

Figure 5.5 Conversion of deoxy-Mb to Mb–CO in a mixture of CORM-Dabsyl (15 µM) and deoxy-Mb (60 µM) in phosphate buffer (pH 7.4) upon exposure to light (405 nm, 8 mW/cm^2). Inset: CO release per CORM-Dabsyl *versus* time.

To identify which molecular orbitals are associated to the photochemical release of CO upon blue light illumination, TD-DFT calculations were performed. Several excited states were identified between 418 and 396 nm that correspond to excitations from the three (Mn–CO)-bonding d_π-orbitals, responsible for π-back bonding to CO, to (Mn–CO)-antibonding orbitals. While the d_π-orbitals feature mainly d-character, the MOs 167 and 168 correspond to antibonding linear combinations between π^*_{CO}- and the e_g-orbitals. [227] These data indicate that the photochemical activity of CORM-Dabsyl originates from orbitals around the Mn center and not start from ligand excited states that are populated with light above 418 nm (up to 600 nm). Even though there was a strong absorption of CORM-Dabsyl upon excitation with 480 nm light (Figure 5.6 b), no CO release is observed at all. This is considered as the absorption band of the dabsyl moiety in CORM-Dabsyl.

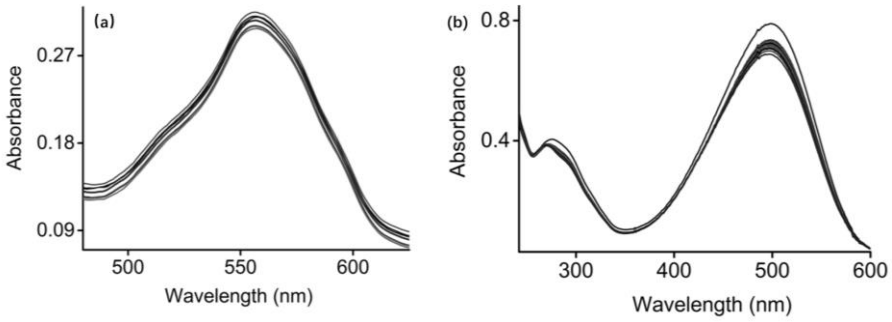

Figure 5.6 (a) Electronic absorption spectral traces of CORM-Dabsyl (15 μM) in presence of sodium dithionite and myoglobin (60 μM) recorded at dark conditions for every 10 min intervals in nitrogen bubbled phosphate buffer (PB: DMSO = 99:1, v/v, pH 7.4). (b) Electronic absorption spectral of CORM-Dabsyl irradiated with 480 nm light (8 mW/cm^2) recorded for every 20 sec intervals in phosphate buffer (PB: DMSO = 99:1, v/v, pH 7.4).

This result confirms that the complex only reacts with deep-blue light and that the photo-induced liberation of CO is not influenced by the colorimetric functional group dabsyl moiety. Whereas, the CT character of ligand intensely contributes to the charge distribution in vicinity of the manganese metal center (electronic ground state). Overall, it is established that CORM-Dabsyl is a highly stable CORM and that CORM-Dabsyl releases almost all three carbonyls under irradiation with low intensity light, concomitantly a remarkable colorimetric response.

5.2.4. Characterization of the inactive product after irradiation.

Diverse characterization approaches (such as ESR, NMR, IR spectroscopy, MS and DFT calculations) are performed to investigate the photo-product iCORM-Dabsyl. ^{13}C NMR spectroscopy demonstrated that the signal peak at 217.8 ppm for the CO molecules of CORM-Dabsyl disappeared upon irradiation of CORM-Dabsyl, which confirmed the successful CO release of CORM (Figure 5.7 b). ^{1}H NMR spectroscopy of photo-product manifested that the ligand L still combined with the Mn center through the observed proton signals without chemical shift (Figure 5.7 a). However, the broader signal peaks upon illumination compared to the initial CORM-Dabsyl exhibited the paramagnetic nature of the product, which is related to the oxidation status of manganese. Moreover, the comparison of X-band ESR spectrum (at 295 K) proved this assertion. The spectra of photolyzed solution of CORM-Dabsyl represents a six-line spectrum

indicative of a paramagnetic Mn(II) species (Mn^{II} - d_5) with high spin state (Figure 5.7 c), which is contrary to diamagnetic low-spin state of Mn^{I} - d_6 in CORM-Dabsyl. Meanwhile, the different possible spin states of iCORM-Dabsyl were investigated by DFT calculation. Considering the first three doublets, quartet and sextet states, within their equilibrium structures, MS-RASPT2 predicts a high spin sextet ground state, energetically favored with respect to the doublet (+1.79 eV) and quartet (+2.48 eV) ground state. In agreement with ESR, the sextet ground state corresponds to a $3d^5$ configuration on the Mn. Subsequently, the nature of the bright excitations underlying the absorption spectrum of the photoproduct were unraveled by means TD-DFT within sextet multiplicity. For iCORM-Dabsyl TD-DFT estimates two bright states (S_9 and S_{11}) at 496 nm and 477 nm. Their character is similar to the bright S_2 state as in ligand and CORM-Dabysl with additional charge-transfer from the azobenzene into the -orbitals. The ATR-IR spectra revealed the disappearance of the CO vibrational bands (between 1900–2100 cm^{-1}) after the irradiation at 405 nm, which clearly confirms that all three CO ligands were released from CORM-Dabsyl. This is in accordance with data from the myoglobin assay in aqueous solution. In addition, HRMS reported that the photolyzed product had a mass of 541.1222 m/z, which was attributed to [L + Mn] with an Mn(I) species.

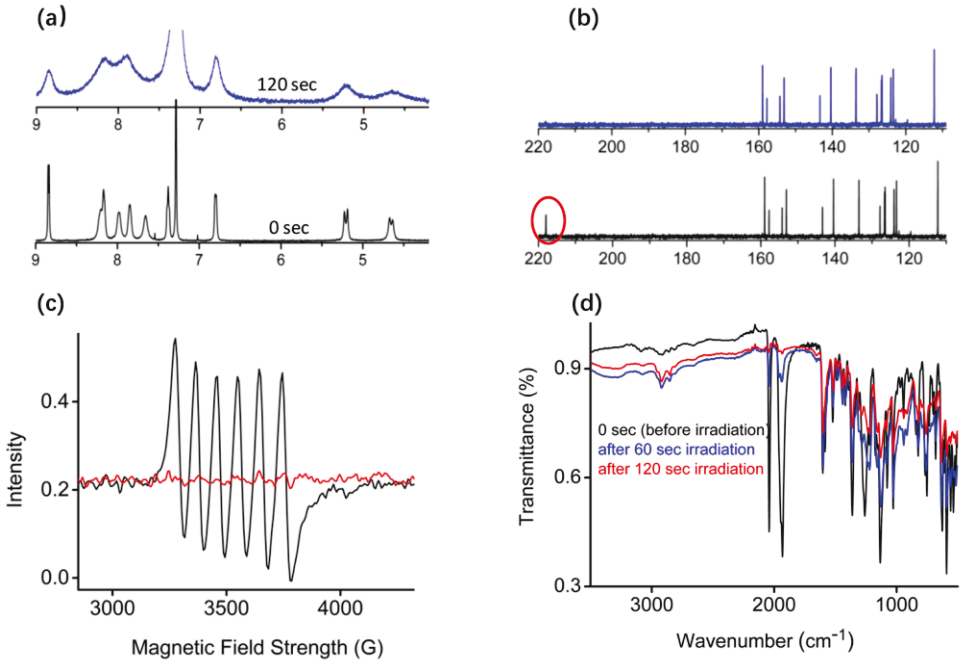

Figure 5.7. (a) Time-dependent partial ^{1}H NMR spectra of CORM-Dabsyl before (black) and after (blue) photolysis (405 nm, 8 mW/cm^2). (b) ^{13}C NMR spectra of CORM-Dabsyl before (black) and after (blue)

photolysis (405 nm, 8 mW /cm^2). (c) X-band ESR spectra (at 295 K) of CORM-Dabsyl (4 mM) before (red line) and after photolysis (black line) in DMSO: water (1:1, v/v). Microwave frequency, 9.87 GHz; modulation amplitude, 0.6 Mt; modulation frequency, 100 kHz and power of the microwave source, 1,262 mW. (d) ATR-IR spectra of CORM-Dabsyl before (black line) and after irradiation (blue and red line).

In summary, these data reveal that the manganese center is still conjugated to the ligand upon irradiation and CO release. The three carbonyl ligands of CORM-Dabsyl are in situ substituted by the solvent ligands in related solution media to form a positive charge product of $[MnL(solvent)_3]^{2+}$.

5.2.5. Toxicity of CORM-Dabsyl against human cell lines

To determine the potential cytotoxicity, CORM-Dabsyl was tested against two human hepatic model cell lines (HepaRG® and LX-2) by applying a common resazurin-based cell viability assay in the dark at standard cell culture conditions (Figure 5.8). [225] In vitro experiments it revealed that CORM-Dabsyl is mildly cytotoxic to both cell lines with EC50 values of 31 ± 5 µM (LX-2) and 26 ± 7 µM (HepaRG®) for an incubation time of 24 h. Nevertheless, these results convey the need for CORMs to be immobilized in a carrier material to prevent or reduce cytotoxic effects at the desired site of CO-release.

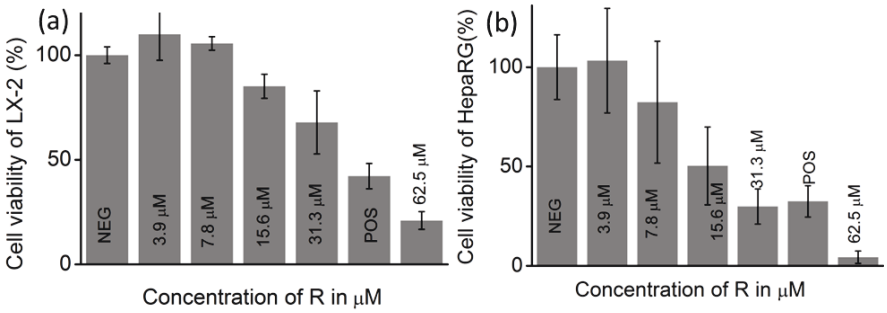

Figure 5.8 Relative cell viability percentage of (a) LX-2 cells and (b) HepaRG® cells that were treated for 24 h with medium only (NEG), 5 µM alpha-toxin (POS), or a concentration series of CORM-Dabsyl (3.9 µM – 62.5 µM).

5.2.6. Light-induced CO-release from paper strips

Due to the efficacious photo reactivity and stability of CORM-Dabsyl, a new strategy for light induced CO delivery material with a colorimetric response is developed. A 1 × 3 cm paper strip was immersed in a DCM solution (0.5 mL) containing high concentration of CORM-Dabsyl (0.5 mg). The absorption process completed within 2 mins, leaving a red paper with entire fluid had been homogeneously absorbed because of the capillary forces. Then the absorbed red paper strip was totally dried under air conditions for several minutes. In addition, this paper materials have strong stability which can be observed from the indeclinable color remained for couple weeks at room temperature in the air environments and the steady absorption band of aqueous supernatant solution in which the paper strips had been immersed for at least 15 min.

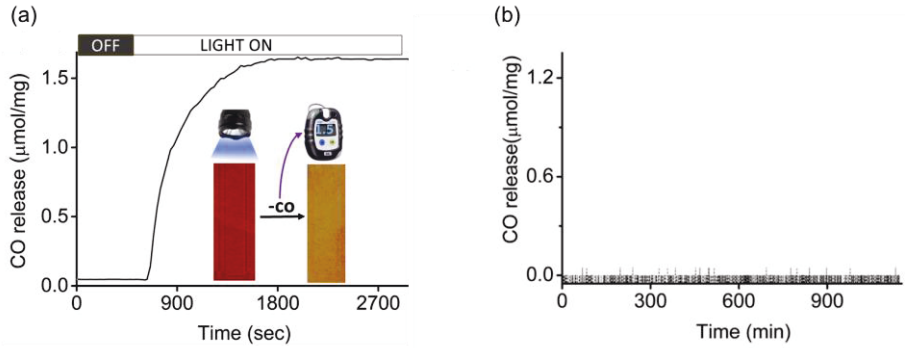

Figure 5.9 (a) Amount of CO released as a function of time during irradiation (λ_{irr} = 405 nm; 8 mW/cm^2) of paper strips loaded with CORM-Dabsyl with LED light in a closed desiccator. The inset shows the color change from red (before) to yellow (after) due to irradiation. (b) Amount of CO released as a function of time of a paper strip loaded with CORM-Dabsyl without LED irradiation in a closed desiccator.

To investigate the capability of light induced CO release from the pater strips, this material was determined with a portable CO sensor (Dräger Pac7000) under illumination with a 405 nm LED arrays (8 mW cm^{-2}).[200] As a result, a paper strip that containing 0.5 mg CORM-Dabsyl released around 1.5 µmol mg^{-1} CO exposure of light (λ_{irr} = 405 nm; 8 mW cm^{-2}) within 10 min. Furthermore, the color of the strips turned from red to yellow (Figure 5.9 a), in accordance with the statement of aqueous solution of CORM-Dabsyl previously mentioned.

Moreover, the yellow paper strip after light exposure of previous step depicted in Figure 5.9 was examined with ATR-IR spectroscopy immediately. The CO characteristic vibration bands (1900 – 2100 cm^{-1}) completely disappeared after irradiation, confirming the entire deliberation of CO.

Besides, the paper strip under same concentration conditions was repeated without illumination as a control experiment, remaining no CO release from the unchanged spectra during a 16 h measurement time (Figure 5.9 b). This further supports the outstanding stability of paper strips.

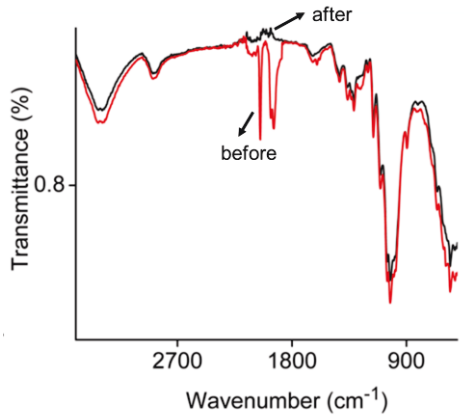

Figure 5.10 IR response of paper strip before and after irradiation.

In brief, these results reveal that the CO release only occurs under irradiation with proper light. This immobilized strategy for photo-CORMs exhibits excellent stability and efficient CO release, being highly promising for the controlled CO delivery materials. The method can simply cover the wounds or cuts to release CO at a requisite site like a Band-Aid. Moreover, this approach gives an immediate indication of possible CO releasing extent through the colorimetric response of the paper strips.

5.3. Summary and conclusion

In conclusion, a stable and water-soluble colorimetric CO-releasing molecule (CORM-Dabsyl) that releases three CO molecules upon photolysis is synthesized. The associated color change is easily observed by the naked eye. DFT and TD-DFT calculations are performed to investigate the CO release mechanism, contribution of dabsyl ligand and the properties of the photo-product iCORM-Dabsyl. Moreover, paper strips based on CORM-Dabsyl that acted as a CO-releasing material for convenient and efficient CO-release under illumination are the first time fabricated. The strong colorimetric response offers a direct visible estimation of CO release. The confinement of CORM-Dabsyl into paper strips allows on-demand release of CO at a biological site and the retention of mild toxic metal photo-product fragments. This study paves the way for the development of the next generation of CO-releasing materials.

5.4. Experimental section

5.4.1. General procedure

Materials and instrumentation.

$Mn(CO)_5Br$, silver triflate, di-(2-picolyl)amine, dabsyl chloride and triethylamine were purchased from Sigma-Aldrich. Solvents were purified and/or dried by standard techniques prior to use for all syntheses. ^1H NMR, ^{13}C NMR and ^{19}F NMR spectra were recorded on a Bruker AV 400 MHz NMR spectrometer in $CDCl_3$ or DMSO-d_6 at room temperature. Tetramethylsilane (TMS) served as an internal standard for ^1H NMR, and trichlorofluoromethane (CCl_3F) as an internal standard for ^{19}F NMR. Chemical shifts as related to the signals of the deuterated solvents used. UV-Vis absorption spectra were recorded with a spectrometer Specord S 600 UV-Vis from Analytic Jena. Mass spectra (ESI-MS) were acquired on a Finnigan MAT SSQ 710 or MAZ95XL device. Elemental analysis was performed on a Heraeus Vario EL III CHNS instrument. All IR (ATR) spectra were recorded in a range of 400 – 4000 cm^{-1} on a Bruker Vertex 70 FT-IR. Electron spin resonance (ESR) spectra on solution samples were recorded at X-band frequencies on a Bruker Elexsys E500 spectrometer.

General experimental methods for UV-Vis studies.

A 1 mM stock solution of CORM-Dabsyl and Dabsyl ligand were prepared in nitrogen-bubbled DMSO, which was used for all studies. For spectroscopic measurements, the DMSO stock solution was diluted with 10 mM phosphate buffer (PB, pH 7.2) to acquire a 15 µM solution in 1:99 v/v DMSO: PB, unless not otherwise mentioned. UV-Vis absorption spectra were recorded at room temperature in a quartz cuvette every 20 seconds during UV light exposure (UVP Benchtop 2 UV Transilluminator, ≤8 mW/ cm^2).

Photolysis Experiment.

Solution of CORM-Dabsyl (15 µM) in a quartz cuvette were exposed to different light sources (365 nm, 405 nm and 480 nm; 8 mW/cm^2) at every 20 seconds intervals to investigate the photoinduced CO-release studies. The power of the light sources was determined with a

PM100USB power meter.

Calculation of the quantum yield of photoactivation.

A solution of CORM-Dabsyl in DMSO (50 μM, volume V = 3.0 mL) was transferred to a stirred quartz fluorescence cuvette (1 cm pathlength) at 20 °C in a UV-Vis absorption spectrometry setup. Irradiation was performed with a high power 424 nm fiber-coupled LED (Thorlabs M420F2) that was connected to a collimating lens on top of the cuvette, thereby producing a 23.3 mW light beam through the solution (i.e. photon flux $\Phi = 8.26 \times 10^{-8}$ Einstein/s). UV-Vis spectra were recorded every second until the reaction was completed. The quantum yield (φ) of the photochemical reaction of CORM-Dabsyl was then calculated according to Equation 5.2. [230] It was assumed that the photoreaction proceeds with pseudo-first order kinetics, which is justified by the fact that we observe the spectral evolution of one species to the other without any intermediates.

$$\varphi = k \times n_{tot} / [\Phi \times (1 - 10^{A_{exc}})] \quad \text{(Equation 5.2)}$$

where k is the reaction rate constant, n_{tot} is the total amount of manganese complex in solution, and A_{exc} is the absorbance at the selected excitation wavelength (424 nm in this section). k was obtained from the slope of a plot of ln([CORM-Dabsyl]/(n_{tot}/V)) *versus* irradiation time, where [CORM-Dabsyl] was obtained at each timepoint i according to Equation 5.3:

$$[\boldsymbol{CORM\text{–}Dabsyl}] = (A_i^{487} - A_\infty^{487}) / [l \times (\varepsilon_{CORM-Dabsyl}{}^{487} - \varepsilon_{product}{}^{487})] \quad \text{(Equation 5.3)}$$

where $A_i{}^{487}$ is the absorbance at 487 nm at each timepoint i or at the end of the reaction (∞) and ε^{487} is the extinction coefficient at 487 nm (3.4×10^4 and 1.3×10^4 for CORM-Dabsyl and the photoproduct, respectively). φ had a value of 0.5% ± 0.1% under 424 nm irradiation. Since the photoreaction is accompanied by the release of three carbonyls, the quantum yield of CO-release was 1.5 ± 0.2% under 424 nm irradiation.

5.4.2. Synthesis and measurements

(E)-4-((4-(dimethylamino)phenyl)diazenyl)-N,N-bis(pyridin-2-ylmethyl)benzenesulfonamide (ligand).

Di-(2-picolyl) amine (105 mg, 0.5 mmol) and dabsyl chloride (162 mg, 0.5 mmol) were dissolved in 25 mL of dry tetrahydrofuran (THF). To this solution, triethylamine (0.1 ml) was added and stirred for 5 h at room temperature. A red-colored precipitate was filtered. The filtrate was concentrated and subjected to silica column chromatographic (eluent ethyl acetate and hexane in 1:1 (v/v)) purification to yield pure ligand as a red solid (150 mg, 61%).

^{1}H NMR (400 MHz, $CDCl_3$), δ (ppm): 8.39 (2H, d, J = 4.4 Hz, ArH); 7.94−7.87 (6H, m, ArH); 7.57 (2H, t, J = 7.2 Hz, ArH); 7.35 (2H, d, J = 7.6Hz, ArH); 7.10 (2H, t, J = 5.2 Hz, ArH); 6.79 (2H, d, J = 9.2Hz, ArH); 4.66 (4H, s, CH_2); 3.15 (6H, s, CH_3). ^{13}C NMR (100 MHz, DMSO-d_6): δ (ppm) 156.28, 155.50, 149.07, 143.61, 139.24, 136.52, 128.32, 125.72, 122.64, 122.46, 122.28, 111.47, 53.78 and 46.30. ESI-MS (m/z) $C_{26}H_{26}N_6O_2S$ calculated: 486.18, observed: 509.2 $[M+Na]^+$.

Synthesis of $[MnL(CO)_3](CF_3SO_3)$, CORM-Dabsyl.

In the dark conditions and under a nitrogen atmosphere, $Mn(CO)_5Br$ (110 mg, 0.40 mmol) and silver triflate (120 mg, 0.40 mmol) were dissolved in 15 mL dry acetone. The reaction mixture was stirred at 60 °C for 1.5 h. The reaction mixture was filtered under an inert atmosphere to separate the precipitate of silver bromide. To the filtrate, ligand (150 mg, 0.31 mmol) in 10 mL of dry and deoxygenated acetone was added and the reaction mixture was heated under reflux for 60 °C for 1.5 h. The reaction mixture was filtered off and washed with dry diethyl ether for several times to get pure CORM-Dabsyl as a dark red solid (180 mg, 74%). Slow diffusion of ether into a $CHCl_3$ solution of CORM-Dabsyl afforded orange red plate-like crystals suitable for X-ray crystallography.

^{1}H NMR (400 MHz, DMSO-d_6), δ (ppm): 8.95 (1H, d, J = 8.0 Hz, ArH); 8.84 (2H, d, J = 5.6 Hz, ArH); 8.62 (1H, t, J = 8.8 Hz, ArH); 8.46 (1H, d, J = 7.6 Hz, ArH);7.44− 7.78 (3H, m, ArH); 7.67 (1H, t, J = 8.0 Hz, ArH); 7.48 (2H, d, J = 7.6 Hz, ArH); 7.37 (2H, t, J = 6.0 Hz, ArH); 7.27 (1H, d, J = 8.8 Hz, ArH); 5.22 (2H, d, J = 16.4 Hz, CH_2); 4.35 (2H, d, J = 16.4 Hz, CH_2); 3.00 (6H, s, CH_3). ^{13}C NMR (125 MHz, DMSO-d_6), δ (ppm): 217, 159, 157,154, 143, 140, 133, 127, 126, 126, 124, 123, 112, 63 and 29. ^{19}F{^{1}H} NMR (188 MHz, DMSO-d_6), δ(ppm): −77.89. ESI-MS (m/z) $C_{31}H_{26}F_3MnN_6O_8S_2^-$, calculated for: 774, observed: 625 [CORM-Dabsyl - OSO_2CF_3]. IR (ATR)$_v$ = 2037 cm^{-1} and 1928 cm^{-1}. Elemental analysis $C_{30}H_{26}F_3MnN_6O_8S_2$ calculated: C = 46.52%, H =

3.38%, F = 7.36%, Mn = 7.09%, N = 10.85%, O = 16.52%, S = 8.28%, found: C = 46.07%, H = 3.39%, N = 10.50%, S = 8.03 %.

Crystal Data for CORM-Dabsyl:

$C_{31}H_{30}F_3MnN_6O_9S_2$[*], Mr = 806.67 $gmol^{-1}$[*], orange prism, size 0.134 × 0.122 × 0.108 mm^3, triclinic, space group P ī, a = 10.5628(2), b = 13.4613(3), c = 26.2818(5) Å, α = 79.225(1), β = 83.349(1), γ = 75.404(1)°, V = 3543.33(12) $Å^3$, T= −140 °C, Z = 4, $\rho_{calcd.}$ = 1.512 gcm^{-3}[*], μ (Mo-Kα) = 5.67 cm^{-1}[*], multi-scan, transmin: 0.6886, transmax: 0.7456, F(000) = 1656[*], 26160 reflections in h(-13/13), k(-17/17), l(-33/33), measured in the range 1.58° ≤ Θ ≤ 27.10°, completeness Θmax = 95.9%, 15002 independent reflections, R_{int} = 0.0266, 12901 reflections with $F_o > 4\sigma(F_o)$, 925 parameters, 0 restraints, $R1_{obs}$ = 0.0867, wR^2_{obs} = 0.2193, $R1_{all}$ = 0.0985, wR^2_{all} = 0.2279, GOOF = 1.041, largest difference peak and hole: 2.815 / −3.716 e $Å^{-3}$.

6. Colorimetric and fluorometric responsive photo-CORM

This chapter describes a novel manganese tricarbonyl photo-CORM with a colorimetric as well as fluorometric response upon irradiation with visible light. This CORM-NBD demonstrated superior stability in aqueous environment under normal day light conditions. Upon exposure to light with low intensity (at 490 nm), CORM-NBD releases almost all three CO with a visible color change from colorless to yellow as well as a strong luminescent response that centered at 560 nm. The associated colorimetric response gives a visible instant feedback of whether CO has been released and the turn-on luminescence makes it possible to track the CO delivery intracellular conditions. Additionally, TLC plates that loaded CORM-NBD complexes rapidly released CO under illumination. In vitro studies, LX-2 and HepaRG® human cell lines were used, which confirmed a low toxicity of CORM-NBD against the two cell lines. These results render CORM-NBD a novel CO releasing material to photodynamic therapy (PDT).

6.1. Introduction

6.1.1. The introduction of NBD group

Series of luminescent Mn(I)- and Re(I)- based carbonyl complexes as trackable photo-CORMs for CO delivery to cellular targets are published by Mascharak et al. [231–234] These photo-CORMs were proved to release CO upon exposure to light in human breast cancer cells or human colon cancer cells leading to a dose-dependent apoptotic cell death, and the turn-on luminescence promoted to track photolysis of CORMs within the cellular matrices. Inspired by those works, a nitrobenzodiazole (NBD) fluorophore with dual colorimetric as well as fluorometric response was used to increase the conjugation in the ligand, leading to absorption in the visible spectrum. This functional group was tethered to di-(2-picolyl)amine to form a symmetrical tridentate carbonyl ligand, which can coordinate facially to a manganese center. Upon illumination, fluorometric response occurs with visible color change due to photo-release of CO from CORM-NBD.

6.1.2. Biological studies of CO releasing molecules

The first step to develop a desired drug is commonly to identify a molecular target for the treatment of a selected disease. However, there is no identified definite molecule target or specific signaling pathways for carbon monoxide. Therefore, the biological studies of CORMs as drug agents need to be performed within cellular substrate with animal models of human diseases. [169] Mostly of biological applications of CO and CORMs focus on the inflammatory diseases, cardiovascular models and cancer cells. Inflammatory diseases generally start with the activation of macrophages and CORMs can be tested *ex vivo* with isolated macrophages or with macrophage cell lines. For instance, CORM-3 was tested in joint tissues and was proved to decrease the inflammatory response through increasing the levels of osteocalcin in the serum but also to protect against the degradation of cartilage and bone. [235] In cardiovascular disease models, CORMs are designed to exhibit protection of cells against death or accelerate specific endothelial cell proliferation. Chen et al. used CORM-2 to rescue OH-1-deficient mice from arterial thrombosis by reducing platelet aggregation in the graft. [236] Cancer cell experiments often use generated CO to inhibit cancer cell growth and induce apoptosis in cancer cells in a dose-dependent manner or time-dependent manner. [237] In this present work, parenchymal hepatocyte-like cell line HepaRG® and non-parenchymal hepatic stellate cell-like cell line LX-2 were used for in vitro studies. This will be introduced in subchapter 6.2.6.

6.2. Results and Discussion

The following chapter describes the preliminary synthesis and general characterization of the light-responsive carbon monoxide releasing molecule with a fluorometric dual response from a nitrobenzodiazole (NBD) fluorophore ligand. This CORM-NBD molecule was stable under dark conditions and in oxygen-free aqueous media. Its photochemical activities were spectroscopically examined and were observed with naked eyes. The DFT calculations and toxicity cell assay are also given. A low toxicity of photo-CORM was observed against LX-2 and HepaRG® human cell lines.

6.2.1. Synthesis and Characterization of CORM-NBD

$[MnL(CO)_3](CF_3SO_3)$, CORM-NBD was obtained from the reaction of the tridentate ligand containing a nitrobenzodiazole group with the manganese carbonyl precursor with yield of 60% (Figure 6.1).

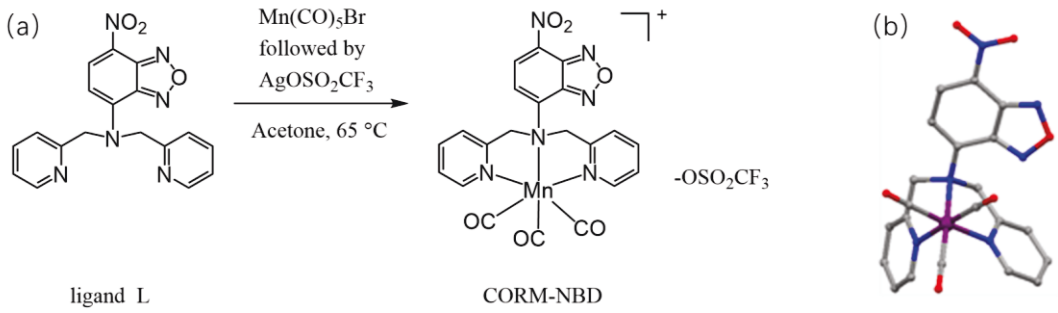

Figure 6.1 (a) Synthesis of CORM-NBD. (b) X-ray structure of CORM-NBD. Solvent molecules, triflate anions and hydrogens are omitted for clarity; gray = carbon, blue = nitrogen, red = oxygen and purple = manganese.

The analytical and spectroscopic data confirmed the successful synthesis and purity of ligand and CORM-NBD. The solid-state X-ray crystal structure of CORM-NBD (Figure 6.1 b) represents that there are three electron withdrawing carbonyl ligands facially coordinated to the octahedral Manganese (I) center and opposite to the each of the three nitrogen atoms of facially coordinated dipicolyl amine moiety. Slimier to CORM-Dabsyl in chapter 5, the Mn–N(sp^3) bond

length (2.161(2) Å) in the architecture of CORM-NBD was also found to be longer the other Mn–N (sp^2) bond distances 2.042(2) Å and 2.050(2) Å, which supports that the superior coordinating ability of the sp^2 hybridized pyridine nitrogens compared to the sp^3 hybridized amine. The IR spectrum of CORM-NBD displayed three typical ν_{CO} bands at 2033, 1954 and 1932 cm^{-1}, respectively. This pattern of Figure 6.2 confirms the exist of three bonded CO and accords with the known manganese complexes in literature.

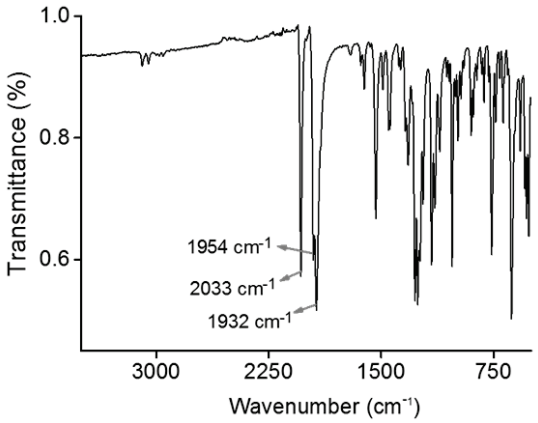

Figure 6.2 IR spectrum of CORM-NBD.

Furthermore, comparison of ^1H NMR spectra of ligand and CORM-NBD shows that the methylene protons of the dipicolylamine moiety have singlet multiplicity for ligand (δ = 5.44 ppm) and become two doublets for CORM-NBD (δ = 5.63−5.59 and 4.83−4.79 ppm). Due to the different project direction (towards and away) to the carbonyl ligands on the manganese center, the two nonequivalent magnetically methylene group are considered as endo- and exo-CH protons. [225]

6.2.2. UV-Vis evaluation of ligand and CORM-NBD under illumination

A comparison experiments of ligand and CORM-NBD was performed at 480 nm at room temperature until no further spectral changes were observed. The electronic absorption spectra were measured in aqueous phosphate buffer (PB): DMSO (99:1, v/v) medium and compared to calculated spectra obtained by the TD-DFT (Figure 5.2 a).

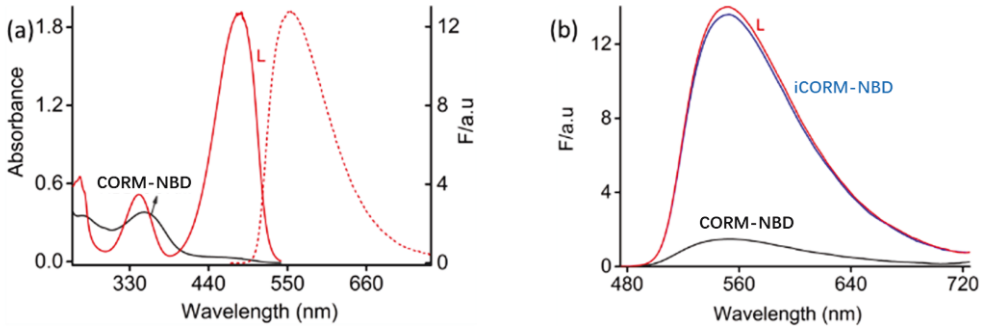

Figure 6.3. (a) Electronic absorption spectrum of L & CORM-NBD and luminescence spectrum (λ_{ex} = 440 nm) of L (dotted line). (b) Luminescence spectrum of L and changes in luminescence spectra of CORM-NBD before and after (iCORM-NBD) photolysis (480 nm; 8 mW cm^{-2}).

Ligand L shows two distinct absorption band at 343 nm (ε = 5.1 × 10^4 mol^{-1} L cm^{-1}) and 480 nm (ε = 1.9× 10^5 mol^{-1} L cm^{-1}). The former is less intense absorption band, which is assigned to the intramolecular charge transfer (ICT) process from the N, N′-dimethylamine donor moiety to the oxadiazole (–N=N–) fragment by means of quantum chemical simulations. Moreover, TD-DFT predicts this transition (S_7) at 318 nm. Whereas, the intense low energy absorption band results from a bright $\pi_{NBD} \rightarrow \pi^*_{NBD}$ excitation (S_1) on the NBD moiety estimated at 412 nm by TD-DFT. CORM-NBD exhibits an intense absorption band in at 353 nm, that corresponds to the state S_{15} at 333 nm predicted by calculations. This is assigned to an ICT process contributed with S_7 in ligand and additional metal to ligand charge transfer (MLCT). Upon excitation at 440 nm, ligand L represents a strong emission band with a λ_{max} of 553 nm. In addition, the relative emission quantum yield for ligand (Φ_L) in the mixture buffer was found to be 0.12 (using fluorescein as a standard). Compared to ligand L, the relative emission quantum yield for ligand ($\Phi_{CORM\text{-}NBD}$) was 0.014 through calculation on photoluminescence spectra data (λ_{ex} = 440 nm and λ_{em} = 553 nm) in the buffer circumstance. This quenching of NBD fluorophores group results from the conjugation with three electron withdrawing CO ligands upon the formation of CORM-NBD.

Time evolution of UV-Vis absorption spectra of CORM-NBD (50 μM, 3 mL) in nitrogen bubbled buffer media (PB:DMSO, 99:1, v/v) was recorded every 2 min. Upon irradiation with light (490 nm, 23 mW), CORM-NBD exhibited two main absorption bands at 353 nm and 480 nm respectively were shown in the Figure 6.3 a. With illumination time increasing, the absorption band at 353 nm was observed to decrease gradually and a new absorption band at around 480 nm

grew and increased with an isosbestic point at 411 nm. Simultaneously occurred the color change of the solution from colorless to yellow.

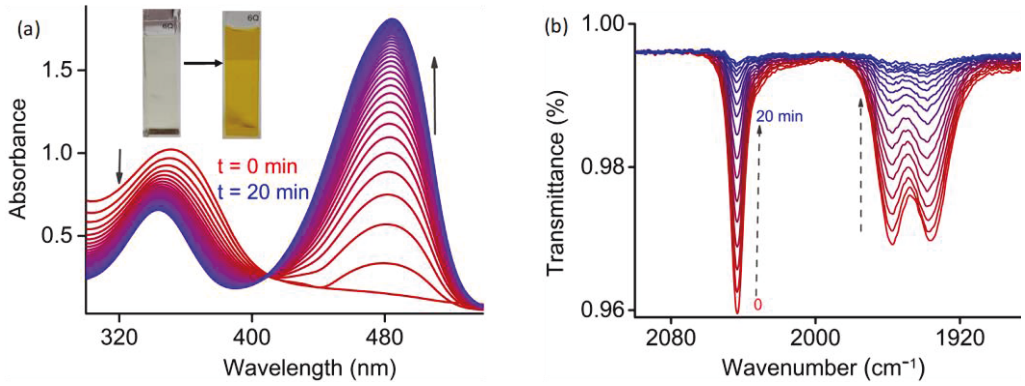

Figure 6.3 (a) Time evolution of absorption spectra of CORM-NBD (20 µM) in 3 mL DMSO solution during irradiation (490 nm, 23 mW). Time between spectra is 2 min. Inset: Pictures of the solution in a cuvette before (left) and after (right) the photoreaction. (b) Time evolution of liquid-phase IR spectra during irradiation of CORM-NBD solution (10 mM) recorded every 1.5 min.

The photoreaction was also measured at normal day light conditions. No changes in absorbance were observed in the phosphate buffer over a course 4 h, confirming the stability of compound in solution environment under ambient light conditions. Moreover, it is clearly observed that the characteristic vibration bands of carbonyls at 2032, 1954, and 1932 cm^{-1} completely disappeared in 30 min with irradiation even at high concentrations from the liquid-phase IR spectra for CORM-NBD (Figure 6.3 b). This confirms that all three carbonyls release. It could be assumed that the extended conjugation and the electron withdrawing nitro group in the ligand π-frame promotes the CO deliberation upon illumination at low energy (490 nm).

6.2.3. Myoglobin assay for photo-CORM and investigation of the CO-release mechanism

To determinate CO release from CORM-NBD, a myoglobin (Mb) assay was performed. A fresh solution of CORM-NBD in oxygen-free DMSO was added to a buffered solution of myoglobin to get a 15 µM CORM-NBD mixture. Then sodium dithionite was added. Upon illumination of this mixture with light (480 nm, 8 mW/cm^2), the absorbance of deoxy-Mb at 557 nm decreased and

the characteristic absorbance bands of Mb–CO at 540 and 578 nm in the Q-band region grew and stabilized, thereby confirming the binding of CO to myoglobin. In addition, a further myoglobin assay solution was kept in the dark for 60 min, to investigate the influence of sodium dithionite on CO-release from CORM-NBD (Figure 6.4 b). The characteristic absorbance band did not decrease obviously and there were no absorbance changes at 540 and 577 nm. This confirms the stability of CORM-NBD in the myoglobin solution under dark conditions and the stability against sodium dithionite. Hence, the release of CO was actually triggered by light illumination and not by the sodium dithionite. Thus, these data demonstrate that CORM-NBD successfully releases CO upon irradiation at 480 nm. The amount of CO per CORM was calculated from these data and amounted to the near-complete release of three equivalents CO for each molecule CORM-NBD.

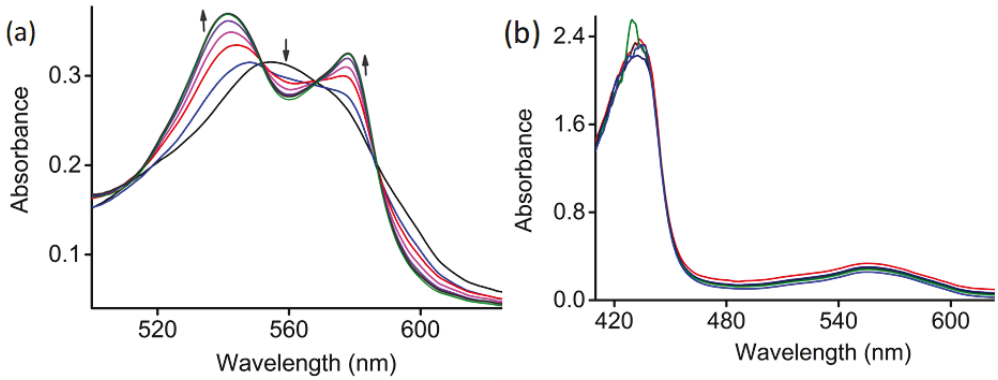

Figure 6.4 (a) Conversion of deoxy-Mb to Mb–CO in a mixture of CORM-NBD (15 μM) and reduced Myoglobin (60 μM) in phosphate buffer (pH 7.4) upon exposure to light (480 nm, 8 mW/cm^2). (b) Electronic absorption spectral traces of CORM-NBD (15 μM) in presence of sodium dithionite and reduced myoglobin (60 μM) recorded at dark conditions for every 10 min intervals in nitrogen bubbled buffer media (pH 7.4).

Furthermore, a time-dependent fluorescence spectrum was applied in the buffer media (PB:DMSO, 99:1, v/v, pH 7.4) with irradiation at 480 nm. In agreement with the result observed from the UV-Vis spectra, the fluorescence intensity of CORM-NBD solution increased with time upon illumination. This indicates the liberative NBD group emit fluorescence due to the loss of electron withdrawing CO ligands. Then, a photochemical reaction kinetic rate constant k_{CO} = 5 min^{-1} (T = 22 °C) for the CO release was given through analyzing the fluorescence intensity at 553 nm against time (Figure 6.5 b).

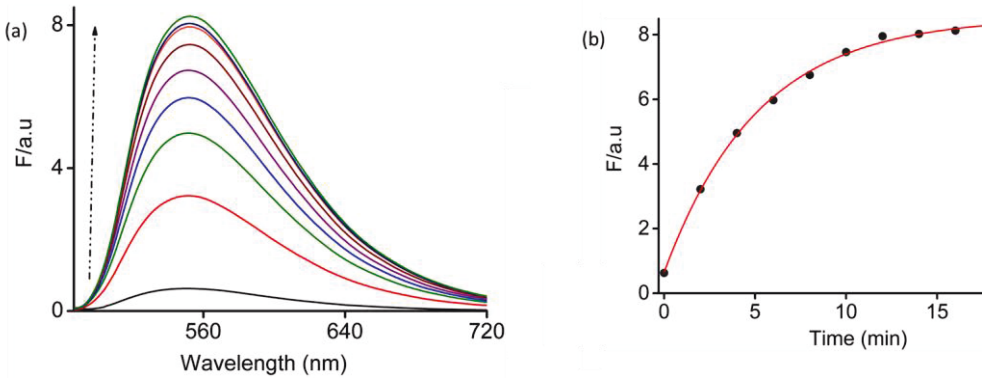

Figure 6.5 (a) Time-resolved luminescence traces of CORM-NBD in buffer media (PB: DMSO, 99:1, v/v, pH 7.4) upon exposure to low-power visible light illumination (480 nm, 8 mW/cm^2) at 3 min intervals. (b) Plot of fluorescence intensity at 553 nm *vs* time (solid line as monoexponential curve fitting, apparent rate constant k_{CO} = 5 min^{-1}).

To further investigate the mechanism of the photochemical CO release upon illumination, TD-DFT calculations were performed. A low lying excited states (S_1) were identified at 461 nm that correspond to excitations from the d_π-orbitals to π^*_{NBD} MLCT state (Figure 6.6). The excitation from three (Mn–CO)-bonding d_π-orbitals undermined the electron density at the manganese center, resulting in a weakening of the π-back bonding interaction between Mn and CO ligands. This led to the ultimate CO release. The quantum yields of CO release for CORM-NBD at different wavelengths were measured at 365 nm, 413 nm, 450 nm and 490 nm and $\Phi_{CORM\text{-}NBD}$ were found to be 8.0%, 7.7%, 3.5% and 1.2%, respectively. [230] Several excited states (S_{11}–S_{13}) were identified between 358 nm and 361 nm that corresponded to mixed MLCT and ligand field states (LF) with local $d_\pi \rightarrow d^*_\sigma$ orbitals. The transitions S_1 presented a π^*_{NBD} orbital that populated with an orbital nonbonding towards the CO ligands, while the populated d^*_σ orbitals were directly antibonding towards the CO ligands which further supported the CO release. Generally pure d-d LF transitions would be spin-forbidden but the electronic transitions in the S_{11}−S_{13} spun in two ways. These data indicate that the photochemical activity of CORM-NBD originates from linear d_π orbitals combinations of d_{Mn} and π^*_{CO} orbitals. Hence, the starting d_π orbitals are considered as an admixture of $d_\pi \rightarrow \pi^*_{NBD}$ MLCT character, resulting in nonzero oscillator strengths for state S_{11}−S_{13}.

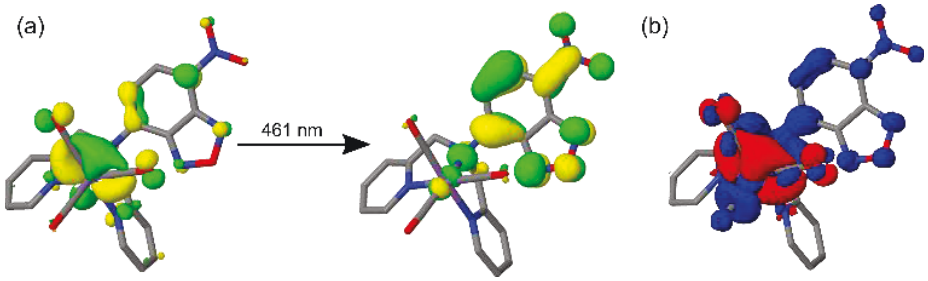

Figure 6.6 Illustrations of the bright MLCT state (S_1) at 461 nm as predicted by TD-DFT. (a) Natural Transition Orbitals (ρ = 0.04 electrons/au^3); (b) Charge Density Difference (ρ = 0.001 electrons/au^3). Transfer of electron density from the metal center onto the L leads to CO release. Hydrogens were omitted for clarity.

This result confirms that the complex can be triggered by UV and visible light with low intensity to release all three coordinated CO, accompanying with fluorometric dual response and obviously color conversion in solution. The photochemical reaction of CORM-NBD starts from the mixture of d_π orbitals that consisted of d orbitals of manganese center and antibonding π orbitals of carbonyls.

6.2.4. Characterization of the inactive product after irradiation

The photo-product of CORM-NBD upon illumination was also determined with diverse characterization strategies. Time-dependent partial ^{1}H NMR spectra of CORM-NBD before and after photolysis (480 nm, 8 mW/cm^2) with different time intervals were shown in Figure 6.7 (a).

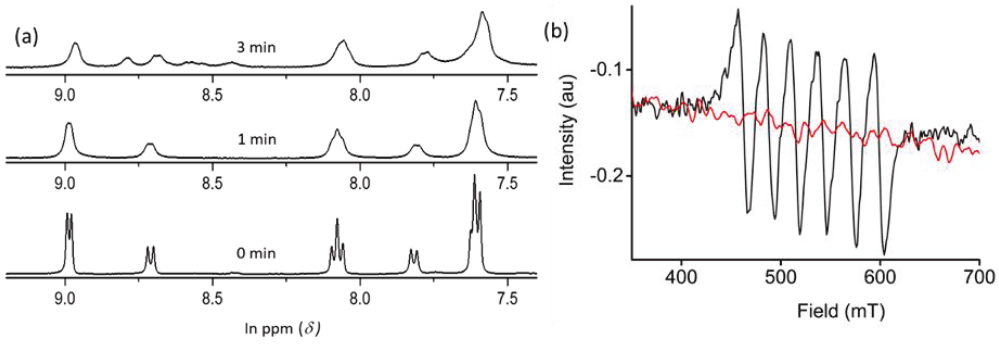

Figure 6.7 (a) Time-dependent partial ^{1}H NMR spectra of CORM-NBD before and after photolysis (480 nm, 8 mW/cm^2) at different time intervals in CD_3CN solution. (b) X-band ESR spectra (at 295 K) of CORM-NBD (4 mM) before (red line) and after photolysis (black line) in DMSO: water (1:1, v/v). Microwave

frequency, 9.8509 GHz; modulation amplitude, 0.6 Mt; modulation frequency, 100.

^{1}H NMR spectroscopy of photo-product at different time intervals demonstrated that the ligand L still combined with the Mn center through the observed proton signals without chemical shift (Figure 6.7 a) as well as the broader aromatic signal peaks upon illumination were related to the oxidation status of manganese core in the inactive product. Moreover, the comparison of X-band ESR spectrum (at 295 K) was performed to further identify the magnetism and oxidation status of Mn. The spectra of photolyzed solution of iCORM-NBD represent a six-line spectrum indicative of a paramagnetic Mn(II) species (Mn^{II} -d_5) with high spin state, which is converted from a diamagnetic low-spin state of Mn^{I} -d_6 in CORM-NBD. Similar to CORM-FBS and CORM-Dabsyl, the photo-product could be described as the formula of $[MnL(solvent)_3]^{2+}$, conjugating ambient solvent molecules in the position where occupied by dissociated carbonyls to the manganese center.

6.2.5. Light-induced CO-release from alumina TLC plates

In this section, CORM-NBD was immobilized on the alumina TLC plates to support the CO release from solid status photo-CORMs. The plates were loaded with loaded with 2.0 mg CORM-NBD and then released around 150 ppm CO upon irradiation with 480 nm over 30 minutes. In addition, the color change before and after illumination could be observed by naked eye. As a comparison experiment, a stick loaded with CORM-NBD at same concentrations was detected in ambient light environments without irradiation. No free CO was monitored, testifying the stability of CORM-NBD under dark or day light conditions.

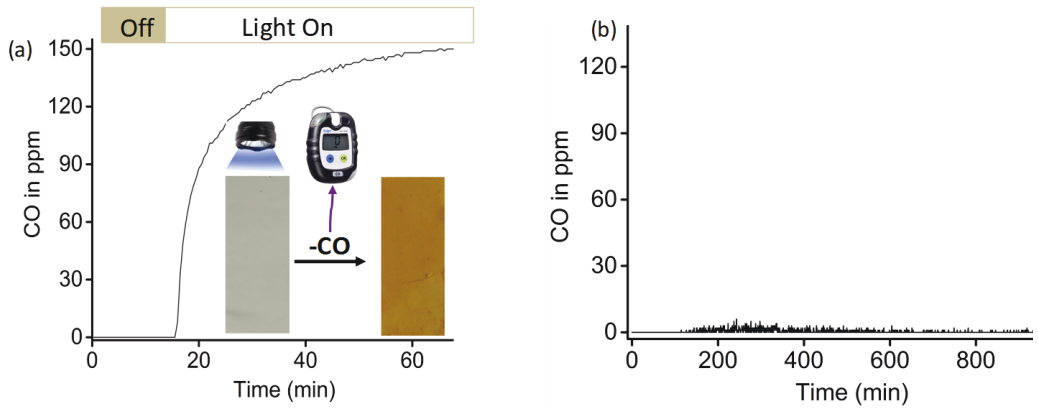

Figure 6.8 (a) Amount of CO released as a function of time during irradiation with LED light (λ_{irr} = 480 nm; 8 mW/cm^2) of plate sticks loaded with CORM-NBD in a closed desiccator. The inset shows the color change from colorless (before) to yellow (after) due to irradiation. (b) Amount of CO released as a function of time from paper strip loaded with CORM-NBD in ambient light conditions without LED irradiation in a closed desiccator.

6.2.6. Toxicity of CORM-NBD against human cell lines

Inspired by the turn-off/on luminescence response of CORM-NBD before and after illumination, the immortalized hepatic stellate cell line LX-2 was utilized to track the inclusion of the CORM complex and CO release with confocal laser scanning microscopy (CLSM). The CLSM images (Figure 6.9 a−d) showed a turn-on fluorescence by the cells displayed in the green channel after irradiation with light at 470 nm, which demonstrates the abilities of cellular uptake of CORM-NBD and control over the CO release driven by visible light inside living cells. To determine the potential cytotoxicity, CORM-NBD and iCORM-NBD were tested against two human hepatic model cell lines (parenchymal HepaRG® and non-parenchymal LX-2) by applying a well-established cell viability assay in the dark at standard cell culture conditions (Figure 6.9 e and f). [225]

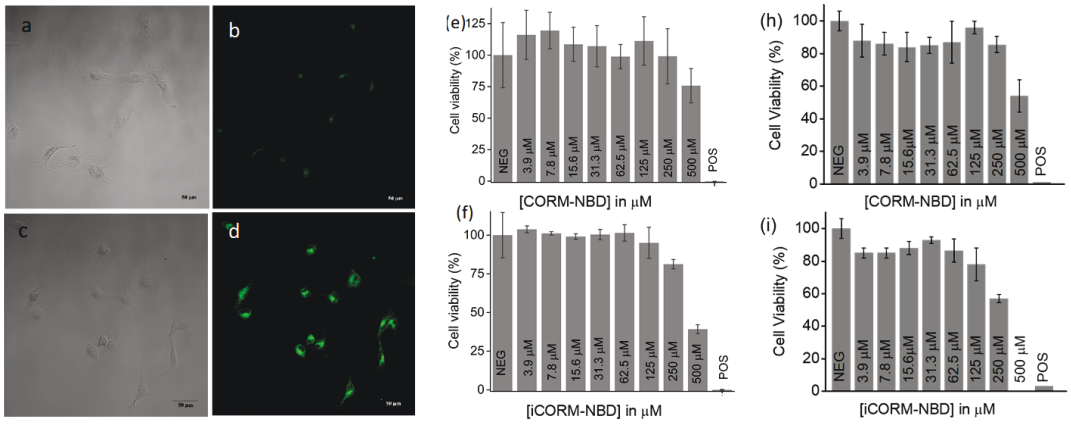

Figure 6.9 Relative cell viability percentage of (a) LX-2 cells and (b) HepaRG® cells that were treated for 24 h with medium only (NEG), 5 µM alpha-toxin (POS), or a concentration series of CORM-NBD (3.9 µM – 62.5 µM). Confocal laser scanning microscopy (CLSM) images of LX-2 cells incubated with 20 µM of

NBD-CORM for 30 min at 37 °C (λ_{ex} = 488 nm; λ_{em} = 555 nm: (a,c) bright-field images, (b) image without light exposure and (d) image recorded after irradiation with low power LED light (λ_{irr} = 470 nm). Cell viability of LX-2 cells in percentage for e) NBD-CORM and f) NBD-iCORM (NEG = non-treated, POS = 0.05 % sodium dodecyl sulphate).

In vitro experiments revealed that CORM-NBD was no cytotoxic to both cell lines even with up to a concentration of 250 μM or higher. While for iCORM-NBD against HepaRG®, a reduction of viability was found at a concentration of 250 μM or higher, resulting in more than 30 % cell viability loss. The CO-depleted molecule showed remarkable toxicity only at the highest tested concentration of 500 μM, indicating a highly promising biocompatible CO carrier molecule of CORM-NBD.

6.3. Summary and Conclusion

In conclusion, a colorimetric as well as fluorometric dual response CO-releasing molecule (CORM-NBD) that releases all three CO molecules upon photolysis at low energy light is introduced. The easily observed colorimetric response provides a directly visible estimation of CO release by the naked eye. The turn-on luminescence achieves to track the CO delivery within the cells from the cellular imaging experiments on LX-2 cells and HepaRG® cells. DFT and TD-DFT calculations are studied to investigate the CO release mechanism. Moreover, TLC plate sticks that loaded CORM-NBD release CO immediately under illumination with strong colorimetric response. These make CORM-NBD a promising candidate to conduct as CO releasing material in therapeutic application.

6.4. Experimental section

6.4.1. General procedure

Materials and instrumentation.

$Mn(CO)_5Br$, silver triflate, di-(2-picolyl)amine, 4-chloro-7-nitrobenzofurazan and fluorescein were purchased from Sigma-Aldrich. Solvents were purified and/or dried by standard techniques prior to use for all syntheses. ^1H NMR, ^{13}C NMR and ^{19}F NMR spectra were recorded on a Bruker AV 400 MHz NMR spectrometer at room temperature using $CDCl_3$, CD_3CN and DMSO-d_6 as the solvents. Tetramethylsilane (TMS) and trichlorofluoromethane (CCl_3F) were used as internal standards for ^1H NMR and ^{19}F NMR, respectively. Chemical shifts as related to the signals of the deuterated solvents used. UV-Vis absorption spectra were recorded with a spectrometer Specord S 600 UV-Vis from Analytic Jena. Mass spectra (ESI-MS) were acquired on a Finnigan MAT SSQ 710 or MAZ95XL device. Mass spectra were acquired on a Finnigan MAZ95XL device. Elemental analysis was performed on a Vario EL III CHNS instrument. All IR (ATR) spectra were recorded on a Bruker Vertex 70 FT-IR spectrometer. Electron spin resonance (ESR) spectra on solution samples were recorded at X-band frequencies on a Bruker Elexsys E500 spectrometer.

General experimental methods for UV-Vis and fluorescence studies.

A 1 mM stock solution of CORM-NBD and ligand L were prepared in nitrogen-bubbled DMSO, which was used for all the studies. Unless not otherwise mentioned, the DMSO stock solution was diluted with 10 mM phosphate buffer (PB, pH 7.2) and the diluted solution was used for all spectroscopic studies. For spectroscopic measurements, DSMO stock solution was further diluted with phosphate buffer (PB: DMSO, 99:1, v/v) and the effective final concentration was made as 10 μM. All luminescence measurements were done using $\lambda_{ex} = 440$ nm with an emission slit width of 3 nm. The fluorescence quantum yield was determined according to literature method using fluorescein (in 0.1 M NaOH) as reference ($\Phi_f = 0.92$). Each spectrum was recorded at room temperature with a quartz cuvette at regular time intervals of UV light exposure (UVP Benchtop 2

UV Transilluminator, ≤10 mW/cm^2) at different wavelengths.

Photolysis Experiment.

Solution of CORM-NBD (15 μM) in a quartz cuvette were exposed to different light sources (365 nm, 405 nm and 480 nm; 8 mW/cm^2) at every 20 sec intervals to investigate the photoinduced CO-release studies. The power of the light sources was determined with a PM100USB power meter.

Calculation of the quantum yield of photoactivation.

A solution of 8.3 μM CORM-NBD in 1/99 DMSO/PBS (v/v, V = 3.0 mL) was transferred to a stirred quartz fluorescence cuvette (1 cm pathlength) at 20 °C in a UV-Vis absorption spectrometry setup. Irradiation was performed with different wavelength LEDs (365, 413, 450, and 490 nm) that were mounted on top of the cuvette using a custom-build holder that fit exactly on top of the cuvette. Photon fluxes (Φ) were determined by ferrioxalate actinometry and had values of 1.9×10^{-8}, 2.2×10^{-8}, 1.3×10^{-7}, and 6.1×10^{-8} einstein/s at 365, 413, 450, and 490 nm, respectively. UV-Vis spectra were recorded every second until the reaction was completed. The quantum yield (φ) of the photochemical reaction of CORM-NBD was then calculated according to the following equation. [209] It was assumed that the photoreaction proceeds with pseudo-first order kinetics, which is justified by the fact that we observe the spectral evolution of one species to the other without any intermediates.

$$\varphi = k \times n_{tot} / [\Phi \times (1 - 10^{A_{exc}})] \qquad \text{(Equation 6.1)}$$

where k is the reaction rate constant, n_{tot} is the total amount of manganese complex in solution, and A_{exc} is the absorbance at the selected excitation wavelength. k was obtained from the slope of a plot of ln([CORM-NBD]/(n_{tot}/V)) *versus* irradiation time, where [CORM-NBD] was obtained at each timepoint i according to a method reported by Bahreman to deconvolute the two species' concentrations in time using the molar absorption coefficient at two-wavelengths: at 350 nm ($\varepsilon_{CORM\text{-}NBD}$ = 10800, $\varepsilon_{product}$ = 6290) and 480 nm ($\varepsilon_{CORM\text{-}NBD}$ = 870, $\varepsilon_{product}$ = 22000). φ had values of 8.0%, 7.7%, 3.5%, and 1.2% at 350, 413, 450, and 490 nm, respectively. [230]

6.4.2. Synthesis and measurements

(E)-4-((4-(dimethylamino)phenyl)diazenyl)-N,N-bis(pyridin-2-ylmethyl)benzenesulfonamide (L).

Di-(2-picolyl)amine (200 mg, 1.0 mmol) and 4-chloro-7-nitrobenzofurazan (200 mg, 1.0 mmol) were dissolved in 20 mL of fresh ethyl acetate. The reaction mixture was stirring for 5 h at room temperature. By monitoring the TLC, reaction was stopped. The crude mixture was concentrated and subjected to alumina column chromatographic (eluent ethyl acetate and n-hexane in 1:1(v/v)) purification to result pure oil compound L (158mg, 41%) after evaporation of the solvent.

^{1}H NMR (400 MHz, $CDCl_3$), δ (ppm): 8.57 (2H, d, J = 4.4 Hz, ArH); 8.38 (1H, J = 8.8 Hz, ArH); 7.70 (2H, td, J = 8.0 Hz, ArH); 7.33 (2H, d, J = 8.0 Hz, ArH); 7.27–7.23 (2H, m, ArH); 6.35 (1H, d, J = 9.2 Hz, ArH); 5.44 (4H, s, CH_2). ^{13}C NMR (100 MHz, $CDCl_3$), δ (ppm): 155, 149, 145, 144, 144, 137, 135, 123, 121, 103 and 58. ESI-MS (m/z) calculated for $C_{18}H_{14}N_6O_3$: 362.1, observed: 385.0 [L + Na^+].

Synthesis of $[MnL(CO)_3](CF_3SO_3)$, CORM-NBD.

In the dark and under a nitrogen atmosphere, $Mn(CO)_5Br$ (123 mg, 0.414 mmol) and silver triflate (106 mg, 0.414 mmol) were dissolved in 18 mL of dry acetone. The reaction mixture was stirred at 60 °C for 1.5 h. The reaction mixture was filtered under an inert atmosphere to separate the precipitate of silver bromide. To the filtrate, ligand L (150 mg, 0.414 mmol) in 10 mL of dry and deoxygenated acetone was added and the reaction mixture was heated under reflux for 60 °C for 1.5 h. The reaction mixture was filtered off and washed with dry diethyl ether several times to get pure CORM-NBD as in dark red solid (161mg, 60%). Slow diffusion of ether into a $CHCl_3$ solution of CORM-NBD afforded orange red plate-like crystals suitable for X-ray studies.

^{1}H NMR (400 MHz, CD_3CN), δ (ppm)]: 8.98 (2H, d, J = 5.6 Hz, ArH); 8.71 (1H, d, J = 8.0 Hz, ArH); 8.08 (2H, t, J = 7.66 Hz, ArH); 7.81 (1H, d, J = 8.0 Hz, ArH); 7.61 (4H, t, J = 4.8 Hz, ArH); 5.61 (2H, d, J = 16.8 Hz, -CH_2); 4.90 (2H, d, J = 16.8 Hz, -CH_2). ^{13}C-NMR (100 MHz, CD_3CN), δ (ppm): 159, 152, 146, 146, 144, 140, 132, 126, 123, 115 and 66. ESI-MS (m/z) $C_{22}H_{17}F_3MnN_6O_9S$, calculated for 649.99, observed: 501.0 [(CORM-NBD)-$^{-}OSO_2CF_3$].

IR: $(ATR)_v$ = 2042 cm^{-1}, 1956 cm^{-1} and 1933 cm^{-1} (ν_{CO} stretchings). Elemental analysis $C_{30}H_{26}F_3MnN_6O_8S_2$, calculated for C = 40.63%, H = 2.17 %, F = 8.76%, Mn = 8.45%, N =

12.92%, O = 22.14%, S = 21.51%, found: C = 40.32%, H = 2.25%, N = 12.35%, S = 4.41%.

Crystal Data for CORM-NBD:

$C_{22}H_{14}F_3MnN_6O_9S$ [*], Mr = 650.39 g mol^{-1} [*], yellow prism, size 0.088 × 0.082 × 0.068 mm^3, monoclinic, space group C2/c, a = 24.7020(5), b = 14.8232(3), c = 15.4917(3) Å, β = 118.287(1)°, V = 4995.10(17) $Å^3$, T= −140 °C, Z = 8, $\rho_{calcd.}$ = 1.730 g cm^{-3}, μ (Mo-K_α) = 7.01 cm^{-1}, multi-scan, transmin: 0.7099, transmax: 0.7456, F(000) = 2624, 16444 reflections in h(-32/31), k(−19/18), l(−17/20), measured in the range 2.51° ≤ Θ ≤ 27.45°, completeness Θ_{max} = 98.8%, 5646 independent reflections, R_{int} = 0.0483, 4779 reflections with $F_o > 4\sigma(F_o)$, 435 parameters, 0 restraints, $R1_{obs}$ = 0.0416, wR^2_{obs} = 0.0792, $R1_{all}$ = 0.0527, wR^2_{all} = 0.0849, GOOF = 1.074, largest difference peak and hole: 0.391 / −0.366 e $Å^{-3}$.

7. Summary

In this present work, a collection of transition metal based nitric oxide releasing molecules (NORM) and carbon monoxide releasing molecules (CORM) are introduced. The first chapter focuses on a series of ruthenium complexes with fluorinated carboxamide ligands $\{Ru\text{-}NO\}^6$. This conjugation ligand promoted NO liberation and improved residues stability after irradiation. Substituted fluorine ions worked as withdrawing functional group to influence the electron density of π-electrons. The two together contributed to improve the photolysis of NO from Ru(6-Fbpb)(NO)Cl, in which substitution of fluorine occurred at the ortho position of the aromatic ring. Different photochemical activities of NORMs upon low intensity irradiation were performed by a fluorescence assay with the presence of dye NO_{550}. DFT and TD-DFT calculations were given to describe the conjugation of ruthenium nitrosyls and investigate the NO release mechanism.

In the second part of work, a similar series of ruthenium-based CO releasing molecules with identical ligands of ruthenium nitrosyls were synthesized. Ortho-substituted compound, Ru(6-bpb)(CO)(H_2O) demonstrated high stability under aerobic conditions as well as in solution environment. It released CO upon illumination with low intensity light at 405 nm with detectable ^{19}F NMR characteristic signal change. DFT calculations confirmed the photolysis of CO from Ru(6-bpb)(CO)(H_2O) started from the admixture of d orbitals of metal center and antibonding π orbitals of ligands.

The third section described a stable and water-soluble manganese-based tricarbonyl complex with a fluorobenzenesulfonyl group. This CORM-FBS was found to rapidly release almost all three CO molecules upon illumination with low intensity light monitored by time-dependent liquid IR spectroscopy. DFT and TD-DFT calculations gave insight into the CO release mechanism and the properties of the inactive photo-product. For the first time, ^{19}F NMR was performed to monitor the photoreaction process of CORM-FBS under irradiation. The comparison of characteristic spectra revealed that one CO ligand was firstly photochemically dissociated and replaced by solvent molecule with remaining residues for further CO release by oxidation reaction.

Then, a stable and water-soluble CORM-Dabsyl that released three CO molecules upon photolysis with an obviously visible colorimetric response was synthesized. DFT and TD-DFT calculations were performed to investigate the CO release mechanism, contribution of dabsyl ligand and the properties of the photo-product iCORM-Dabsyl. Furthermore, paper strips which loaded CORM-Dabsyl that acted as a CO-releasing material for convenient and efficient CO-release under illumination were the first time fabricated. This process was recorded by a portable CO sensor (Dräger Pac7000) and its strong colorimetric response offered a direct visible estimation of CO release.

The last chapter presented a colorimetric as well as fluorometric dual response CORM-NBD that released all three CO molecules upon photolysis at low energy light. The easily observed colorimetric response also provided a directly visible estimation of CO release by the naked eye. The turn-on luminescence made it possible to track the CO delivery within the cells from the cellular imaging experiments on LX-2 cells and HepaRG® cells. DFT and TD-DFT calculations were studied to investigate the CO release mechanism. Moreover, TLC plate sticks that loaded CORM-NBD achieved to release CO immediately upon irradiation with strong colorimetric response.

In summary, the introduction of electron withdrawing groups and colorimetric groups aimed at improving the NO and CO releasing properties and render the light-triggered NORMs and CORMs applicable to medical situations where exogenous nitric oxide and carbon monoxide gas molecules are needed as drugs. These modifications are highly useful for to achieve precise spatial and temporal control over gas releasing as well as to monitor the photo-reaction process. Moreover, cell studies further confirmed the practicability of potential therapeutic agent in biological systems. It is reasonable to believe that the synthesis of these photo-NORMs and -CORMs is one giant step for the next generation of NO and CO releasing molecules and materials.

8. Zusammenfassung

In der vorliegenden Arbeit wird eine Sammlung von übergangsmetallbasierten, Stickstoffmonoxidfreisetzenden- (NORM) und Kohlenstoffmonoxidfreisetzenden (CORM) Molekülen vorgestellt.

Das erste Kapitel handelt von Ruthenium-Komplexen mit fluorinierten Carboxamid-Liganden {Ru-NO}6. Diese konjugierten Liganden fördern die NO-Freisetzung durch Lichtbestrahlung und verbessern die Stabilität des Komplexes nach der Bestrahlung. Durch die Substitution mit Fluor am Carboxamid-Liganden erhöht sich der Einfluss auf die Elektronendichte des Moleküls, da Fluor eine elektronenziehende Wirkung auf das π-System hat. Die zwei zusammen trugen dazu bei, die Photolyse von NO aus Ru(6-Fbpb)(NO)Cl zu verbessern, bei der die Substitution von Fluor an der ortho-Position des aromatischen Rings erfolgte. Verschiedene photochemische Aktivitäten der NORMs bei Bestrahlung mit geringer Intensität wurden durch einen Fluoreszenztest mit dem Farbstoff NO550 durchgeführt. DFT- und TD-DFT-Rechnungen wurden zur Beschreibung der Konjugation von Rutheniumnitrosylen und zur Untersuchung des NO-Freisetzungsmechanismus durchgeführt.

Im zweiten Teil der Dissertation geht es ebenfalls um Ruthenium-Carboxamid-Komplexe, diesmal jedoch mit einem Kohlenstoffdioxid-Liganden statt einem Nitrosyl-Liganden. Der ortho-substituierte Komplex, Ru(6-bpb)(CO)(H2O), zeigt eine hohe Stabilität unter aeroben Bedingungen sowie in einer Lösungsumgebung. Durch die Bestrahlung mit Licht geringer Intensität bei 405 nm wird CO freigesetzt und eine mit 19F-NMR detektierbare Signaländerung kann gemessen werden. DFT-Rechnungen bestätigten die Photolyse von CO aus Ru(6-bpb)(CO)(H2O), die aus der Überlappung von d-Orbitalen des Metallzentrums und der antibindenden π-Orbitale des Liganden resultieren.

Der dritte Abschnitt beschreibt einen stabilen und wasserlöslichen Tricarbonylkomplex auf Manganbasis mit einer Fluorbenzolsulfonylgruppe (FBS). Es wurde festgestellt, dass dieses CORM-FBS bei Bestrahlung mit Licht niedriger Intensität alle drei CO-Moleküle fast zeitgleich freisetzt. Überwacht wurde diese Freisetzung durch zeitabhängige, flüssige IR-Spektroskopie.

DFT- und TD-DFT-Rechnungen lieferten Einblicke in den CO-Freisetzungsmechanismus und die Eigenschaften des inaktiven Fotoprodukts. Zum ersten Mal wurde 19F-NMR zur Überwachung des Photoreaktionsprozesses eines CORM-FBS eingesetzt. Der Vergleich der charakteristischen Spektren ergab, dass ein CO-Ligand zuerst photochemisch dissoziiert und durch ein Lösungsmittelmolekül ersetzt wurde. Weitere CO-Freisetzungen erfolgen durch Oxidationsreaktionen.

Dann wurde ein stabiles und wasserlösliches CORM-Dabsyl synthetisiert, dass bei der Photolyse drei CO-Moleküle mit einer sichtbaren kolorimetrischen Reaktion freisetzte. DFT- und TD-DFT-Rechnungen wurden durchgeführt, um den CO-Freisetzungsmechanismus, den Beitrag des Dabsyl-Liganden und die Eigenschaften des Fotoprodukts iCORM-Dabsyl zu untersuchen. Darüber hinaus wurden das erste mal Papierstreifen mit CORM-Dabsyl als CO-freisetzendes Material beladen, um eine bequeme und effiziente CO-Freisetzung durch Beleuchtung zu ermöglichen. Dieser Prozess wurde mit Hilfe eines tragbaren CO-Sensors (Dräger Pac7000) begleitet und aufgezeichnet und seine starke kolorimetrische Reaktion bot eine direkte sichtbare Abschätzung der CO-Freisetzung.

Das letzte Kapitel zeigt eine Kombination aus kolorimetrischen und fluorimetrischen Reaktionen, CORM-NBD, welches alle drei CO-Moleküle bei der Photolyse mit energiearmen Licht freisetzte. Die leicht zu beobachtende kolorimetrische Reaktion lieferte auch eine direkte sichtbare Abschätzung der CO-Freisetzung mit bloßem Auge. Die einschaltbare Lumineszenz ermöglichte die Verfolgung der CO-Abgabe innerhalb der Zellen aus den zellulären Bildgebungsexperimenten an LX-2-Zellen und HepaRG®-Zellen. Mit Hilfe von DFT- und TD-DFT-Rechnungen wurde versucht den CO-Freisetzungsmechanismus zu untersuchen. Darüber hinaus wurden DC-Platten mit CORM-NBD geladen, um unmittelbar nach der Bestrahlung CO freizusetzen und eine starke kolorimetrische Rückmeldung zu erhalten.

Zusammengefasst, die Einführung von elektronenziehenden und kolorimetrischen Gruppen verbessert die NO- und CO-freisetzenden Eigenschaften und macht die lichtgesteuerten NORMs und CORMs für medizinische Anwendungen einsetzbar, in denen exogene Stickstoffmonoxid- und Kohlenstoffmonoxid-Gasmoleküle als Arzneimittel benötigt werden. Diese Modifikationen sind sehr nützlich, um eine präzise räumliche und zeitliche Steuerung der Gasfreisetzung zu

erreichen und den Fotoreaktionsprozess zu überwachen. Darüber hinaus bestätigten Zellstudien die Praktikabilität potentieller Therapeutika in biologischen Systemen. Es ist anzunehmen, dass die Synthese dieser Photo-NORMs und -CORMs ein großer Schritt für eine nächste Generation von NO- und CO-freisetzenden Molekülen und Materialien ist.

9. References

[1] G. Farrugia, J. H. Szurszewski, *Gastroenterology* **2014**, *147*, 303–313.

[2] D. Koshland, *Science (80-.).* **1992**, *258*, 1861.

[3] C. Szabõ, *Nat. Rev. Drug Discov.* **2007**, *6*, 917–935.

[4] S. H. C. Askes, G. U. Reddy, R. Wyrwa, S. Bonnet, A. Schiller, *J. Am. Chem. Soc.* **2017**, *139*, 15292–15295.

[5] D. T. Mason, E. Braunwald, *Circulation* **1965**, *32*, 755–766.

[6] N. C. Gilbert, *J. Am. Med. Assoc.* **1952**, *148*, 1372–1376.

[7] R. Berlin, *Drugs* **1987**, *33*, 1–4.

[8] T. Lauder. Brunton, *Lectures on the Action of Medicines; Being the Course of Lectures on Pharmacology and Therapeutics Delivered at St. Bartholomew's Hospital during the Summer Session 1896*, New York ; The Macmillan Company, **1998**.

[9] M. F. Katsuki S, Arnold W, Mittal C, *J. Cyclic Nucleotide Res.* **1977**, *3*, 23–25.

[10] R. M. Palmer, A. G. Ferrige, S. Moncada, *Nature* **1987**, *327*, 524–526.

[11] R. F. Furchgott, *Biosci. Rep.* **1999**, *19*, 235–251.

[12] R. F. Furchgott, J. V. Zawadzki, *Nature* **1980**, *288*, 373–376.

[13] L. J. Ignarro, G. M. Buga, K. S. Wood, R. E. Byrns, G. Chaudhurit, C. H. Sawyer, *Med. Sci.* **1987**, *84*, 9265–9269.

[14] L. J. Ignarro, R. E. Byrns, G. M. Buga, K. S. Wood, *Circ. Res.* **1987**, *61*, 866–879.

[15] J. E. Albina, J. S. Reichner, *Cancer Metastasis Rev.* **1998**, *17*, 39–53.

[16] S. Moncada, a. Higgs, R. Furchgott, *Pharmacol. Rev.* **1997**, *49*, 137–142.

[17] S. Mocellin, V. Bronte, D. Nitti, *Med. Res. Rev.* **2007**, *27*, 317–352.

[18] D. Hirst, T. Robson, *J. Pharm. Pharmacol.* **2007**, *59*, 3–13.

[19] E. A. H. S. Moncada, R. M. J. Palmer, *Pharmacol. Rev.* **1991**, *43*, 109–134.

[20] A. G. Tennyson, S. J. Lippard, *Chem. Biol.* **2011**, *18*, 1211–1220.

[21] H. Li, J. Igarashi, J. Jamal, W. Yang, T. L. Poulos, *J. Biol. Inorg. Chem.* **2006**, *11*, 753–768.

[22] P. Vallance, J. Leiper, *Nat. Rev. Drug Discov.* **2002**, *1*, 939–950.

[23] K. A. Hanafy, J. S. Krumenacker, F. Murad, *Med. Sci. Monit.* **2001**, *7*, 801–819.

[24] M. K. O. Grant, E. E. El-Fakahany, *Life Sci.* **2004**, *74*, 1701–1721.

[25] B. S. S. Masters, K. McMillan, A. Sheta, J. S. Nishimura, J. Roman, P. Martasek, *Faseb J.* **1996**, *10*, 552–558.

[26] B. G. Hill, B. P. Dranka, S. M. Bailey, J. R. Lancaster, V. M. Darley-Usmar, *J. Biol. Chem.* **2010**, *285*, 19699–19704.

[27] Owen W. Griffith, Dennis. J. Stuehr, *Annu. Rev. Physiol.* **1995**, *57*, 707–736.

[28] U. Förstermann, W. C. Sessa, *Eur. Heart J.* **2012**, *33*, 829–837.

[29] K. Pant, A. M. Bilwes, S. Adak, D. J. Stuehr, B. R. Crane, *Biochemistry* **2002**, *41*, 11071–11079.

[30] W. K. Alderton, C. E. Cooper, R. G. Knowles, *Biochem. J.* **2001**, *357*, 593–615.

[31] D. J. Stuehr, *J. Nutr.* **2004**, *134*, 2748–2751.

[32] D. J. Stuehr, J. Santolini, Z. Q. Wang, C. C. Wei, S. Adak, *J. Biol. Chem.* **2004**, *279*, 36167–36170.

[33] P. G. Wang, M. Xian, X. Tang, X. Wu, Z. Wen, T. Cai, A. J. Janczuk, *Chem. Rev.* **2002**, *102*, 1091–1134.

[34] S. Moncada, E. A. Higgs, *Br. J. Pharmacol.* **2006**, *147*, S193–S201.

[35] P. George, T. B. Cai, *Nitric Oxide Donors: For Pharmaceutical and Biological Applications*, Wiley-Vch Verlag GmbH & Co. KGaA, **2005**.

[36] J. C. Toledo, O. Augusto, *Chem. Res. Toxicol.* **2012**, *25*, 975–989.

[37] D. A. Wink, I. Hanbauer, M. B. Grisham, F. Laval, R. W. Nims, J. Laval, J. Cook, R. Pacelli, J. Liebmann, M. Krishna, et al., *Curr. Top. Cell. Regul.* **1996**, *34*, 159–187.

[38] D. A. Wink, J. B. Mitchell, *Free Radic. Biol. Med.* **1998**, *25*, 434–456.

[39] P. C. F. David A.Wink, Matthew B.Grisham, James B.Mitchell, *Methods Enzymol.* **1996**, *268*, 12–31.

[40] R. G. Knowles, M. Palacios, R. M. Palmer, S. Moncada, *Proc. Natl. Acad. Sci. U. S. A.* **1989**, *86*, 5159–5162.

[41] A. J. Gomes, E. M. Espreafico, E. Tfouni, *J. Inorg. Biochem.* **2008**, *102*, 757–766.

[42] C. N. Louis J. Ignarro, Giuseppe Cirino, Alessandro Casini, *J. Cardiovasc. Pharmacol.* **1999**, *34*, 879–886.

[43] D. Fukumura, S. Kashiwagi, R. K. Jain, *Nat. Rev. Cancer* **2006**, *6*, 521–534.

[44] R. W. N. david A. Wink, Yoichi Osawa, John F. Darbyshire, Collins R. Jones, Steven C. Eshenaur, *Arch. Biochem. Biophys.* **1993**, *300*, 115–123.

[45] P. R. O. de M. Hugues Ouellet, Jérôme Lang,§ Manon Couture, *Biochemistry* **2009**, *48*, 863–872.

[46] J. J. Davis, in *Eng. Bioelectron. Interface Appl. to Anal. Biosensing Protein Detect.*, Royal Society Of Chemistry, **2009**.

[47] M. N. Möller, Q. Li, D. A. Vitturi, J. M. Robinson, J. R. Lancaster, A. Denicola, *Chem. Res. Toxicol.* **2007**, *20*, 709–714.

[48] J. A. McCleverty, *Chem. Rev.* **1979**, *79*, 53–76.

[49] C. Szabó, H. Ischiropoulos, R. Radi, *Nat. Rev. Drug Discov.* **2007**, *6*, 662–680.

[50] X. Chen, F. Wang, J. Y. Hyun, T. Wei, J. Qiang, X. Ren, I. Shin, J. Yoon, *Chem. Soc. Rev.* **2016**, *45*, 2976–3016.

[51] S. K. Sharma, A. W. Schaefer, H. Lim, H. Matsumura, P. Moënne-Loccoz, B. Hedman, K. O. Hodgson, E. I. Solomon, K. D. Karlin, *J. Am. Chem. Soc.* **2017**, *139*, 17421–17430.

[52] S. V. Lymar, J. K. Hurst, *J. Am. Chem. Soc.* **1995**, *117*, 8867–8868.

[53] P. C. Ford, I. M. Lorkovic, *Chem. Rev.* **2002**, *102*, 993–1017.

[54] A. R. Butler, I. L. Megson, *Chem. Rev.* **2002**, *102*, 1155–1165.

[55] M. Lewin, K. Fisher, I. Dance, *Chem. Commun.* **2000**, *4*, 947–948.

[56] J. A. McCleverty, *Chem. Rev.* **2004**, *104*, 403–418.

[57] P. C. Ford, *Acc. Chem. Res.* **2008**, *41*, 190–200.

[58] R. Eisenberg, C. D. Meyer, *Acc. Chem. Res.* **1975**, *8*, 26–34.

[59] M. Hoshino, L. Laverman, P. C. Ford, *Coord. Chem. Rev.* **1999**, *187*, 75–102.

[60] J. H. Enemark, R. D. Feltham, *J. Am. Chem. Soc.* **1974**, *96*, 5002–5004.

[61] N. Reginato, C. T. C. McCrory, D. Pervitsky, L. Li, *J. Am. Chem. Soc.* **1999**, *121*, 10217–10218.

[62] J. H. Enemark, *Coord. Chem. Rev.* **1974**, *13*, 339–406.

[63] N. L. Fry, P. K. Mascharak, *Dalt. Trans.* **2012**, *41*, 4726.

[64] R. Hoffmann, M. M. L. Chen, M. Elian, *Inorg. Chem.* **1974**, *13*, 2666–2675.

[65] G. B. Richter-Addo, R. A. Wheeler, C. A. Hixson, L. Chen, M. A. Khan, M. K. Ellison, C. E. Schulz, W. R. Scheidt, *J. Am. Chem. Soc.* **2001**, *123*, 6314–6326.

[66] M. Wolak, R. Van Eldik, *Coord. Chem. Rev.* **2002**, *230*, 263–282.

[67] M. D. Carducci, M. R. Pressprich, P. Coppens, *J. Am. Chem. Soc.* **1997**, *119*, 2669–2678.

[68] F. Roncaroli, M. Videla, L. D. Slep, J. A. Olabe, *Coord. Chem. Rev.* **2007**, *251*, 1903–1930.

[69] Lyon Playfair, *Annalen* **1850**, *74*, 317–320.

[70] Johnson C. C., *Arch. Int. Pharmacodyn. Ther.* **1929**, *35*, 480–496.

[71] P. T. Manoharan, W. C. Hamilton, *Inorg. Chem.* **1963**, *2*, 1043–1047.

[72] A. R. Butler, C. Glidewell, *Chem. Soc. Rev.* **1987**, *16*, 361–380.

[73] U. Hauser, V. Oestreich, H. D. Rohrweck, P. Institut, U. Kn, **1977**, *25*, 17–25.

[74] H. Zöllner, W. Krasser, T. Woike, S. Haussühl, *Chem. Phys. Lett.* **1989**, *161*, 497–501.

[75] L. Grossi, S. D'Angelo, *J. Med. Chem.* **2005**, *48*, 2622–2626.

[76] A. R. Butler, *J. Chem. Educ.* **1982**, *59*, 549.

[77] L. Chen, Q. He, M. Lei, L. Xiong, K. Shi, L. Tan, Z. Jin, T. Wang, Z. Qian, *ACS Appl. Mater. Interfaces* **2017**, *9*, 36473–36477.

[78] Roussin, *Ann. Chim. Phys.* **1958**, *52*, 285–303.

[79] P. C. Ford, J. Bourassa, K. Miranda, B. Lee, I. Lorkovic, S. Boggs, S. Kudo, L. Laverman, *Coord. Chem. Rev.* **1998**, *171*, 185–202.

[80] J. Bourassa, W. DeGraff, S. Kudo, D. A. Wink, J. B. Mitchell, P. C. Ford, *J. Am. Chem. Soc.* **1997**, *119*, 2853–2860.

[81] F. W. Flitney, I. L. Megson, D. E. Flitney, A. R. Butler, *Br. J. Pharmacol.* **1992**, *107*, 842–848.

[82] A. D. Ostrowski, P. C. Ford, *Dalt. Trans.* **2009**, 10660–10669.

[83] K. H. Hopmann, J. Conradie, A. Ghosh, *J. Phys. Chem. B* **2009**, *113*, 10540–10547.

[84] M. B. Sárosi, L. Silaghi-Dumitrescu, R. B. King, *Phys. Chem. Chem. Phys.* **2012**, *14*, 5998–6002.

[85] F. Aquilante, J. Autschbach, R. K. Carlson, L. F. Chibotaru, M. G. Delcey, L. De Vico, I. Fdez. Galván, N. Ferré, L. M. Frutos, L. Gagliardi, et al., *J. Comput. Chem.* **2016**, *37*, 506–541.

[86] M. Jaworska, Z. Stasicka, *New J. Chem.* **2005**, *29*, 604–612.

[87] N. L. Anna C. Merkle, Ashley B. McQuarters, *Dalt. Trans.* **2012**, *41*, 8047–8059.

[88] G. K. Helmkamp, D. C. Owsley, W. M. Barnes, H. N. Cassey, *J. Am. Chem. Soc.* **1968**, *90*, 1635–1638.

[89] E. M. Arnett, T. C. Moriarity, L. E. Small, J. P. Rudolph, R. P. Quirk, *J. Am. Chem. Soc.* **1973**, *95*, 1492–1495.

[90] P. C. Ford, L. E. Laverman, *Coord. Chem. Rev.* **2005**, *249*, 391–403.

[91] M. J. Rose, P. K. Mascharak, *Chem. Commun.* **2008**, 3933–3935.

[92] N. L. Fry, J. Wei, P. K. Mascharak, *Inorg. Chem.* **2011**, *50*, 9045–9052.

[93] N. L. Fry, B. J. Heilman, P. K. Mascharak, *Inorg. Chem.* **2011**, *50*, 317–324.

[94] J. T. Mitchell-Koch, T. M. Reed, A. S. Borovik, *Angew. Chemie - Int. Ed.* **2004**, *43*, 2806–2809.

[95] J. Bordini, P. C. Ford, E. Tfouni, *Chem. Commun.* **2005**, 4169–4171.

[96] N. L. Fry, P. K. Mascharak, *Acc. Chem. Res.* **2011**, *44*, 289–298.

[97] J. C. Toledo, H. A. S. Silva, M. Scarpellini, V. Mori, A. J. Camargo, M. Bertotti, D. W. Franco, *Eur. J. Inorg. Chem.* **2004**, 1879–1885.

[98] C. Kim, I. Novozhilova, M. S. Goodman, K. A. Bagley, P. Coppens, *Inorg. Chem.* **2000**, *39*, 5791–5795.

[99] F. Marquele-Oliveira, D. C. de Almeida Santana, S. F. Taveira, D. M. Vermeulen, A. R. Moraes de Oliveira, R. S. da Silva, R. F. V. Lopez, *J. Pharm. Biomed. Anal.* **2010**, *53*, 843–851.

[100] J. Wang, F. Yang, Y. Zhao, P. Yu, X. Qiao, J. Wang, H. Wang, *Phys. Chem. Chem. Phys.* **2014**, *16*, 24045–24054.

[101] T. C. Harrop, M. M. Olmstead, P. K. Mascharak, *Inorg. Chem.* **2005**, *44*, 6918–6920.

[102] D. V. Fomitchev, T. R. Furlani, P. Coppens, *Inorg. Chem.* **1998**, *37*, 1519–1526.

[103] A. D. Ostrowski, S. J. Deakin, B. Azhar, T. W. Miller, N. Franco, M. M. Cherney, A. J. Lee, J. N. Burstyn, J. M. Fukuto, I. L. Megson, et al., *J. Med. Chem.* **2010**, *53*, 715–722.

[104] A. A. Eroy-Reveles, Y. Leung, P. K. Mascharak, *J. Am. Chem. Soc.* **2006**, *128*, 7166–7167.

[105] J. R. Michael, M. B. Nolan, G. O. Allen, P. K. Mascharak, *Inorg. Chem.* **2010**, *49*, 1854–1864.

[106] N. Levin, N. O. Codesido, E. Bill, T. Weyhermüller, A. P. Segantin Gaspari, R. S. Da Silva, J. A. Olabe, L. D. Slep, *Inorg. Chem.* **2016**, *55*, 7808–7810.

[107] R. K. Afshar, A. A. Eroy-Reveles, M. M. Olmstead, P. K. Mascharak, *Inorg. Chem.* **2006**, *45*, 10347–10354.

[108] L. Cheng, I. Novozhilova, C. Kim, A. Kovalevsky, K. A. Bagley, P. Coppens, G. B. Richter-Addo, *J. Am. Chem. Soc.* **2000**, *122*, 7142–7143.

[109] J. J. Yan, M. A. Gonzales, P. K. Mascharak, B. Hedman, K. O. Hodgson, E. I. Solomon, *J. Am. Chem. Soc.* **2017**, *139*, 1215–1225.

[110] C. Gianna Hoffman-Luca, A. A. Eroy-Reveles, J. Alvarenga, P. K. Mascharak, *Inorg. Chem.* **2009**, *48*, 9104–9111.

[111] K. Ghosh, A. A. Eroy-Reveles, B. Avila, T. R. Holman, M. M. Olmstead, P. K. Mascharak, *Inorg. Chem.* **2004**, *43*, 2988–2997.

[112] B. J. Heilman, J. St. John, S. R. J. Oliver, P. K. Mascharak, *J. Am. Chem. Soc.* **2012**, *134*, 11573–11582.

[113] A. C. Merkle, N. L. Fry, P. K. Mascharak, N. Lehnert, *Inorg. Chem.* **2011**, *50*, 12192–12203.

[114] G. M. Halpenny, K. R. Gandhi, P. K. Mascharak, *ACS Med. Chem. Lett.* **2010**, *1*, 180–183.

[115] A. A. Eroy-Reveles, P. K. Mascharak, *Future Med. Chem.* **2009**, *1*, 1497–1507.

[116] K. A. Mowery, M. H. Schoenfisch, J. E. Saavedra, L. K. Keefer, M. E. Meyerhoff, *Biomaterials* **2000**, *21*, 9–21.

[117] D. A. Riccio, P. N. Coneski, S. P. Nichols, A. D. Broadnax, M. H. Schoenfisch, *ACS Appl. Mater. Interfaces* **2012**, *4*, 796–804.

[118] E. Deniz, N. Kandoth, A. Fraix, V. Cardile, A. C. E. Graziano, D. Lo Furno, R. Gref, F. M. Raymo, S. Sortino, *Chem. - A Eur. J.* **2012**, *18*, 15782–15787.

[119] D. S. Marlin, P. K. Mascharak, *Chem. Soc. Rev.* **2000**, *29*, 69–74.

[120] D. Neuman, A. D. Ostrowski, R. O. Absalonson, G. F. Strouse, P. C. Ford, *J. Am. Chem. Soc.* **2007**, *129*, 4146–4147.

[121] P. D. Marcato, L. F. Adami, R. De Melo, P. S. Melo, R. Iasmin, L. De Paula, N. Durán, A. B. Seabra, *Curr. Nanosci.* **2013**, *9*, 1–7.

[122] R. Weissleder, V. Ntziachristos, *Nat. Med.* **2003**, *9*, 123–128.

[123] R. Weissleder, *Nat. Biotechnol.* **2001**, *19*, 316–317.

[124] Y. Hitomi, Y. Iwamoto, M. Kodera, *Dalt. Trans.* **2014**, *43*, 2161–2167.

[125] J. D. Mase, A. O. Razgoniaev, M. K. Tschirhart, A. D. Ostrowski, *Photochem. Photobiol. Sci.* **2015**, *14*, 775–785.

[126] D. Neumann, A. D. Ostrowski, A. A. Mikhailovsky, R. O. Absalonson, G. F. Strouse, P. C. Ford, *J. Am. Chem. Soc.* **2008**, *130*, 168–175.

[127] G. M. Halpenny, M. M. Olmstead, P. K. Mascharak, *Inorg. Chem.* **2007**, *46*, 6601–6606.

[128] C. Bohlender, K. Landfester, D. Crespy, A. Schiller, *Part. Part. Syst. Charact.* **2013**, *30*, 138–142.

[129] E. Tfouni, F. G. Doro, A. J. Gomes, R. S. da Silva, G. Metzker, P. G. Z. Benini, D. W. Franco,

Coord. Chem. Rev. **2010**, *254*, 355–371.

[130] D. Crespy, K. Landfester, U. S. Schubert, A. Schiller, *Chem. Commun.* **2010**, *46*, 6651.

[131] C. Bohlender, M. Wolfram, H. Goerls, W. Imhof, R. Menzel, A. Baumgaertel, U. S. Schubert, U. Mueller, M. Frigge, M. Schnabelrauch, et al., *J. Mater. Chem.* **2012**, *22*, 8785–8792.

[132] R. Motterlini, L. E. Otterbein, *Nat. Rev. Drug Discov.* **2010**, *9*, 728–743.

[133] P. Horcajada, R. Gref, T. Baati, P. K. Allan, G. Maurin, P. Couvreur, G. Férey, R. E. Morris, C. Serre, *Chem. Rev.* **2012**, *112*, 1232–1268.

[134] K. Ling, F. Men, W.-C. Wang, Y.-Q. Zhou, H.-W. Zhang, D.-W. Ye, *J. Med. Chem.* **2017**, *61*, 2611–2635.

[135] S. D. G. B. V. D. M. Maurice Stupfel M. D., *Ann. N. Y. Acad. Sci.* **1970**, *174*, 342–368.

[136] L. E. Otterbein, F. H. Bach, J. Alam, M. Soares, H. Tao Lu, M. Wysk, R. J. Davis, R. A. Flavell, A. M. K. Choi, *Nat. Med.* **2000**, *6*, 422–428.

[137] T. R. Johnson, B. E. Mann, J. E. Clark, R. Foresti, C. J. Green, R. Motterlini, *Angew. Chemie Int. Ed.* **2003**, *42*, 3722–3729.

[138] K. Sato, J. Balla, L. Otterbein, R. N. Smith, S. Brouard, Y. Lin, E. Csizmadia, J. Sevigny, S. C. Robson, G. Vercellotti, et al., *J. Immunol.* **2001**, *166*, 4185–4194.

[139] L. Günther, P. O. Berberat, M. Haga, S. Brouard, R. Neal Smith, M. P. Soares, F. H. Bach, E. Tobiasch, *Diabetes* **2002**, *51*, 994–999.

[140] S. W. Ryter, J. Alam, A. M. K. Choi, *Physiol Rev* **2006**, *86*, 583–650.

[141] L. Li, A. Hsu, P. K. Moore, *Pharmacol. Ther.* **2009**, *123*, 386–400.

[142] S. W. Ryter, L. E. Otterbein, *BioEssays* **2004**, *26*, 270–280.

[143] W. a Catterall, A. L. Goldin, S. G. Waxman, *Pharmacol. Rev.* **2005**, *57*, 397–409.

[144] S. F. Medical, X. Francisco, **1969**, *244*, 1255–1259.

[145] B. E. Mann, R. Motterlini, *Chem. Commun. (Camb)* **2007**, 4197–4208.

[146] H. P. Kim, S. W. Ryter, A. M. K. Choi, *Annu. Rev. Pharmacol. Toxicol.* **2006**, *46*, 411–449.

[147] H. Inaba, K. Fujita, T. Ueno, *Biomater. Sci.* **2015**, *3*, 1423–1438.

[148] B. Olas, *Chem. Biol. Interact.* **2014**, *222*, 37–43.

[149] S. W. Ryter, L. E. Otterbein, D. Morse, A. M. K. Choi, *Mol. Cell. Biochem.* **2002**, *234–235*, 249–263.

[150] R. Alberto, R. Motterlini, *Dalt. Trans.* **2007**, 1651–1660.

[151] C. Peers, D. S. Steele, *J. Mol. Cell. Cardiol.* **2012**, *52*, 359–365.

[152] L. Wu, *Pharmacol. Rev.* **2005**, *57*, 585–630.

[153] R. Motterlini, R. Foresti, *Am. J. Physiol. Cell Physiol.* **2017**, *312*, C302–C313.

[154] T. L. Poulos, *Curr. Opin. Struct. Biol.* **2006**, *16*, 736–743.

[155] X. Ma, N. Sayed, A. Beuve, F. Van Den Akker, *EMBO J.* **2007**, *26*, 578–588.

[156] G. D'Amico, *J. Cell Sci.* **2006**, *119*, 2291–2298.

[157] W. J. Wilkinson, P. J. Kemp, *J. Physiol.* **2011**, *589*, 3055–3062.

[158] J. L. Scragg, M. L. Dallas, J. A. Wilkinson, G. Varadi, C. Peers, *J. Biol. Chem.* **2008**, *283*, 24412–24419.

[159] C. Peers, M. L. Dallas, J. L. Scragg, *Commun. Integr. Biol.* **2009**, *2*, 241–242.

[160] W. A. Catterall, *Cold Spring Harb. Perspect. Biol.* **2011**, *3*, 1–23.

[161] K. Charalambous, B. A. Wallace, *Biochemistry* **2011**, *50*, 6742–6752.

[162] C. Guardiani, O. A. Fedorenko, S. K. Roberts, I. A. Khovanov, *Phys. Chem. Chem. Phys.* **2017**, *19*, 29840–29854.

[163] J. L. Boer, S. B. Mulrooney, R. P. Hausinger, *Arch. Biochem. Biophys.* **2014**, *544*, 142–152.

[164] M. O. H. H. Jaffe, *Temhcdron* **1960**, *10*, 212–214.

[165] Y. Liu, B. Liu, Y. Liu, M. G. B. Drew, *J. Chem. Educ.* **2012**, *89*, 355–359.

[166] C. D. Zeinalipour-Yazdi, R. A. Van Santen, *J. Phys. Chem. C* **2012**, *116*, 8721–8730.

[167] G. Blyholder, *J. Phys. Chem.* **1964**, *68*, 2772–2777.

[168] G. Bistoni, S. Rampino, N. Scafuri, G. Ciancaleoni, D. Zuccaccia, L. Belpassi, F. Tarantelli, *Chem. Sci.* **2016**, *7*, 1174–1184.

[169] C. C. Romão, W. A. Blättler, J. D. Seixas, G. J. L. Bernardes, *Chem. Soc. Rev.* **2012**, *41*, 3571–3583.

[170] Z. Lam, K. V. Kong, M. Olivo, W. K. Leong, *Analyst* **2016**, *141*, 1569–1586.

[171] R. Motterlini, *Circ. Res.* **2002**, *90*, e17–e24.

[172] J. E. Clark, *Circ. Res.* **2003**, *93*, e2–e8.

[173] R. Motterlini, *FASEB J.* **2004**, *19*, 284–286.

[174] T. S. Pitchumony, B. Spingler, R. Motterlini, R. Alberto, *Org. Biomol. Chem.* **2010**, *8*, 4849–4854.

[175] J. D. Seixas, A. Mukhopadhyay, T. Santos-Silva, L. E. Otterbein, D. J. Gallo, S. S. Rodrigues, B. H. Guerreiro, A. M. L. Gonçalves, N. Penacho, A. R. Marques, et al., *Dalt. Trans.* **2013**, *42*, 5985–5998.

[176] S. Botov, E. Stamellou, S. Romanski, M. Guttentag, R. Alberto, J. M. Neudörfl, B. Yard, H. G. Schmalz, *Organometallics* **2013**, *32*, 3587–3594.

[177] N. S. Sitnikov, Y. Li, D. Zhang, B. Yard, H. G. Schmalz, *Angew. Chemie Int. Ed.* **2015**, *54*, 12314–12318.

[178] M. A. Gonzales, H. Han, A. Moyes, A. Radinos, A. J. Hobbs, N. Coombs, S. R. J. Oliver, P. K. Mascharak, *J. Mater. Chem. B* **2014**, *2*, 2107–2113.

[179] F. Zobi, O. Blacque, R. A. Jacobs, M. C. Schaub, A. Y. Bogdanova, *Dalt. Trans.* **2012**, *41*, 370–378.

[180] R. Dale Rimmer, H. Richter, P. C. Ford, *Inorg. Chem.* **2010**, *49*, 1180–1185.

[181] F. Zobi, A. Degonda, M. C. Schaub, A. Y. Bogdanova, *Inorg. Chem.* **2010**, *49*, 7313–7322.

[182] F. Zobi, *Future Med. Chem.* **2013**, *5*, 175–188.

[183] W. Q. Zhang, A. C. Whitwood, I. J. S. Fairlamb, J. M. Lynam, *Inorg. Chem.* **2010**, *49*, 8941–8952.

[184] S. E. McGlynn, D. W. Mulder, E. M. Shepard, J. B. Broderick, J. W. Peters, *Dalt. Trans.* **2009**, 4274–4298.

[185] J. Niesel, A. Pinto, H. W. Peindy N'Dongo, K. Merz, I. Ott, R. Gust, U. Schatzschneider, *Chem. Commun.* **2008**, 1798–1800.

[186] C. V. Siva Rama Rao, K. V. Rao, A. Raviprasad, C. Chiranjivi, *J. Chem. Eng. Data* **1978**, *23*, 23–25.

[187] C. Bischof, T. Joshi, A. Dimri, L. Spiccia, U. Schatzschneider, *Inorg. Chem.* **2013**, *52*, 9297–9308.

[188] R. Kretschmer, G. Gessner, H. Görls, S. H. Heinemann, M. Westerhausen, *J. Inorg. Biochem.* **2011**, *105*, 6–9.

[189] A. E. Pierri, A. Pallaoro, G. Wu, P. C. Ford, *J. Am. Chem. Soc.* **2012**, *134*, 18197–18200.

[190] S. J. Carrington, I. Chakraborty, P. K. Mascharak, *Chem. Commun.* **2013**, *49*, 11254.

[191] A. E. Pierri, P.-J. Huang, J. V. Garcia, J. G. Stanfill, M. Chui, G. Wu, N. Zheng, P. C. Ford, *Chem. Commun.* **2015**, *51*, 2072–2075.

[192] C. Bohlender, S. Gläser, M. Klein, J. Weisser, S. Thein, U. Neugebauer, J. Popp, R. Wyrwa, A. Schiller, *J. Mater. Chem. B* **2014**, *2*, 1454–1463.

[193] A. R. Rothrock, R. L. Donkers, M. H. Schoenfisch, *J. Am. Chem. Soc.* **2005**, *127*, 9362–9363.

[194] G. Dördelmann, T. Meinhardt, T. Sowik, A. Krueger, U. Schatzschneider, *Chem. Commun.* **2012**, *48*, 11528–11530.

[195] M. Barone, M. T. Sciortino, D. Zaccaria, A. Mazzaglia, S. Sortino, *J. Mater. Chem.* **2008**, *18*, 5531–5536.

[196] P. C. Kunz, H. Meyer, J. Barthel, S. Sollazzo, A. M. Schmidt, C. Janiak, *Chem. Commun.* **2013**, *49*, 4896–4898.

[197] F. G. Doro, U. P. Rodrigues-Filho, E. Tfouni, *J. Colloid Interface Sci.* **2007**, *307*, 405–417.

[198] N. A. Stasko, M. H. Schoenfisch, *J. Am. Chem. Soc.* **2006**, *128*, 8265–8271.

[199] M. Ma, H. Noei, B. Mienert, J. Niesel, E. Bill, M. Muhler, R. A. Fischer, Y. Wang, U. Schatzschneider, N. Metzler-Nolte, *Chem. - A Eur. J.* **2013**, *19*, 6785–6790.

[200] S. Gläser, R. Mede, H. Görls, S. Seupel, C. Bohlender, R. Wyrwa, S. Schirmer, S. Dochow, G. U. Reddy, J. Popp, et al., *Dalt. Trans.* **2016**, *45*, 13222–13233.

[201] C. Steiger, T. Lühmann, L. Meinel, *J. Control. Release* **2014**, *189*, 46–53.

[202] C. F. Fortney, R. E. Shepherd, *Inorg. Chem. Commun.* **2004**, *7*, 1065–1070.

[203] E. Sasaki, H. Kojima, H. Nishimatsu, Y. Urano, K. Kikuchi, Y. Hirata, T. Nagano, *J. Am. Chem. Soc.* **2005**, *127*, 3684–3685.

[204] Y. Gabe, Y. Urano, K. Kikuchi, H. Kojima, T. Nagano, *J. Am. Chem. Soc.* **2004**, *126*, 3357–3367.

[205] Y. Yang, S. K. Seidlits, M. M. Adams, V. M. Lynch, C. E. Schmidt, E. V Anslyn, J. B. Shear, *J. Am. Chem. Soc.* **2010**, *132*, 13114–13116.

[206] M. J. Rose, P. K. Mascharak, *Curr. Opin. Chem. Biol.* **2008**, *12*, 238–244.

[207] A. K. Patra, M. J. Rose, K. A. Murphy, M. M. Olmstead, P. K. Mascharak, *Inorg. Chem.* **2004**, *43*, 4487–4495.

[208] R. Pph, H. Ci, T. Chen, J. Zhu, K. Cheng, S. Pengb, *J. Chem. Soc. Dalt. Trans.* **1995**, 2215–2219.

[209] A. K. Patra, P. K. Mascharak, *Inorg. Chem.* **2003**, *42*, 7363–7365.

[210] E. Tfouni, M. Krieger, B. R. McGarvey, D. W. Franco, *Coord. Chem. Rev.* **2003**, *236*, 57–69.

[211] I. K. Lednev, R. E. Hester, J. N. Moore, *J. Am. Chem. Soc.* **1997**, *119*, 3456–3461.

[212] M. D. Kärkäs, T. Åkermark, H. Chen, J. Sun, B. Åkermark, *Angew. Chemie Int. Ed.* **2013**, *52*, 4189–4193.

[213] R. Ramachandran, P. Viswanathamurthi, *Spectrochim. Acta Part A Mol. Biomol. Spectrosc.* **2013**, *103*, 53–61.

[214] M. Y. Ho, M. L. Chiou, R. C. Chang, Y. H. Chen, C. C. Cheng, *J. Inorg. Biochem.* **2010**, *104*, 614–617.

[215] S. McLean, B. E. Mann, R. K. Poole, *Anal. Biochem.* **2012**, *427*, 36–40.

[216] A. J. Atkin, J. M. Lynam, B. E. Moulton, P. Sawle, R. Motterlini, N. M. Boyle, M. T. Pryce, I. J. S. Fairlamb, *Dalt. Trans.* **2011**, *40*, 5755–5761.

[217] J. P. Perdew, *Phys. Rev. B* **1986**, *33*, 8822–8824.

[218] F. Weigend, R. Ahlrichs, *Phys. Chem. Chem. Phys.* **2005**, *7*, 3297–3305.

[219] A. O. Okaru, T. S. Brunner, S. M. Ackermann, T. Kuballa, S. G. Walch, M. Kohl-Himmelseher, D. W. Lachenmeier, *J. Anal. Methods Chem.* **2017**, *2017*, 1–7.

[220] G. Arsenault, B. Chittim, J. Gu, A. McAlees, R. McCrindle, V. Robertson, *Chemosphere* **2008**, *73*, 53–59.

[221] C. Langner, J. Meier-Haack, B. Voit, H. Komber, *J. Fluor. Chem.* **2013**, *156*, 314–321.

[222] J. Axthelm, H. Görls, U. S. Schubert, A. Schiller, *J. Am. Chem. Soc.* **2015**, *137*, 15402–15405.

[223] J. Axthelm, S. H. C. Askes, M. Elstner, G. Upendar Reddy, H. Görls, P. Bellstedt, A. Schiller, *J.*

Am. Chem. Soc. **2017**, *139*, 11413–11420.

[224] H. M. Berends, P. Kurz, *Inorganica Chim. Acta* **2012**, *380*, 141–147.

[225] G. Upendar Reddy, J. Axthelm, P. Hoffmann, N. Taye, S. Gläser, H. Görls, S. L. Hopkins, W. Plass, U. Neugebauer, S. Bonnet, et al., *J. Am. Chem. Soc.* **2017**, *139*, 4991–4994.

[226] T. Perera, P. Abhayawardhana, P. A. Marzilli, F. R. Fronczek, L. G. Marzilli, *Inorg. Chem.* **2013**, *52*, 2412–2421.

[227] P. Rudolf, F. Kanal, J. Knorr, C. Nagel, J. Niesel, T. Brixner, U. Schatzschneider, P. Nuernberger, *J. Phys. Chem. Lett.* **2013**, *4*, 596–602.

[228] U. Hasegawa, A. J. Van Der Vlies, E. Simeoni, C. Wandrey, J. A. Hubbell, *J. Am. Chem. Soc.* **2010**, *132*, 18273–18280.

[229] G. Knizia, *J. Chem. Theory Comput.* **2013**, *9*, 4834–4843.

[230] A. Bahreman, B. Limburg, M. A. Siegler, E. Bouwman, S. Bonnet, *Inorg. Chem.* **2013**, *52*, 9456–9469.

[231] S. J. Carrington, I. Chakraborty, J. M. L. Bernard, P. K. Mascharak, *ACS Med. Chem. Lett.* **2014**, *5*, 1324–1328.

[232] I. Chakraborty, J. Jimenez, W. M. C. Sameera, M. Kato, P. K. Mascharak, *Inorg. Chem.* **2017**, *56*, 2863–2873.

[233] S. J. Carrington, I. Chakraborty, J. M. L. Bernard, P. K. Mascharak, *Inorg. Chem.* **2016**, *55*, 7852–7858.

[234] J. Jimenez, I. Chakraborty, A. Dominguez, J. Martinez-Gonzalez, W. M. C. Sameera, P. K. Mascharak, *Inorg. Chem.* **2018**, *57*, 1766–1773.

[235] N. Maicas, M. L. Ferrándiz, I. Devesa, R. Motterlini, M. I. Koenders, W. B. van den Berg, M. J. Alcaraz, *Eur. J. Pharmacol.* **2010**, *634*, 184–191.

[236] B. Chen, L. Guo, C. Fan, S. Bolisetty, R. Joseph, M. M. Wright, A. Agarwal, J. F. George, *Am. J. Pathol.* **2009**, *175*, 422–429.

[237] M. Kourti, W. G. Jiang, J. Cai, *Oxid. Med. Cell. Longev.* **2017**, *2017*, 1–12.

Declaration of Originality

I certify that the work presented here is, to the best of my knowledge and belief, original and the result of my own investigations, except as acknowledged, and has not been submitted, either in part or whole, for a degree at this or any other university.

Selbständigkeitserklärung

Ich erkläre, dass ich die vorliegende Arbeit selbstständig und nur unter Verwendung der angegebenen Hilfsmittel, persönlichen Mitteilungen und Quellen angefertigt habe.